

POLITECNICO DI TORINO

Master's Degree in Aerospace Engineering



**Politecnico
di Torino**



Master's Degree Thesis

STRUCTURAL DESIGN OF AN UNMANNED BLENDED-WING-BODY AERIAL VEHICLE

Supervisors

Prof. STEFAN HALLSTRÖM

Prof. RAFFAELLO MARIANI

Prof. MARCO GHERLONE

Candidate

GIOVANNI FANELLI

TRITA-SCI-GRU 2025:013

February 2025

Abstract

This thesis presents the preliminary structural design and analysis of the Green Raven UAV, a blended-wing-body (BWB) platform developed by KTH Royal Institute of Technology to test a hybrid hydrogen fuel cell and battery propulsion system. In response to the aerospace industry's increasing emphasis on energy efficiency and sustainable technology, the Green Raven aims to provide a viable foundation for future configurations of commercial wide-body aircraft. The primary design objectives are to develop a modular, lightweight structure that facilitates transport, ensures structural integrity under operational loads, and complies with regulatory weight constraints for UAV certification.

Sammanfattning

Denna avhandling presenterar den preliminära dimensioneringen och analysen av Green Raven UAV, en blended-wing-body (BWB)-plattform utvecklad på KTH för att testa ett hybridssystem med vätgasbränslecell och batteridrivna framdrivning. För att möta flygindustrins ökande fokus på energieffektivitet och hållbar teknik syftar Green Raven till att lägga en genomförbar grund för framtida konfigurationer av kommersiella bredkroppsflygplan. De primära designmålen är att utveckla en modular, lätt struktur som underlättar transport, säkerställer strukturell integritet under operativa belastningar och uppfyller regelverket avseende viktbegränsningar för UAV-certifiering.

Acknowledgements

Vorrei dedicare questa pagina a coloro i quali sono stati al mio fianco durante questo percorso.

"A Letizia, Martina, Sapo, Zurlo, Zizzi, Mattia, Pierpaolo ed Alessandro. La distanza può separare i luoghi, ma non le persone che contano davvero"

"Un grazie speciale a Daniele, che in questi anni è stato per me un fratello, un fedele compagno di sopravvivenza e un'eccellente chef"

"Grazie Sara per essere sempre stata al mio fianco, avermi compreso e sostenuto in ogni momento e per essere riuscita con la tua dolcezza, a strapparmi un sorriso quando ne avevo bisogno"

"Ringrazio infinitamente tutta la mia famiglia, senza la quale non sarei quello che sono oggi. In particolar modo ci tengo a riservare un sentito grazie a zio Fabio, che, nonostante il suo carattere ironico e critico, è stato per me fonte di ispirazione, un modello di perseveranza e impegno che mi ha spronato ad arrivare fin qui"

Un immenso grazie va poi ai miei genitori e a mio fratello

"Grazie Antonio per essere sempre pronto ad ascoltarmi e consigliarmi, e per le emozioni che mi regali ogni volta che mi stringi con il cuore aperto e con un abbraccio che sa di casa"

"Grazie papà, per aver reso possibile tutto questo, per avermi insegnato con il tuo esempio il valore del sacrificio, della dedizione e della forza di volontà. Grazie per avermi sostenuto in ogni passo e per avermi guidato a diventare l'uomo che sono oggi"

"Grazie mamma per aver sempre creduto in me, a volte anche più di quanto non facessi io stesso. Sei sempre stata al mio fianco, supportandomi nei momenti più difficili, ma anche gioendo di ogni mio successo"

Ognuna delle persone a cui ho rivolto i mie più sinceri ringraziamenti è stata parte integrante della mia vita fino ad oggi, non potrei essere più felice di avere persone come voi al mio fianco

Table of Contents

List of Tables	VI
List of Figures	VII
1 Introduction	1
1.1 Context and Motivation	1
1.2 Thesis Objective and Design Constraints	2
2 Conceptual Design	4
2.1 Wing Design	4
2.1.1 Wing Spar	4
2.1.2 Wing Ribs	6
2.1.3 Skin	8
2.2 Main Fuselage Design	9
2.3 Wing-Fuselage Load Transfer Framework	15
2.4 Control Surfaces	20
3 Aerodynamic Loads	24
3.1 Flight Envelope	24
3.2 Aerodynamic Loads Calculation	29
4 Material Selection for Structural Components	31
4.1 Advantages of Composite Materials	31
4.2 Wing Spars and Cylindrical beams	32
4.3 Sandwich Panels	37
4.4 Truss Structures	38
5 Structural Analysis of Wing Components	40
5.1 Mathematical Model	41
5.2 Model Validation	46
5.3 Wing Spar Analysis	50

5.4	Truss Structure Analysis	61
5.5	Rib Analysis	65
5.6	Wing Components' Weight	70
6	Structural Analysis of Fuselage Components	72
6.1	Cylindrical Beams Analysis	72
6.2	Fuselage Main Structure Analysis	77
6.3	Fuselage Components' Weight	80
7	Future Works	82
8	Conclusions	84
A	Aerodynamic data	86
B	Matlab Code for FEM Analysis of the Main Spar	87
C	Matlab Code for FEM Analysis of Cylindrical Beams	96
	Bibliography	102

List of Tables

2.1	Wing spar geometry	6
2.2	Cylindrical beams layout	16
3.1	Load diagram intersection points	26
3.2	Gust diagram intersection points	27
4.1	Unidirectional and Plain wave laminate mechanical properties . . .	34
4.2	Technical characteristics DIVINYCELL H 80	38
4.3	Alluminum 7075-T6 mechanical properties	39
5.1	Model validation results	49
5.2	Wing spar reaction forces and moments	52
5.3	Comparison between maximum stresses and material strengths . . .	57
5.4	Loads applied to truss structures	63
5.5	Comparison between maximum stresses and materials strengths for the wing ribs	70
5.6	Weight of the wing components	70
6.1	Reaction forces applied to the cylindrical beams	73
6.2	Maximum compressive and shear stress in cylindrical beams	75
6.3	Weight of the fuselage components	80

List of Figures

1.1	Green Raven's external geometry	2
2.1	Lightening holes in the wing ribs	8
2.2	Main wing structure	8
2.3	Placement of systems in the fuselage	10
2.4	Fuselage base structures	12
2.5	Systems support framework	13
2.6	Main fuselage structure	13
2.7	Half-lap joint	14
2.8	Flanged bushing connecting the cylindrical beams to the primary load-bearing panels	17
2.9	Inner truss structure	18
2.10	Outer truss structure	19
2.11	Wing-Fuselage load transfer framework	19
2.12	Connection system between the control surface and the wing rib . .	20
2.13	Control surface internal structure	21
2.14	Wing conceptual design	22
2.15	Fuselage conceptual design	22
2.16	Internal structure of the Green Raven	23
3.1	Maneuvering Envelope	26
3.2	Gust Envelope	28
3.3	Flight Envelope	28
3.4	Lift coefficient along the span	29
3.5	Lift distribution	30
5.1	Displacements obtained with ANSYS (left) and MATLAB (right) .	48
5.2	Normal stresses in the flanges obtained with ANSYS and MATLAB	48
5.3	Shear stresses in the flanges obtained with ANSYS and MATLAB .	48
5.4	Shear stresses in the webs obtained with ANSYS and MATLAB . .	49
5.5	Bending and Torsional stiffness distribution	50

5.6	Lift and torsional moment distribution	51
5.7	Wing spar deflection and twist	52
5.8	Transverse load, bending moment and torsional moment distribution	53
5.9	Axial force distribution in flanges (top) and webs (bottom) laminates	54
5.10	Moment distribution in flanges laminates	54
5.11	Direction of shear flow along the perimeter of the cross section . . .	55
5.12	Maximum bending shear flow in walls and flanges	56
5.13	Bending shear flow pattern along the perimeter of the cross section	57
5.14	Torsional shear flow distribution	57
5.15	Normal and shear stresses distribution in the UD flange layer	58
5.16	Normal and shear stresses distribution in the PW_{45} flange layer . .	58
5.17	Normal and shear stresses distribution in the PW_0 walls layer . . .	59
5.18	Normal and shear stresses distribution in the PW_{45} walls layer . . .	59
5.19	Truss structures beam model	62
5.20	Outer truss structure loads and boundary conditions	63
5.21	Inner truss structure loads and boundary conditions	63
5.22	Von Mises stress in the outer truss structure [MPa]	64
5.23	Von Mises stress in the inner truss structure [MPa]	64
5.24	Load distribution applied to the rib	67
5.25	Rib loads and boundary conditions	68
5.26	Rib deflections [mm]	68
5.27	Normal stresses in the rib faces [MPa]	68
5.28	Normal stresses in the rib core [MPa]	69
5.29	Shear stresses in the rib faces [MPa]	69
5.30	Shear stresses in the rib core [MPa]	69
6.1	Front Cylindrical beam deflection	73
6.2	Transverse load and bending moment distribution in the cylindrical beam	74
6.3	Direction of shear flow along the perimeter of the cylindrical beam cross section	75
6.4	Maximum normal and shear stresses distribution in the UD layer .	76
6.5	Maximum normal and shear stresses distribution in the PW_{45} layer	76
6.6	Maximum stress criterion in the PW_{45} ply	79
6.7	Maximum stress criterion in the PW_0 ply	79
6.8	Maximum stress criterion in the core	80

Chapter 1

Introduction

1.1 Context and Motivation

The aerospace industry is in a state of constant innovation, driven by the need to improve energy efficiency and mitigate the environmental impact due to greenhouse gas emissions and noise pollution associated with conventional propulsion systems. In response, starting from the 1980s, the concept of "More Electric Aircraft" (MEA) emerged, where all non-propulsive systems are progressively replaced by electrical systems. With the aim of achieving net-zero goals in aviation, the concept of "All Electric Aircraft" was subsequently developed based on the principles of the MEA, in which not only the traditional hydraulic, pneumatic, and mechanical systems but also the propulsion systems are powered by hydrogen fuel cells and advanced battery systems, thereby significantly reducing the environmental impact.

Simultaneously, Unmanned Aerial Vehicles (UAVs) have gained popularity due to their versatility in a wide range of fields, including surveillance, environmental monitoring, logistics, and emergency response. One of the most advanced configurations for UAVs and future commercial aircraft is the Blended-Wing-Body (BWB) design, which, unlike the traditional architecture, integrates the fuselage and wings into a unified structure, significantly improving aerodynamic efficiency. Several studies, such as the one conducted by Iwanizki et al. [1], have indeed demonstrated that Blended Wing Body concepts are among the most promising configurations, offering a reduction in fuel consumption of approximately 10% over traditional "tube-and-wing" designs, marking a significant advancement in sustainable aviation.

Positioned at the forefront of this movement is the Green Raven project [2], a UAV platform developed at KTH Royal Institute of Technology, conceived as an experimental testbed for integrating a hybrid hydrogen fuel cell and battery propulsion system. This innovative UAV serves as a prototype, not only for the operational testing of hybrid systems but also as a potential model for future

wide-body commercial transport aircraft.

1.2 Thesis Objective and Design Constraints

This thesis aims to develop the preliminary structural design of the Green Raven UAV, ensuring it is lightweight yet capable of withstanding the aerodynamic loads experienced by the aircraft under the most demanding flight conditions, while adhering to the project's requirements.

Designed for a target endurance of 1 hour at a cruise altitude of 500 meters, the UAV is intended to operate primarily from paved runways. In compliance with EU C3C4 UAV certification standards, the aircraft's maximum takeoff mass (MTOM) is limited to 25 kg. The previously conducted weight estimates of the onboard systems dictate that the structural weight must not exceed 15 kg, thus requiring careful consideration in the selection of lightweight materials and the implementation of efficient structural solutions.

The Green Raven's configuration shown in figure 1.1 employs a Blended-Wing-Body (BWB) design in a tailless format characterized by a wingspan of 4 m, a centerline chord length of 1.7 m, an outboard chord of 0.25 m at the wingtip and a wing sweep angle of 30° .

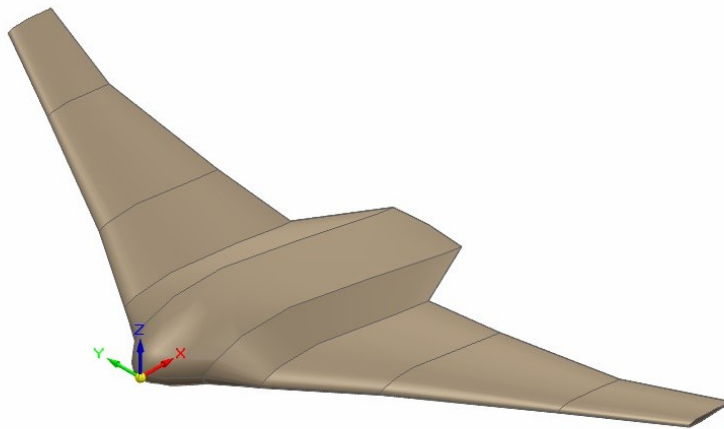


Figure 1.1: Green Raven's external geometry

Among the project requirements is the need to create a structure that can be disassembled into three primary components, the two wings and the fuselage, to facilitate easy transport and reassembly. Additionally, the structural components must be designed for straightforward construction, allowing for fabrication in a laboratory setting with minimal complexity and must be compatible with the

predefined placement of key systems within the fuselage such as the hydrogen tank, fuel cells, and auxiliary battery, ensuring that the load-bearing components do not interfere with the installation of such systems.

A unique challenge in this design phase is the limited information available on the weight and placement of some systems, including engines and landing gear, which are yet to be finalized. Therefore, the fuselage design must incorporate a level of flexibility that allows for future modifications and system integrations as specific details become available. Rather than providing a fully detailed design, this thesis focuses on developing a preliminary structure that can be easily adapted in later stages of the Green Raven's design.

The aerodynamic characteristics of the Green Raven, detailed in the appendix, were determined through an in-depth analysis conducted by the team led by Professor Raffaello Mariani and results served as the basis for determining the load conditions to which the structure is subjected.

Given these constraints, the structural integrity of the design is paramount, as the structure must reliably withstand operational loads without risk of failure.

Chapter 2

Conceptual Design

In this chapter, the elements characterizing the internal structure of the Green Raven will be described and specifically, the reasons that led to the choice of these components and the definition of their geometry will be examined.

2.1 Wing Design

Aeronautical structures are usually classified as truss, shell or reinforced semi-monocoque structures. Truss structures are often used in the fuselage, while wings are usually composed of either shell or semi-monocoque shell structures. In shell structures, the outer skin serves as the primary structural element, responsible for absorbing all loads and transferring them to the fuselage. In semi-monocoque structures, however, the skin transfers aerodynamic lift and drag loads to the spar through the ribs. The spar then absorbs bending and torsional loads, allowing the outer skin to be significantly lighter. This approach is currently the most widely used in the aeronautical industry, as it provides the optimal design for lightweight structures. For this reason, the structural design of the Green Raven is based on a reinforced semi-monocoque structure.

2.1.1 Wing Spar

The spar is one of the most critical components of the wing structure, as it bears all the aerodynamic loads applied to the wing. For this project, a single spar design was selected, located at 30 % of the aerodynamic chord. Since aerodynamic loads cause both bending and torsion in the wing, the spar experiences shear stresses as well as normal stresses due to the bending moment. Typically, aeronautical spars are composed by a web, which handles the shear forces, and flanges, which, due to their separation, greatly enhance bending strength and absorb the normal

loads from bending moments. To achieve the lightest possible structure, a closed cross-section spar was selected, as beams with such a design provide considerable torsional stiffness. Consequently, since the spar alone provides the necessary torsional rigidity for the wing, the skin no longer functions as a primary structural component. Instead, it merely transfers aerodynamic loads to the ribs, allowing for a significant reduction in its weight. Furthermore, due to the wing's taper, the height of a constant cross-section spar would be constrained by the maximum airfoil thickness at the wingtip. As a result, at the wing root, where normal stresses from bending moments are usually highest, the reduced section height would diminish bending stiffness, leading to greater wing deformation. Additionally, this would increase the normal stresses on the caps for a given width. The most appropriate solution, therefore, is to use a spar with a thin-walled, closed rectangular cross-section to enhance torsional stiffness, and with a height that decreases linearly from the root to the tip to increase bending stiffness. It is important to note that, although the wing's external geometry does not have a constant taper ratio, a linearly tapered spar was chosen. Constructing a rectangular cross-section beam with a variable taper ratio along its length would be significantly more complex, especially for an element made of composite materials. Therefore, a trade-off was made between optimizing the spar's geometric characteristics to enhance its mechanical properties and reducing the complexity of construction. The spar's geometric characteristics are primarily dictated by the UAV's overall design. The maximum allowable height of the spar section along its span is constrained by the wing profile's thickness and curvature. For the ribs to remain continuous, the spar height must be less than the thickness of the airfoil at each section. Additionally, due to the airfoil's curvature, the spar's maximum width also affects its maximum height. These geometric factors directly impact the spar's stiffness characteristics. Increasing the width of the spar enhances its bending stiffness, which reduces compressive stress on the flanges. Meanwhile, increasing the spar's height influences both bending and shear stiffness. A larger cross-sectional area also boosts the spar's torsional stiffness, providing greater overall rigidity. The design takes into account that the spar's bending stiffness is proportional to the square of its height and linearly proportional to its width, as outlined in section 5. Therefore, maximizing the distance between the two flanges was prioritized. This approach not only improves the bending stiffness but also optimizes the transmission of shear loads from the ribs to the spar. Another possible approach is to proceed with an optimization of the spar. Given the material properties, applied loads, and boundary conditions, an iterative optimization process could be employed. Starting with initial values for the spar's width, tip and root height, as well as the thickness of the webs and flanges, structural analysis could be conducted to determine stress distribution within the spar. This would allow for adjustments to the spar's geometry to achieve the required structural stiffness

while minimizing the overall weight. However, since the design relies on composite laminates, where both the thickness and mechanical properties depend on the stacking sequence, a full structural optimization is beyond the scope of this project. As long as weight constraints are met, it was decided to establish the spar’s width and height based on structural and geometric considerations, without performing an exhaustive optimization. Following this, an initial stacking sequence will be defined for both the webs and flanges. Through structural analysis, the spar’s capability to withstand applied loads will be assessed. If the analysis reveals that the structure does not meet the required stiffness, a new stacking sequence will be developed, iterating as necessary until the spar meets the required performance criteria. The geometric characteristics of the wing spar, are detailed in table 2.1.

Length	Width	Tip height	Root height
1920 mm	20 mm	10 mm	70 mm

Table 2.1: Wing spar geometry

2.1.2 Wing Ribs

The ribs, in addition to maintaining the aerodynamic profile and preserving performance, can also bear concentrated loads from the presence of engine nacelles, landing gear, or transfer aerodynamic loads from the control surfaces. In traditional aircraft, the wings house fuel tanks to increase the available volume for payload within the fuselage and utilize the fuel weight to partially counteract the wing’s lift load. Thus, the ribs also serve to compartmentalize the fuel tanks. However, in the case of the Green Raven, which is powered by a hydrogen fuel cell hybrid system with all systems housed within the fuselage, the ribs primarily serve to transfer reaction loads from the control surfaces to the spar, in addition to their shaping function. For this reason, it is beneficial to position a rib at each end of the control surfaces. Additionally, since the control surfaces rotate around a rod (as will be described in section 2.4) that is prone to bending deformation due to aerodynamic loads, a rib has been added at the midpoint of each control surface to minimize this effect. However, these ribs must be rounded near the leading edge to allow the control surfaces to rotate around the rod. This also helps reduce deformation of the skin, as decreasing the spacing between ribs reduces the size of each skin panel, thereby limiting the overall deformation of the aerodynamic profile. Finally, it is, of course, necessary to add ribs at the wing root and tip.

Once defined the number and location of ribs required to properly transfer aerodynamic loads and concentrated loads from the control surfaces to the spar, it is essential to establish how they will be connected to the skin and the spar. One of the most commonly employed solutions is to design ribs with flanges, which

would increase the contact surface with both the skin and the spar, thereby allowing the various elements to be securely fastened together. However, since composite materials were chosen to reduce structural weight, this solution would complicate the manufacturing process of the ribs, making it less suitable for this application. Another approach could involve the use of L-shaped joints. While this would significantly lighten the structure, it would also require the production of many joints and complicate the assembly process. Therefore, a less conventional solution in the aeronautical field has been chosen: using sandwich panels for the construction of the ribs. This choice offers two main advantages: first, it significantly increases the contact surface between the skin and the ribs, as well as between the ribs and the spar. This allows not only for bonding the components together but also for expanding the surface area through which loads are transmitted to the spar, thereby preventing the development of point loads on the ribs, which could lead to structural failure.

Secondly, since sandwich panels are composed of two thin layers with high mechanical properties and a lightweight core designed to maintain the separation between the layers, they are highly resistant to bending. Although the ribs are not subjected to out-of-plane concentrated or distributed loads, this property helps to increase the overall stiffness of the wing, simplifying the assembly process and preventing the ribs from breaking during the transport and assembly phases of the UAV. The additional weight from the core between the two panels can be minimized by limiting the core's thickness and selecting a material with low density. This approach achieves a good balance between structural stiffness and component weight.

In aircraft design, ribs that do not serve structural functions, such as those to which engine nacelles are attached, and are not subject to high loads, are often designed with lightening holes. These holes reduce the weight of the structure while also allowing for the passage of electrical systems that power the control surfaces. For this reason, it was decided to design the ribs, with the exception of those at the root and the tip, to include three lightening holes, as shown in figure 2.1. The root rib was not designed with holes for the passage of electrical systems, as such holes must logically align with those in the fuselage structure. However, given the need to modify the fuselage in subsequent design phases, where the placement of the systems will be defined in greater detail, it is not feasible at this stage to design holes in the structure that might conflict with future design developments. This design choice effectively reduces the weight of the ribs in less load-intensive areas, optimizing the overall mass distribution while maintaining the structural integrity in the most critical areas around the holes necessary for the insertion of the spar and the cylindrical beams (which will be discussed in section 2.3). The ribs distribution along the wing spar is shown in figure ??.

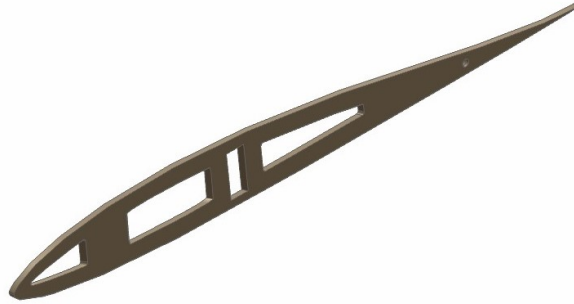


Figure 2.1: Lightening holes in the wing ribs

Given the large dimensions of the ribs near the root of the wing, a "false spar" was added to the structure, as shown in figure 2.2. Although this component is not designed to bear the primary aerodynamic loads, it enhances the overall stiffness and stability of the structure and interconnects the ribs, preventing excessive deformations of the panels due to out-of-plane loads.



Figure 2.2: Main wing structure

2.1.3 Skin

The design of the UAV skin is a fundamental aspect of the overall structural performance of the aircraft. The primary role of the skin in this project is to transfer aerodynamic loads to the ribs, a design choice enabled by the structural configuration of the wing spar. Since the spar, as reported in section 2.1.1, is designed to absorb all bending and torsional loads, the skin does not serve as a structural component. This non-structural role allows for significant weight

reduction, enabling the selection of materials optimized for lightweight and cost-efficiency rather than structural strength.

Based on these considerations, a polymer film produced by Oratex was chosen for the UAV skin. Polymeric film skins are increasingly utilized in aircraft design due to their significant advantages in weight reduction and ease of maintenance. A prime example of this application can be seen in ultralight aircraft, notably the Belite Ultralight. This aircraft leverages the lightweight and durable characteristics of Oratex to meet stringent weight requirements while enhancing performance and efficiency.

Oratex polymer film emerged as the ideal material due to its combination of lightweight properties, ease of application, and cost-effectiveness. The film's lightweight nature is particularly important for the UAV, as reducing the skin's weight directly enhances the aircraft's flight performance.

Another advantage of Oratex is its excellent durability. This polymer film is resistant to UV radiation and moisture, ensuring long-term performance even under harsh operating conditions.

The ease of application is a further reason for selecting Oratex. Unlike traditional skin materials that require adhesives, joints, or complex installation processes, Oratex can be heat-shrunk to fit directly over the frame of the UAV. This not only simplifies the manufacturing process but also reduces labor costs and the potential for errors during application. This design choice represents a strategic shift from conventional aircraft skin designs, where the skin often plays a structural role, prioritizing durability, ease of application, and lightweight properties.

2.2 Main Fuselage Design

The fuselage is the central structure of the UAV, housing critical systems such as the hydrogen tank, batteries, fuel cells, avionics and propulsion systems. Given the concentration of these heavy components, the fuselage must withstand significant concentrated loads arising from their weights, as well as aerodynamic loads transferred from the wings. The design is complicated by the fact that, at this stage, only preliminary estimates have been made regarding the sizing of certain systems, such as the engines and landing gear. Regarding the landing gear, it has not yet been determined whether it will be retractable or fixed. A retractable landing gear would reduce overall aerodynamic drag, thus improving the aerodynamic performance of the UAV. However, it requires a mechanism for retraction, which increases the overall weight and requires adequate space within the UAV to accommodate it when retracted. Furthermore, regarding the engines, it has not yet been definitively decided whether there will be two or three. Nor has their exact placement been determined to ensure good aerodynamic performance without

interfering with other systems. While the final placement of these components will depend on aerodynamic, structural, and spatial considerations, it is yet unclear whether these systems will be integrated within the fuselage or the wings. As a result, the design of a fully detailed fuselage structure falls outside the scope of this project, given the current phase of development. Recognizing the uncertainties associated with component positioning, a flexible design approach was adopted for the fuselage structure. This approach prioritizes modularity, allowing for adjustments in subsequent design phases once the exact requirements and placements of the systems are defined. The aim is to ensure that the fuselage structure can accommodate any design modifications that may arise as the UAV's development progresses. This preliminary fuselage design focuses on meeting the requirements posed by the systems whose positions have already been determined, namely the hydrogen tank, batteries, and fuel cells. The placement of this components within the fuselage was driven by their respective sizes and requirements on the UAV's overall stability. Due to the large size of both the hydrogen tank and the fuel cells, these components must be positioned at the location of maximum airfoil thickness, achieved by sectioning the fuselage along the plane of symmetry. Consequently, to ensure the UAV's stability, the extra batteries need to be placed near the nose of the aircraft. These systems, depicted in Figure 2.3, establish the primary constraints for the current phase of the fuselage design.

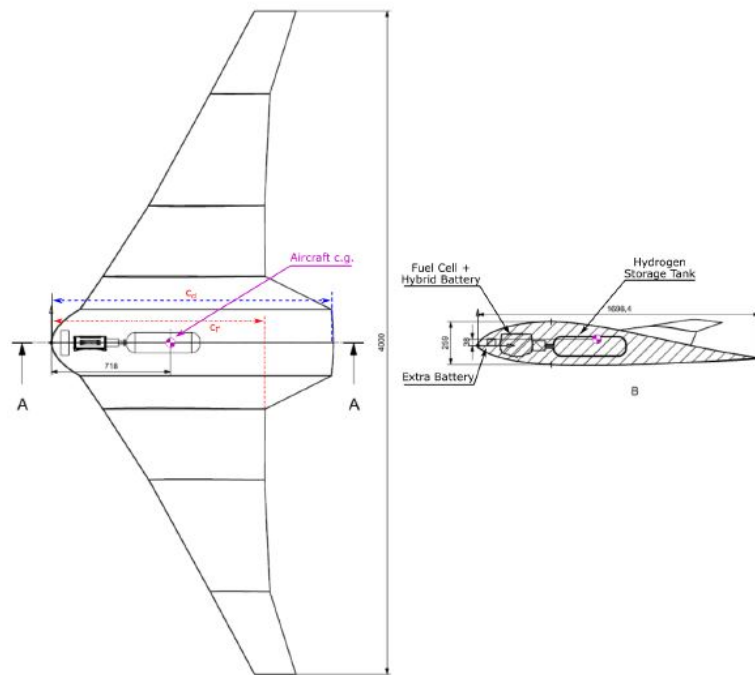


Figure 2.3: Placement of systems in the fuselage

However, further refinement of their placement will be required as additional systems are specified and integrated into the UAV.

While the design of the wing is fairly standardized across many aircraft solutions, the fuselage design is far more dependent on several factors. These include the type of payload, fuselage geometry, and the distribution of concentrated loads, along with considerations for minimizing structural weight. In traditional aircraft architecture, the fuselage is usually composed of a few key structural components:

- **Formers (or Frames):** These elements are essential for maintaining the fuselage's shape. There are two types: shaping formers, which help retain the external contour of the fuselage, and load-bearing frames, which are reinforced to handle concentrated loads, such as those from landing gear attachments or wing connections.
- **Longerons and Stringers:** These longitudinal elements provide the fuselage with adequate bending stiffness, stabilize the skin panels and distribute stresses throughout the structure.
- **Bulkheads:** These reinforced structures are necessary in pressurized aircraft to withstand cabin pressurization forces.

However, in the case of this UAV, which does not require pressurization, bulkheads are unnecessary. Additionally, the design features of this UAV, specifically, the blended wing-body geometry, the choice of composite materials, and the need for a simplified manufacturing process, make a traditional fuselage design less suitable. For these reasons, and particularly due to the blended wing body geometry, it was decided to proceed with the conceptual design of the fuselage by considering it as an extension of the wing and consequently, the decision was made to use ribs as the longitudinal structural elements. The fuselage design incorporates two ribs located at the separation planes between the fuselage and the wings. These ribs are tasked with absorbing the aerodynamic loads from the skin and the control surfaces integrated into the fuselage. Additionally, two primary load-bearing panels are positioned 10 centimeters away from the UAV's plane of symmetry. These panels are the most critical structural elements within the fuselage. They are engineered not only to absorb the aerodynamic loads from the skin but also to handle the loads transferred from the external ribs, the concentrated loads from the wings, and the weights of the onboard systems. Similarly, traditional formers in the fuselage have been substituted with transverse sandwich panels. These panels not only link the fuselage ribs preventing relative translation, but also channel aerodynamic loads from the external ribs to the primary load-bearing panels. In this way, all the loads acting on the fuselage are effectively transferred to the two primary load-carrying ribs. As a result, to balance these concentrated loads, the aerodynamic forces

from the wings will also need to be transferred to the two load-carrying ribs. This approach ensures that both the concentrated system weights and the aerodynamic loads are effectively managed by these primary structural elements. The base structure of the fuselage is shown in figure 2.4.

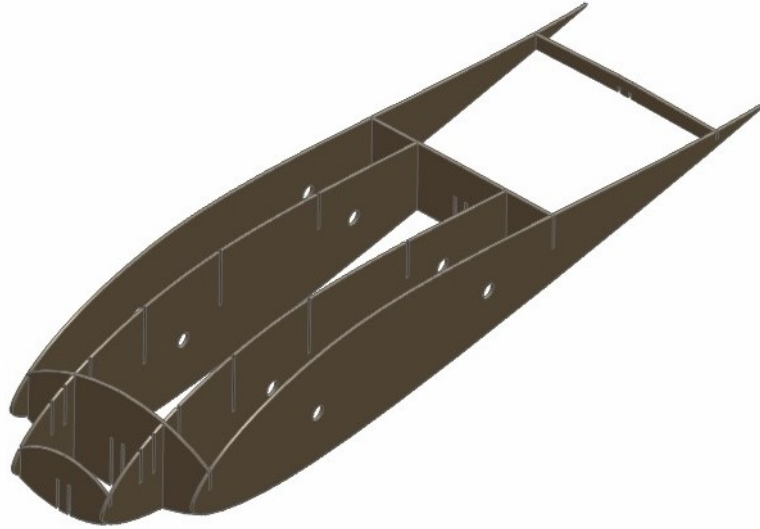


Figure 2.4: Fuselage base structures

Once defined the basic structure of the fuselage, the framework responsible for supporting the systems and transferring the loads due to their weight to the primary load-bearing ribs was established. This structure consists of two panels for each system, symmetrically arranged around the system's center of gravity, spanning between the two primary panels. These panels are designed to support crucial components such as the hydrogen tank, fuel cells, and extra batteries and to transfer the inertial loads to the primary load-bearing ribs. Additionally, two longitudinal panels have been designed whose role is to transmit to the systems the loads originating from the engines, directed along the longitudinal axis of the UAV. The supporting framework is illustrated in figure 2.5, where elements in red represent the extra battery, the fuel cells, and the hydrogen tank. The structure is designed such that the systems are supported directly by the support framework, which then transfer the concentrated loads to the primary load bearing ribs to which loads from the external ribs are also transferred. Given this configuration, it is beneficial to ensure that the loads generated by the wings are directed towards the primary load-bearing panels as well. As a result, these panels serve as the key structural components where all loads converge. The main structure of the fuselage is shown in figure 2.6.

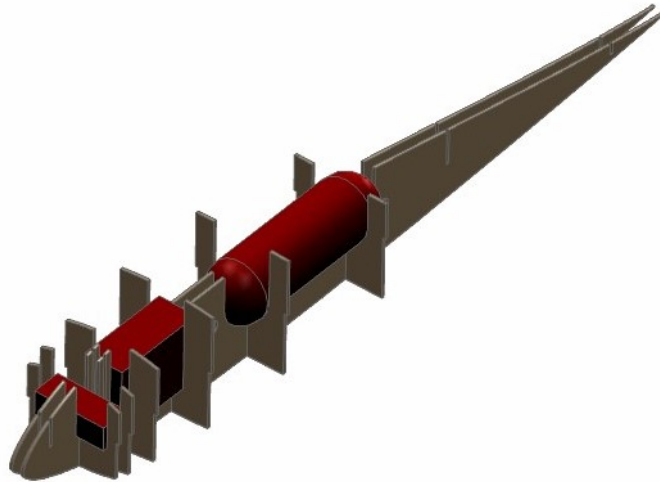


Figure 2.5: Systems support framework

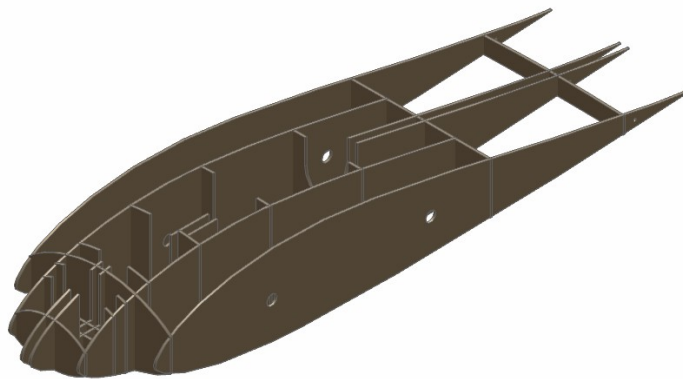


Figure 2.6: Main fuselage structure

Among the various design configurations considered for the fuselage, this solution was chosen since prioritizes both lightweight construction and the ability to withstand concentrated loads from onboard systems. Additionally, this design is straightforward to manufacture and assemble, with an emphasis on enabling easy extraction and reinstallation of systems, which is crucial for operational flexibility and maintenance. The structure was specifically designed to simplify production, reducing both time and costs while maintaining a high level of reliability.

This approach makes it well-suited for current project requirements while also accommodating potential modifications as the design evolves. For this reason, considering the potential need for further modifications in later design phases, it was decided not to include lightening holes in the fuselage structure, as they could conflict with future design iterations. Given that these panels are made of composite materials, a practical choice for connecting them would be to use L-shaped flanges at their intersections. This approach can facilitate an effective load transfer. However, it could also lead to an excessive weight increase, as the total number of flanges required would depend on the total number of panels within the fuselage. Although using flanges to bond the panels would globally reinforce the structure, the individual panels would still exhibit significant flexibility when subjected to out-of-plane loads. For these reasons, the panels have been designed as sandwich structures, similar to the approach taken for the wing ribs. While this choice does increase the weight of the panels, it also provides the structure with adequate stiffness, which is particularly advantageous during the construction and assembly phases. Additionally, by selecting a core material with a lower density, the weight penalty associated with opting for sandwich panels can be minimized. Furthermore, selecting sandwich panels allows for a thickness that enables the connection of components using the half-lap joints, a type of connection where two panels intersect and partially overlap by removing material from each so that they fit together flush. In this configuration, each panel is cut to half of its height at the intersection, allowing them to slot into each other as shown in figure 2.7.

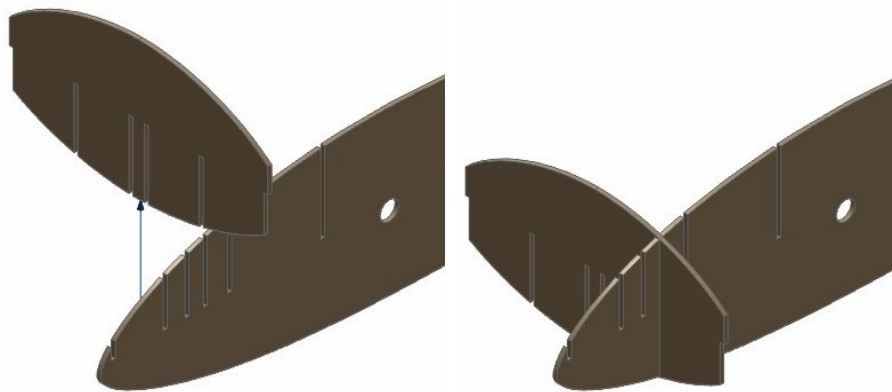


Figure 2.7: Half-lap joint

This design choice maintains the panels' overall thickness and creates a smooth, continuous surface on both sides of the joint. In this design, the newly created contact surfaces from the material removal are used as bonding surfaces. Adhesive is applied to these surfaces, securing the panels to one another and enabling efficient

load transfer between them. Additionally, this method simplifies the assembly of the UAV structure significantly. While the current design phase does not include a fully detailed layout of the fuselage structure, it establishes a robust foundation that can be refined as the UAV's systems and requirements become more defined. By focusing on a modular and flexible design, this preliminary structure ensures that the fuselage can adapt to future design changes.

2.3 Wing-Fuselage Load Transfer Framework

The choice of the connection system for transferring loads from the wing to the fuselage is critical for the structural design of the UAV. This is because all aerodynamic loads distributed along the wing must be transferred to the fuselage as concentrated loads. In traditional aircraft, the load from the wing's spars is transferred to the fuselage's load-bearing frames through joints and bolts, which effectively handle high shear, bending, and torsional loads. However, in the case of the UAV being examined, this solution is not suitable since the design necessitates that the entire UAV be easily disassembled and reassembled to facilitate transportation. Additionally, the structure is made up of composite materials, which present specific challenges. Traditional joints and bolts can lead to stress concentrations and potential damage to the composite materials, compromising their integrity.

A widely adopted solution for large UAVs involves using two cylindrical beams that traverse the fuselage and extend into the wings. This approach not only facilitates efficient load transfer from the wings to the fuselage structure but also significantly simplifies the UAV's assembly process. By employing two cylindrical beams, it becomes possible to handle shear, bending, and torsional loads through the application of purely shear forces within the cylindrical beams themselves. The cylindrical beams are connected to each of the two spars at two points along the wing, which leads to a simply supported configuration rather than a clamped one at the root for the spar. This setup results in reaction forces that are purely shear loads at the connection points between the spars and cylindrical beams. Additionally, at each of the two connection points, torsional loads are managed through differential shear between the two cylinders. The use of dual cylindrical beams for wing-fuselage connections is typically seen in low-wing or high-wing configurations, where the wings can fully span across the fuselage. In contrast, mid-wing configurations often present challenges for this approach, as the beams may interfere with payload space within the fuselage. Despite the mid-wing configuration of the Green Raven UAV, the dual cylindrical beam solution was chosen due to its advantages in ease of construction, assembly, and efficient load transfer. This approach minimizes the need for heavily reinforced structural elements within the fuselage, which would

otherwise be necessary to handle high bending moments transmitted from the wings.

The positioning of the two cylindrical beams in this configuration is constrained by the internal systems housed within the fuselage, particularly the hydrogen tank and its connection system to the fuel cells. Careful placement of the beams ensures that these critical components remain accessible and unaffected. The length of the cylindrical beams is determined by the fuselage width and the overlap length into the wings. This overlap impacts not only the weight of the beams but also the boundary conditions for the spars. Given that the spars are simply supported, the reaction forces depend on the distance between the two supports, greater separation between them results in lower reaction forces for the same external loads. Thus, increasing the distance between the supports reduces the load on the structures responsible for transferring forces from the spars to the cylindrical beams, allowing for a lighter and less critical design.

An additional benefit of increasing the support spacing is that it decreases the maximum tip deflection of the wing, thereby minimizing structural deformations that could affect the UAV's overall aerodynamic characteristics. For these reasons, extending the cylindrical beams' length is advantageous, even though this may result in increased fuselage bulk when disassembled. Since the Green Raven features a dihedral angle, the maximum possible length for the cylindrical beams is constrained by the aircraft's external geometry and internal fuselage systems. These constraints are also influenced by the external radius of the beams. While increasing the radius provides structural benefits by enhancing shear and bending stiffness, it also adds to the weight and space requirements. As such, an iterative process was undertaken to optimize the external radius, length, and center positioning of the beams within the UAV's symmetry plane. This iterative process sought to arrive at a configuration that would avoid interference with fuselage systems, comply with geometric constraints, and achieve a balance between structural stiffness and overall weight. By carefully adjusting these parameters, a design was achieved as reported in table 2.2.

	Center x-coord.	Center z-coord.	Outer diameter	Length
Front beam	500 mm	0 mm	30 mm	1020 mm
Rear beam	950 mm	-20 mm	30 mm	1020 mm

Table 2.2: Cylindrical beams layout

In this configuration, the four structures responsible for transferring loads from the spars to the cylindrical beams are positioned at distances of 20 cm and 50 cm from the UAV's symmetry plane. Although the total distance between the outermost load-bearing structures is 100 cm, the beams have been extended by

an additional centimeter on each side. This slight extension ensures that, during flight, any structural deformation will not cause the cylindrical beams to slip out of their supports. As noted in the previous section, the primary load-bearing ribs in the fuselage are designed to absorb the loads coming from the wings. To effectively transfer these loads from the cylindrical beams to the ribs, flanged bushings have been employed. These bushings shown in figure 2.8 play a crucial role in redistributing high shear loads transmitted by the cylindrical beams over a broader area of the panel, thus preventing the development of concentrated loads that could lead to material failure.

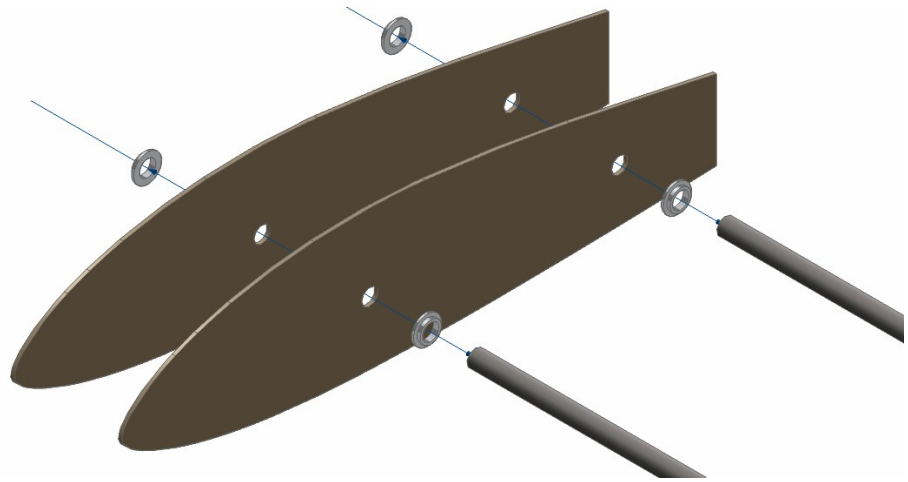


Figure 2.8: Flanged bushing connecting the cylindrical beams to the primary load-bearing panels

The design of the structures responsible for transferring loads from the spars to the cylindrical beams diverges from the UAV's general design approach, primarily due to the critical nature of these elements. These components are subjected to highly concentrated loads at specific points, which could pose a risk of structural failure if composite materials were used. Composite materials, while beneficial for their lightweight properties, can be particularly susceptible to failure under concentrated stresses due to their layered structure and anisotropic nature. To mitigate these risks, an isotropic material with well-defined and consistent properties was chosen, eliminating the need for extensive material testing. As a result, 7075-T6 aluminum was selected for these components. This alloy, frequently used in aerospace applications, offers a high strength to weight ratio and is specifically well suited for handling concentrated loads. To avoid the excessive weight increase associated with aluminum ribs thick enough for bonding to the spar, a reinforced truss-style structure was chosen for load transfer. This design mimics a truss framework and is composed of three primary reinforcement elements:

1. Front Circular Reinforcement: this component houses the front cylindrical beam;
2. Central Rectangular Reinforcement: here, the rectangular spar is inserted and bonded to ensure effective load transfer;
3. Rear Circular Reinforcement: this component houses the rear cylindrical beam.

The truss structure channels shear and torsional loads from the spar through the central rectangular reinforcement and distributes them to the front and rear circular reinforcements via truss members. The layout includes segments connecting the four corners of the central rectangular reinforcement to the upper and lower edges of the front and rear circular reinforcements. The truss framework also incorporates vertical members, which, together with the tangent segments, create near-rectangular sections. As truss structures gain rigidity primarily through triangular configurations, diagonal members are added within each rectangular section to enhance structural stiffness. Since these diagonal members are longer than the vertical ones, they are more susceptible to buckling. To prevent instability, the diagonal members are oriented to carry tensile rather than compressive loads, as the critical buckling load decreases with increased length. Consequently, the shorter vertical members, which are less prone to buckling, are loaded in compression, ensuring a stable and efficient structural framework for load transfer. The structure responsible for transferring the load from the spar to the cylindrical beams, located at the root of the wing, will be referred to as the inner truss structure, while the second structure, positioned 30 cm away from it, will be referred to as the outer truss structure. Both structures are illustrated in figures 2.9 and 2.10.

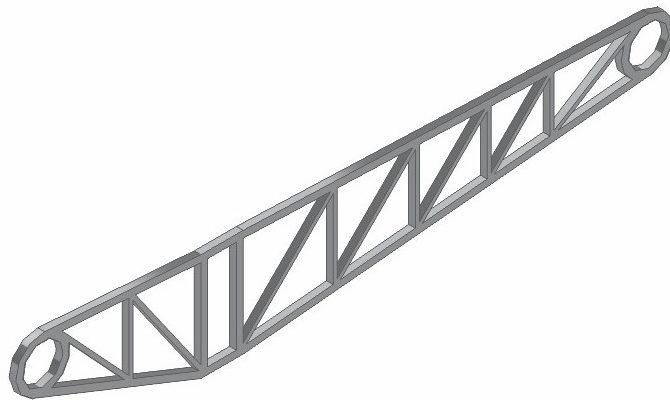


Figure 2.9: Inner truss structure

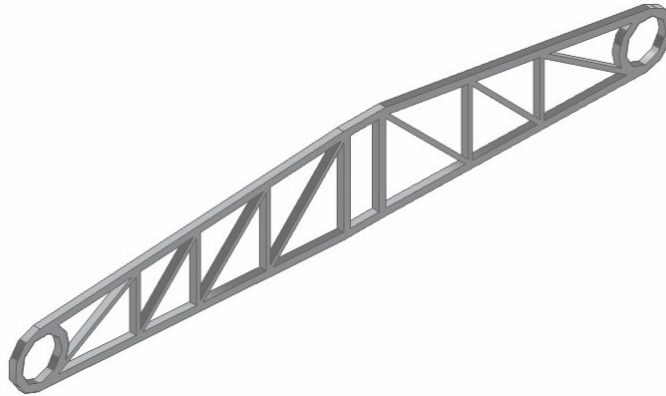


Figure 2.10: Outer truss structure

The initial configuration specifies a thickness of 5 millimeters to ensure adequate contact surface between the truss structure and the wing spar, essential for effective bonding and correct load transfer. Both cylindrical and rectangular reinforcements, as well as the segments connecting these reinforcements, have been designed with a width of 5 millimeters, meanwhile, the vertical and diagonal truss elements have been designed with a width of 3 millimeters. The load transfer framework, including the truss structures, cylindrical beams, and the wing spar, is shown in figure 2.11.

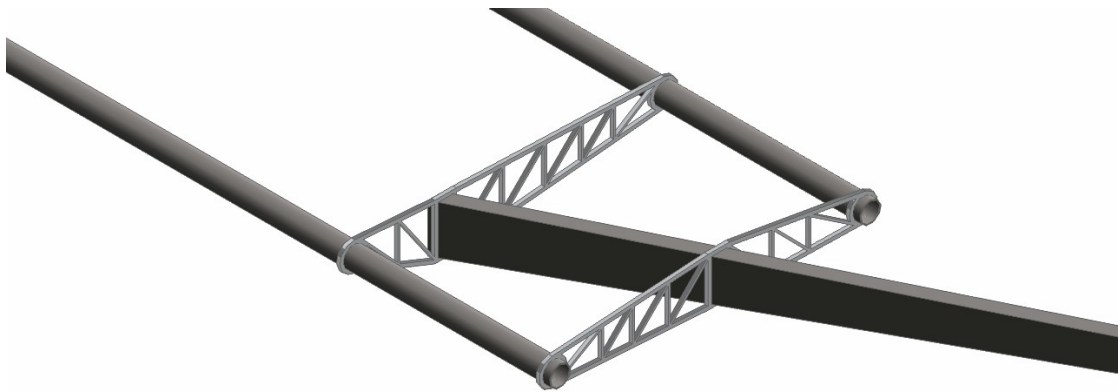


Figure 2.11: Wing-Fuselage load transfer framework

2.4 Control Surfaces

Control surfaces play a fundamental role in managing the UAV's flight, as by varying the geometric characteristics of the aerodynamic profile, under the same external conditions, they allow for significant changes in the lift and drag acting on the wing. The primary control surfaces are responsible for the aircraft's rotation around its three main axes. Specifically, the ailerons, located near the wingtips, operate differentially, causing a difference in lift between the wings, which generates the roll moment. The elevators, situated on the aircraft's tail stabilizer, modify its aerodynamics, and due to the distance between the tail stabilizer and the aircraft's center of gravity along the longitudinal axis, they induce a pitch moment. The rudder, positioned on the vertical tail stabilizer, deflects to create a lateral force that controls the yaw of the aircraft. In the design of the Green Raven, which lacks a vertical tail stabilizer, yaw control is achieved through the differential rotation of control surfaces located at the rear of the aircraft. Specifically, one tail surface is angled to increase aerodynamic resistance on one side of the aircraft, while the opposite surface is positioned to reduce resistance. This contrast between increased and decreased resistance creates a yaw moment that causes the aircraft to rotate around the vertical axis. Due to the proximity of these surfaces to the aircraft's center of gravity, these adjustments do not induce a significant rolling moment; however, this side effect must be carefully counterbalanced using the three control surfaces positioned along each wing.

The structure design of the control surfaces also emphasizes simplicity in fabrication and assembly. Each control surface is connected to the ribs via an aluminum cylindrical rod, around which it is free to rotate. These rods absorb the aerodynamic load from the control surfaces and transmit it to the ribs through aluminum joints shaped like flanged bushings. These bushings are partially inserted into holes made in the ribs to accommodate them as shown in figure 2.12 and are bonded to the ribs through the flanges to allow for a more distributed load transfer.

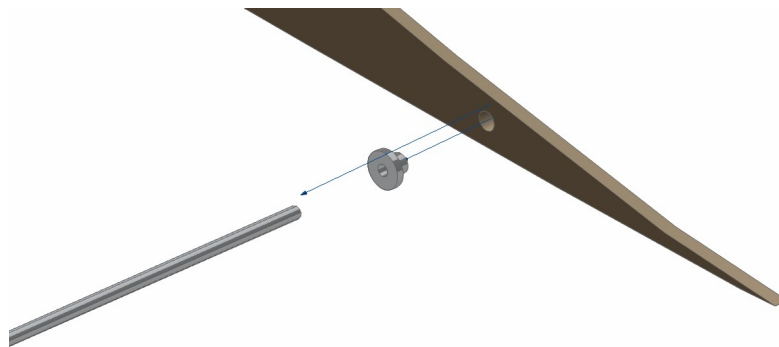


Figure 2.12: Connection system between the control surface and the wing rib

This design prevents the development of concentrated loads where the aerodynamic profile is thinnest, which could lead to rib failure. The initial design of the control surfaces incorporated a sandwich structure, consisting of a composite material skin and a foam core. This configuration combines the strength and lightness of the composite material with the lightweight properties of the foam. However, it comes with a drawback. The use of foam filler in the control surface significantly increases the contact area between it and the aluminum rod, thereby also increasing the frictional force between the two. Consequently, more power is required from the electrical systems to overcome this friction and maneuver the surfaces. For this reason, the design of the control surfaces adopts a philosophy similar to that used for the wing, incorporating ribs positioned near the wing ribs. These ribs effectively transmit the aerodynamic loads from the polymer film skin to the central rod. Additionally, a crucial longitudinal element is integrated within the structure, whose purpose is to prevent any translational and rotational movement between the ribs. This element also contributes to the flexural strength of the rod, enhancing the overall rigidity and functional integrity of the control surfaces. These components are interconnected using half-lap joints, mirroring the construction techniques used in the main structure of the fuselage.



Figure 2.13: Control surface internal structure

This design approach significantly reduces the friction developed between the control surface and the rod, while maintaining a structure that is both lightweight and sufficiently rigid and also simplifies the manufacturing process, making it more efficient and cost-effective. The final configuration of the conceptual design of the wing, fuselage, and overall structure, including the control surfaces and the components responsible for load transfer between the wing and the fuselage, are shown in figures 2.14, 2.15 and 2.16 respectively.



Figure 2.14: Wing conceptual design

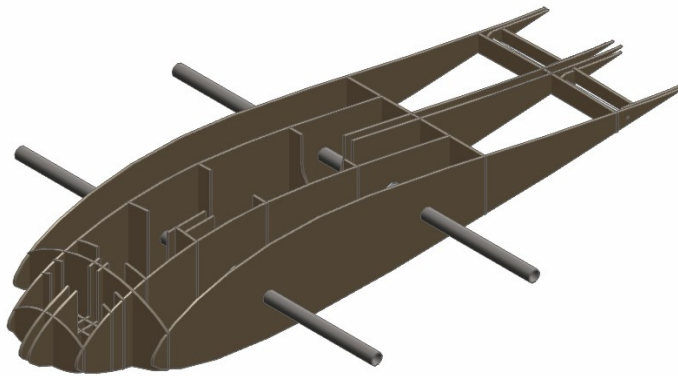


Figure 2.15: Fuselage conceptual design

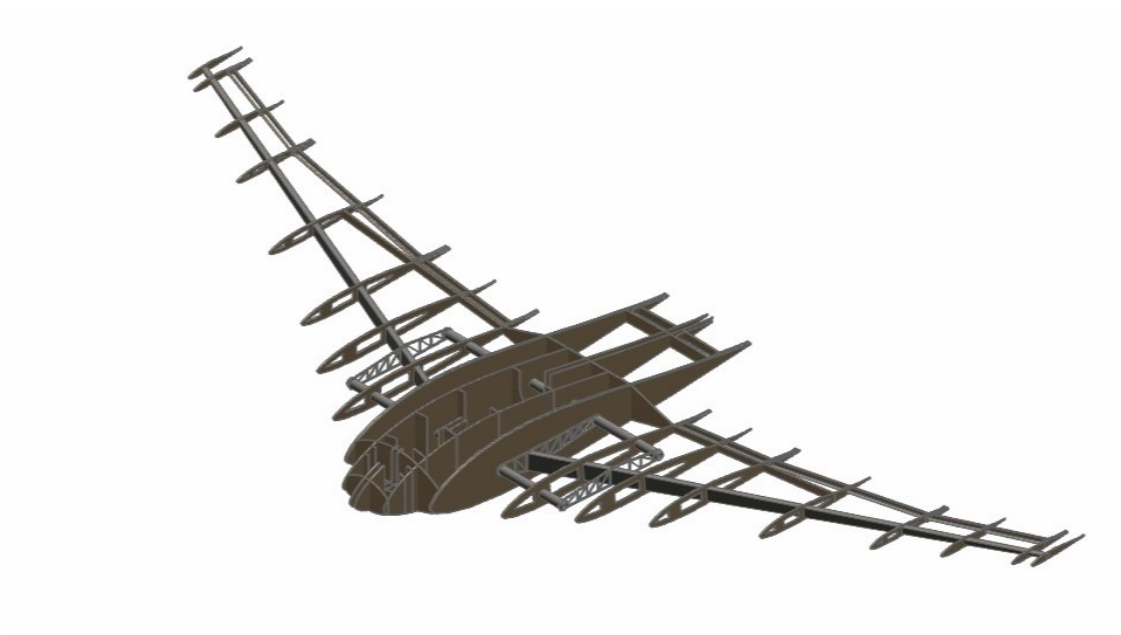


Figure 2.16: Internal structure of the Green Raven

Chapter 3

Aerodynamic Loads

3.1 Flight Envelope

The sizing of the main structural elements must be carried out considering the most critical loading condition that can occur during all phases of flight. To determine the most critical flight conditions, reference is made to the load factor n , that, defined as the ratio between the total lift acting on the lifting surfaces and the overall weight of the aircraft:

$$n = \frac{L}{W} \quad (3.1)$$

represents a measure of the accelerations to which the aircraft is subjected during maneuvering phases. Since there is currently no specific regulation governing the design of drones, the V-N load diagram, which depicts the trend of the limit loads as a function of the airspeed is obtained following the EASA CS-VLA (Very light aircraft) standard [3]. This standard is applicable to single-engine aircraft with no more than two seats, a maximum certificated take-off weight of no more than 750 kg, and a stalling speed in the landing configuration of no more than 83 km/h. The load diagram is drawn starting from the definition of two characteristic speeds of the aircraft, the Never Exceed Speed (V_{NE}) and the Dive Speed (V_D), respectively, the maximum speeds at which the aircraft can fly without risking structural damage during normal flight and during dive. The Never Exceed Speed can be computed as:

$$V_{NE} = 1.3 \times V_c = 26 \text{ m/s} \quad (3.2)$$

and the Dive Speed is:

$$V_D = 1.4 \times V_c = 28 \text{ m/s}. \quad (3.3)$$

The EASA CS-VLA 337 standard EASA standards also require that in the absence of gust, the positive limit maneuvering load factor may not be less than 3.8, while, the negative limit maneuvering load factor may not be less than -1.5. These

constraints define the minimum and maximum values of the load factor during maneuvering under normal flight conditions. It is also necessary to exclude from the load diagram any maneuvers that cause the aircraft to stall, a condition in which, given the speed, the angle of attack is such as to cause separation of the aerodynamic flow and consequently a drastic reduction in lift. The positive and negative stall curves can be plotted by substituting into equation 3.1 the expression for lift as a function of airspeed:

$$L = \frac{1}{2}\rho SC_L V^2, \quad (3.4)$$

where $\rho = 1.225 \text{ kg/m}^3$ is the air density at sea level and $S = 2.87 \text{ m}^2$ is the planform area, by replacing the lift coefficient C_L with $C_{Lmax} = 0.9$ and C_{Lmin} respectively.

Since the aerodynamic analyses were carried out considering a positive angle of attack, it was not possible to determine the negative stall angle and the respective value of the minimum lift coefficient. For this reason, it was decided to consider the aerodynamic profile as if it were symmetric, so:

$$C_{Lmin} = -C_{Lmax}. \quad (3.5)$$

Due to the separation of the aerodynamic flow for high negative angles of attack, this approach overestimates the minimum lift coefficient, and the corresponding load factor values obtained from the maneuver diagram. However, since the most critical flight conditions for structural failure occur during pull-up maneuvers, characterized therefore by a positive load factor, only the positive portion of the diagram will be decisive for the determination of the maximum lift acting on the aircraft. The resulting diagram therefore does not define the maneuvers that the Green Raven is able to perform in downforce conditions, but it is essential to determine the loads applied to the structural elements in the most demanding flight conditions and their sizing. The base load diagram is obtained by intersecting the stall curves with the limits imposed on the maximum load factors, the dive speed and the stall speed in level flight conditions ($n=1$), given by:

$$V_s = \sqrt{\frac{2mg}{\rho_0 SC_{Lmax}}} = 12,45 \text{ m/s} \quad (3.6)$$

where $m = 25 \text{ kg}$ is the estimated total mass of the UAV and $g = 9.81 \text{ m/s}^2$ is the gravitational acceleration. The recalculated stall speed almost matches with the design requirement stall speed of 12 m/s. Table 3.2 shows the coordinates of the intersection points, through which it is possible to plot the load diagram in the absence of gust as shown in figure 3.1.

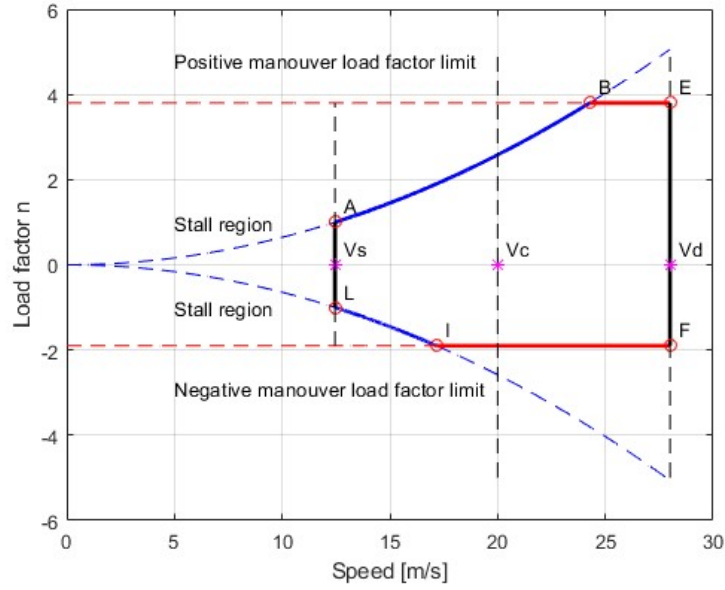


Figure 3.1: Maneuvering Envelope

Point	V [m/s]	n
0	0	0
A	12.45	1
B	24.27	3.8
E	28	3.8
F	12.45	-1
I	17.16	-1.9
L	28	-1.9

Table 3.1: Load diagram intersection points

The envelope diagram drawn, however, is incomplete, as it does not take into account the increases in lift to which the aircraft may be subjected due to symmetrical vertical gusts during the operational phase. Following the guidelines in CS-VLA 333, the load factor in the presence of gusts can be expressed as:

$$n = 1 \pm \frac{1/2\rho_0 V C_{L\alpha} K_g U_{de}}{mg/S} \quad (3.7)$$

where:

V is the aeroplane equivalent speed;

$C_{L\alpha} = 3.9$ [1/rad] is the wing lift curve slope;

$K_g = 0.88\mu_g/(5.3 + \mu_g) = 0.431$ is the gust alleviation factor;

$\mu_g = \frac{2m/S}{\rho_0 \bar{C} C_{L\alpha}} = 5.09$ is the aeroplane mass ratio;

$\bar{C} = \frac{S}{b} = 0.72$ m is the mean geometric chord;

U_{de} is the derived gust velocity

considering a gust speed of 15.24 m/s over the interval $V = [0 - V_c]$ and a gust speed of 7.62 m/s over the interval $V = [0 - V_d]$. Given the gust lines, we can determine the coordinates of the characteristic points of the gust diagram, as reported in table 3.2.

Point	V [m/s]	n
M	V_c	4.67
N	V_d	3.57
P	V_c	-1.57
Q	V_d	-2.67

Table 3.2: Gust diagram intersection points

The airworthiness also specifies that the gust load must vary linearly between the speeds V_c and V_d . Consequently, connecting the points M and N and the points Q and P through linear functions we obtain the gust diagram of the aircraft shown in figure 3.2.

By superimposing the maneuver and gust diagrams we obtain the aircraft envelope diagram as shown in figure 3.3, through which, for each airspeed, it is possible to determine the minimum and maximum total lift acting on the aircraft during all flight phases.

The coordinates of the intersection points C, D, G and H between the two graphs are: C(24.86;4), D(26.31;3.8), G(25.59;-1.9), H(20.2;-2.64). From the envelope diagram it is clear that point C is characterized by the highest load factor, consequently representing the most critical aerodynamic condition for the aircraft. Therefore the sizing of the structural elements must be carried out considering a total lift acting on the aircraft equal to:

$$L = 4mg. \tag{3.8}$$

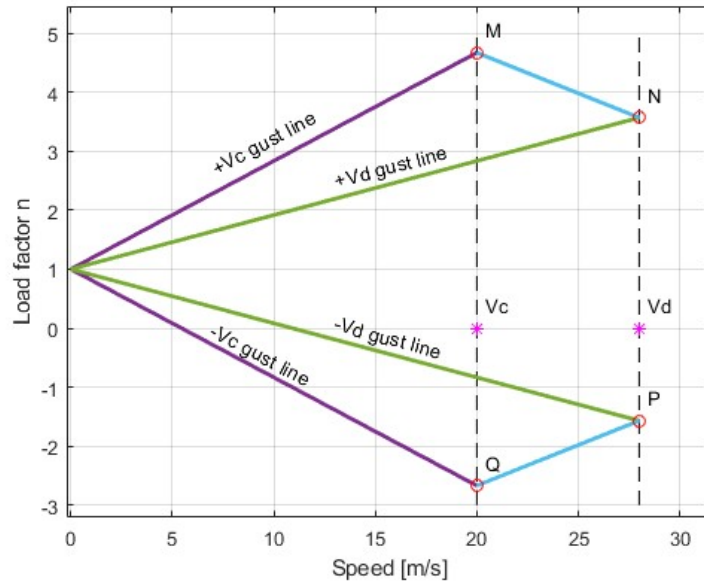


Figure 3.2: Gust Envelope

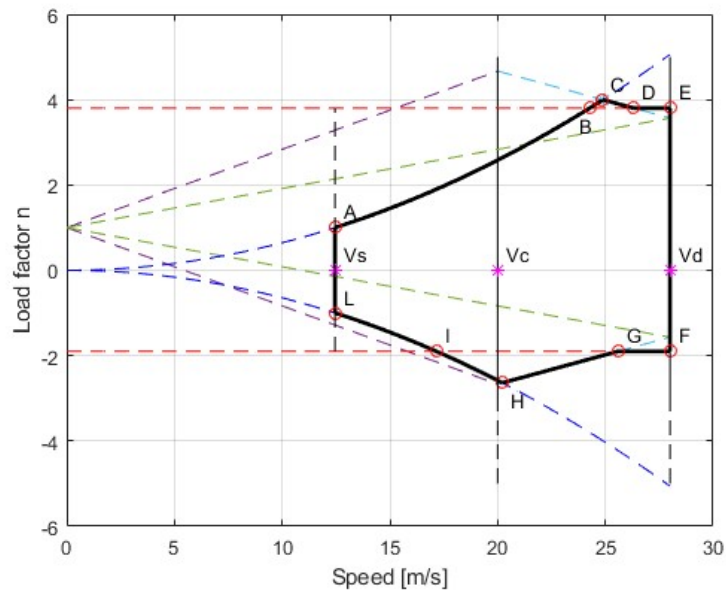


Figure 3.3: Flight Envelope

3.2 Aerodynamic Loads Calculation

Using the xlr software, the team responsible for the aerodynamic analysis was able to determine the lift and resistance characteristics of the aircraft starting from its external geometry, for a cruise speed of 20 m/s and an angle of attack of 8° . In addition to the total loads acting on the lifting surfaces in these conditions, the trend of the lift coefficient as well as the distance between the leading edge and the center of pressure of the corresponding aerodynamic profile along the wingspan were also reported, as shown in figures 3.4.

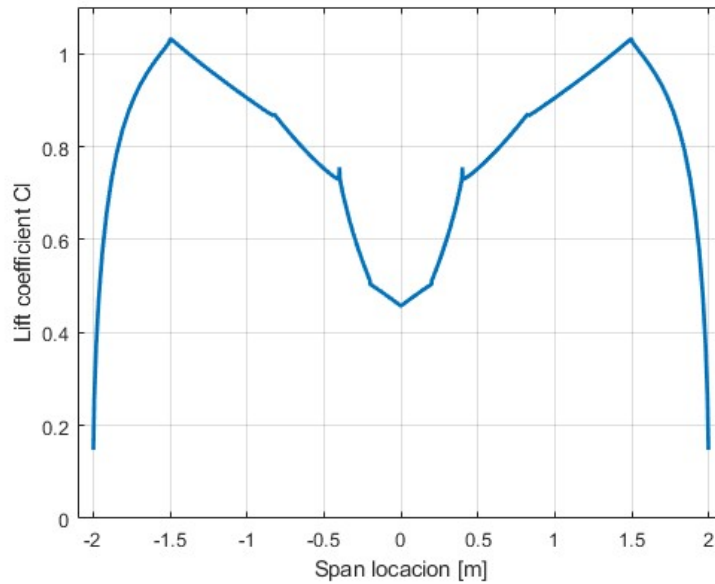


Figure 3.4: Lift coefficient along the span

Substituting equation 3.8 into the lift expression 3.4, and by maintaining the same angle of attack as in the aerodynamic analysis to preserve the lift coefficient:

$$C_L = C_{L\alpha} \cdot \alpha = 0,733346$$

the speed corresponding to the most critical flight condition for the Green Raven is given by:

$$V_{n=4} = \sqrt{\frac{4mg}{\frac{1}{2}\rho S C_L}} = 27.6 \text{ m/s} \quad (3.9)$$

Consequently, the lift distribution per unit length along the wingspan is expressed as:

$$dL(y) = \frac{1}{2}c(y)C_i(y)V_{n=4}^2 \quad (3.10)$$

where $c(y)$ represents the aerodynamic chord of the airfoil. The lift distribution is shown in Figure: 3.5.

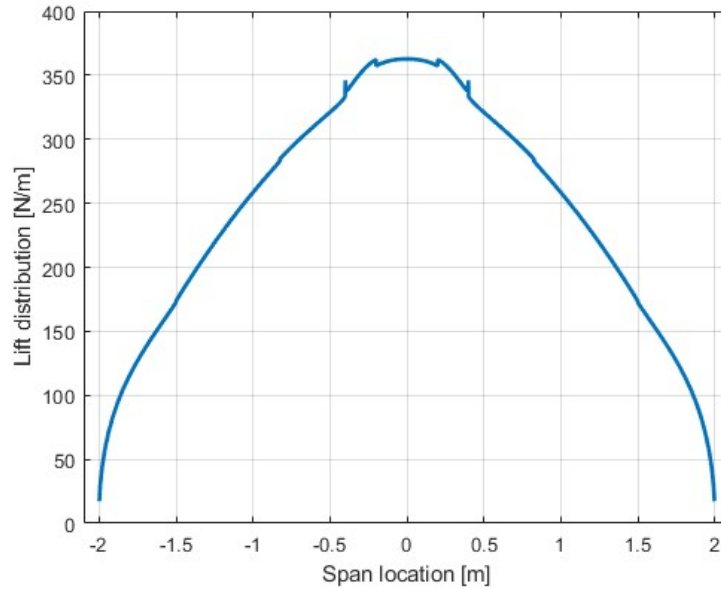


Figure 3.5: Lift distribution

To verify the accuracy of the results obtained, the trapz function in MATLAB was used. In this case, the distribution of nodes along the span corresponds to that provided by the aerodynamic analysis team, characterized by 240 nodes distributed symmetrically but not uniformly along the wing. The total lift obtained using the trapezoidal method is:

$$L = \int_{-2}^2 dL(y)dy = 980.6 \text{ N} \quad (3.11)$$

corresponding exactly to four times the aircraft's maximum weight.

Chapter 4

Material Selection for Structural Components

4.1 Advantages of Composite Materials

In the design of modern aircraft, the choice of materials plays a critical role, as it not only defines the rigidity characteristics and weight of the structure, but also significantly impacts the production processes of the components and costs. For the Green Raven project, given the requirements imposed on the maximum weight of the structure, it was decided to use almost exclusively composite materials and in particular carbon fiber reinforced epoxy. The choice of this material for the design of the main structural elements such as the wing spars and the cylindrical beams is essentially guided by its exceptional strength-to-weight ratio due to the high tensile strength of carbon fiber and the polymer matrices low density, characteristics which make it suitable for supporting high loads while reducing the overall weight. The use of composite materials is mainly aimed at designing a structure that meets the stringent Maximum Take-off Weight (MTOW) requirement imposed by the certification standards. In fact, in addition to the high strength to weight ratio, composite materials have a further advantage since, unlike traditional materials such as aluminum that exhibit uniform properties in all directions, they can be designed with anisotropic properties, which allows to optimize the structural strength and stiffness in specific directions by aligning the fibers along the load path of the components. This customization of mechanical properties ensures that the UAV's structural components are both strong and efficient, allowing for optimized load-bearing.

Although this project focuses on the design of the green raven structure under static loading conditions, it is important to consider that the choice of material directly impacts the fatigue strength of the structural elements. The phenomenon

of fatigue involves a gradual deterioration of the material over time due to cyclic loads applied to the structure and represents a major concern in structural design as it can lead to the structural failure of the components even when the applied loads are such as not to exceed the stiffness limits of the material. Carbon fiber reinforced polymers, exhibit excellent fatigue resistance compared to traditional metals. This property is crucial for UAVs, which are subjected to continuous loading and unloading during flight maneuvers due to the variation in aerodynamic loads. In the case of Green Raven, the enhanced fatigue resistance of carbon fiber composites ensures that the structural elements can withstand the repeated stresses without suffering from fatigue-induced cracks or failures.

In addition to high mechanical performance, composite materials offer high corrosion resistance which preserves the structure from environmental degradation. As reported by Anwar and Li [4], unlike metal structures that require anti-corrosion treatments or coatings to prevent material deterioration, in composites the epoxy matrix acts as a protective layer that shields the fibers from oxidation and corrosion, making them ideal for long-term use in aerospace applications. For the Green Raven UAV, which may be deployed in varying climates and weather conditions, the use of corrosion-resistant materials reduces maintenance costs and extends the service life of the aircraft.

The major disadvantages resulting from the use of composite materials in structural design are mainly attributable to a greater complexity of the production processes arising from the layering and curing process. The major critical issues emerging during the manufacturing of components lie in the development of out-of-plane wrinkles [5], a phenomenon that causes a reduction in the mechanical characteristics of the component and shape distortion [6], due to the development of residual stresses during the curing process. In addition to a greater construction complexity, composites, although offering superior mechanical properties, tend to be more expensive compared to traditional materials like aluminum or steel, resulting in a drive up of the overall production costs and time.

4.2 Wing Spars and Cylindrical beams

As previously reported, when designing structural elements made of composite materials, the choice of the lamination sequence directly impacts the component stiffness and weight, as it allows for strategically reinforcing the structure in specific directions. In the case under consideration, the loads acting on the wings will be distributed on the spars, which will induce shear stresses in the cross-section section as well as normal stresses due to the bending moment. The main contribution to the bending stiffness of a rectangular beam is given by the flanges, which are mainly loaded in compression and tension along the beam's longitudinal axis, while

the walls primarily absorb shear loads, meaning that the stiffness in the walls must be distributed more evenly in both directions within the plane of the panel.

Similarly, the two cylindrical beams are designed to absorb concentrated shear loads arising from the restraints applied to the spars and the fuselage. Such loading conditions cause the beams to exhibit regions that primarily experience tensile and compressive loads, as well as regions that are primarily subjected to shear forces, but, their uniform and continuous geometry makes it unfeasible to design two different stacking sequences as for the rectangular beams. Consequently a single layup capable of withstanding both normal and shear stresses must be designed.

Therefore, all composite structural elements must be made by combining layers designed to absorb compressive loads obtained by arranging the fibers parallel to the direction of the load and layers whose fibers are arranged at $\pm 45^\circ$ to effectively resist shear stresses. In layers responsible for absorbing normal loads, unidirectional carbon fiber plies were used, characterized by a high modulus of elasticity and high resistance loads in the direction of the fibers, while plain weave carbon fiber plies were chosen to handle shear loads. Since the properties of individual plies vary according to the characteristics of the fibers and matrix, the volume fraction of the fibers as well as the manufacturing process, the rapid development of these materials has made a wide variety of options available. For this project, the TORAY 2510 prepreg system [7] has been selected, which provides a detailed technical data sheet describing the properties of the laminates. These properties, for both unidirectional (PART NUMBER: P707AG-15, CTA) and plain weave laminates (PART NUMBER: F6273C-07M, CTA), are listed in Table 4.1.

As reported by Wang et al. [8], the choice of the lamination sequence cannot be made only on the basis of the loading conditions of the laminate, but should follow, as far as possible, a set of design rules, which helps prevent the development of interlaminar stresses, and to increase the local buckling strength.

These rules include:

1. In order to avoid the matrix loading, the minimum amount of plies in each direction should be at least 10%;
2. In order to minimize interlaminar stress, grouping of -45° and 45° plies in adjacent layers should be avoided, separated by a 0° or 90° ply. Similarly, grouping 0° and 90° plies in adjacent layers should be avoided, separated by a -45° or 45° ply;
3. In order to minimize interlaminar stress, grouping of $\pm 45^\circ$ plies in adjacent layers should be avoided, separated by a 0° or 90° ply;
4. Grouping of a maximum of four plies in the same direction is allowed in a stack;

5. Avoid grouping of 90° plies in adjacent layers, which should be separated by 0°, -45°, or 45° plies;
6. The first ply and the last ply of the stack should be -45°, which can improve the local buckling strength and laminate strength.

Property	Symbol	Unidirectional	Plain wave
0° Tensile Strength [MPa]	F_{1t}	1682	803
90° Tensile Strength [MPa]	F_{2t}	52.9	722
0° Tensile Modulus [GPa]	E_{1t}	128	57.1
90° Tensile Modulus [GPa]	E_{2t}	9.03	56.4
0° Compressive Strength [MPa]	F_{1c}	1400	750
90° Compressive Strength [MPa]	F_{2c}	283	742
0° Compressive Modulus [GPa]	E_{1c}	114	54.8
90° Compressive Modulus [GPa]	E_{2c}	14.1	48.7
In-Plane Shear Strength [MPa]	F_{12}	159	155
In-Plane Shear Modulus [GPa]	G_{12}	5.22	4.3
Poisson's Ratio	ν	0.35	0.09
Laminate Density kg/m ³	ρ	1517	1502
Fiber Volume Fraction [%]	V_f	54.4	49.6
Cured Ply Thickness [mm]	t_p	0.152	0.218

Table 4.1: Unidirectional and Plain wave laminate mechanical properties

Finally, by examining the relationship between in-plane forces and moments and the strains for thin laminates:

$$\begin{pmatrix} N_\xi \\ N_\eta \\ N_{\xi\eta} \\ M_\xi \\ M_\eta \\ M_{\xi\eta} \end{pmatrix} = \begin{bmatrix} A_{11} & A_{12} & A_{16} & B_{11} & B_{12} & B_{16} \\ A_{12} & A_{22} & A_{26} & B_{12} & B_{22} & B_{26} \\ A_{16} & A_{26} & A_{66} & B_{16} & B_{26} & B_{66} \\ B_{11} & B_{12} & B_{16} & D_{11} & D_{12} & D_{16} \\ B_{12} & B_{22} & B_{26} & D_{12} & D_{22} & D_{26} \\ B_{16} & B_{26} & B_{66} & D_{16} & D_{21} & D_{66} \end{bmatrix} \begin{pmatrix} \epsilon_\xi^0 \\ \epsilon_\eta^0 \\ \gamma_{\xi\eta}^0 \\ \kappa_\xi \\ \kappa_\eta \\ \kappa_{\xi\eta} \end{pmatrix} \quad (4.1)$$

where

$$\begin{aligned} A_{ij} [N/m] &= \sum_{k=1}^K (Q_{ij})_k (z_k - z_{k-1}) \\ B_{ij} [N] &= \frac{1}{2} \sum_{k=1}^K (Q_{ij})_k (z_k^2 - z_{k-1}^2) \\ D_{ij} [Nm] &= \frac{1}{3} \sum_{k=1}^K (Q_{ij})_k (z_k^3 - z_{k-1}^3) \end{aligned} \quad (4.2)$$

are the stiffness matrices of the entire laminate, K is the total number of plies, z_k and z_{k-1} are the distances from the reference plane to the two surfaces of the k^{th} ply and $(Q_{ij})_k$ are the elements in the stiffness matrix of the "k-th" ply. We can observe that, in the general case, there are in-plane-out-of-plane, extension-shear, and bend-twist coupling effects. The ξ , η , and ζ refer to a coordinate system relative to each laminate where the ξ and η coordinates lie on a chosen reference plane (the midplane of the laminate), and the ζ -axis is perpendicular to this reference plane. As a result, due to the anisotropic nature of composite laminates, under certain loading conditions, in-plane forces can induce out-of-plane deformations, shear forces can cause extensional deformations, and bending moments can produce torsions of the laminate. These coupling effects can be avoided by selecting a symmetric and balanced stacking sequence and making the laminate orthotropic. In a symmetric laminate (i.e., if the laminate is symmetric about the midplane), the matrix $[B]$ becomes zero, avoiding the development of in-plane-out-of-plane coupling effects. Similarly, if the laminate is balanced (i.e., for every ply oriented in the $+\theta$ direction, there is an identical ply in the $-\theta$ direction), the stiffness matrix elements A_{16} and A_{26} are zero, thus eliminating any extension-shear coupling effects. Finally, if the laminate is orthotropic, i.e., each layer is orthotropic and meets the following conditions:

1. the ply is made of unidirectional fibers and all the fibers are aligned with one of the laminate's orthotropy directions;
2. the ply is a woven fabric and the ply's symmetry axes are aligned with the laminate's orthotropy directions;
3. two adjacent unidirectional plies (oriented in different directions) are treated as a single layer and the symmetry axes of this layer are aligned with the laminate's orthotropy directions;

the elements D_{16} and D_{26} are zero and there is no bend-twist coupling.

The sizing of the components was carried out by defining an initial stacking sequence, taking into account both the need to align the fibers with the load direction and adherence to composite design rules. Moreover, to avoid the structure appearing flimsy, it was decided to impose a minimum thickness of 1 mm on the laminates. Once the initial stacking sequence was defined, FEM analysis was used to determine the maximum stresses in each component, iteratively adding further layers if the stresses were such as to lead to structural failure of the component, modifying the stacking sequence where necessary to optimize performance. An initial layup of 6 layers was chosen for the spar flanges, comprising 4 UD layers aligned at 0° to increase the bending stiffness and 2 plain weave layers oriented at 45° relative to the beam's longitudinal axis, to carry the shear load due to torsion. To ensure that the laminate is both symmetrical and balanced, the selected

stacking sequence is $(0/45/0)_s$, providing a total thickness of approximately 1.044 mm. The same layup was chosen for the design of the two cylinders, since they face compressive loads in the top and bottom regions and shear loads in the lateral areas. For the spar webs, which are primarily subjected to shear loads, an initial layup of 5 layers of plain weave carbon fiber was selected. The stacking sequence is $(45/0/45/0/45)$, resulting in a total thickness of 1.09 mm. Following the guidelines given by Kollár & Springer [9], the stress-strain relationship for a thin walled plate under plane-stress conditions can be written as:

$$\begin{pmatrix} \sigma_x \\ \sigma_y \\ \sigma_{xy} \end{pmatrix} = \begin{bmatrix} Q_{11} & Q_{12} & Q_{16} \\ Q_{12} & Q_{22} & Q_{26} \\ Q_{16} & Q_{26} & Q_{66} \end{bmatrix} \begin{pmatrix} \epsilon_x \\ \epsilon_y \\ \gamma_{xy} \end{pmatrix}. \quad (4.3)$$

The stiffness matrix $[Q]$ in terms of the engineering constants for an orthotropic material is given by:

$$[Q] = \begin{bmatrix} \frac{E_1}{D} & \frac{\nu_{12}E_2}{D} & 0 \\ \frac{\nu_{12}E_2}{D} & \frac{E_2}{D} & 0 \\ 0 & 0 & G_{12} \end{bmatrix} \quad (4.4)$$

where:

$$D = 1 - \frac{E_2}{E_1} \nu_{12}^2. \quad (4.5)$$

The resulting stiffness matrices of the plies in the principal directions for the UD layers and the plain wave layers are:

$$[Q]_{UD_0} = \begin{pmatrix} 129 & 3.19 & 0 \\ 3.19 & 9.11 & 0 \\ 0 & 0 & 5.22 \end{pmatrix} \times 10^9 \frac{N}{m^2} \quad (4.6)$$

$$[Q]_{PW_0} = \begin{pmatrix} 56.9 & 5.12 & 0 \\ 5.12 & 56.9 & 0 \\ 0 & 0 & 4.3 \end{pmatrix} \times 10^9 \frac{N}{m^2}. \quad (4.7)$$

The stiffness matrix of a ply oriented at an angle θ with respect to the reference direction of a laminate is obtained through the relationship:

$$[\bar{Q}] = [T_\sigma]^{-1} [Q] [T_\epsilon] \quad (4.8)$$

where the transformation matrices are:

$$[T_\sigma] = \begin{bmatrix} c^2 & s^2 & 2cs \\ s^2 & c^2 & -2cs \\ -cs & cs & c^2 - s^2 \end{bmatrix} \quad [T_\epsilon] = \begin{bmatrix} c^2 & s^2 & cs \\ s^2 & c^2 & -cs \\ -2cs & 2cs & c^2 - s^2 \end{bmatrix} \quad (4.9)$$

and $c = \cos(\theta)$, $s = \sin(\theta)$. The stiffness matrix of the plain wave layers, oriented at $\pm 45^\circ$ is so obtained:

$$[Q]_{PW_{45}} = \begin{pmatrix} 35.3 & 26.7 & 0 \\ 26.7 & 35.3 & 0 \\ 0 & 0 & 2.59 \end{pmatrix} 10^9 \frac{N}{m^2}. \quad (4.10)$$

Given the ply stiffness matrices, equation 4.2 allows to determine the ABD_f and ABD_w matrices of the 2 laminates constituting the flanges (and the cylindrical beams) and the webs of the spar respectively:

$$ABD_f = \begin{pmatrix} 0.939 \times 10^8 & 0.136 \times 10^8 & 0 & 0 & 0 & 0 \\ 0.136 \times 10^8 & 0.209 \times 10^8 & 0 & 0 & 0 & 0 \\ 0 & 0 & 0.145 \times 10^8 & 0 & 0 & 0 \\ 0 & 0 & 0 & 9.29 & 1.04 & 0 \\ 0 & 0 & 0 & 1.04 & 1.69 & 0 \\ 0 & 0 & 0 & 0 & 0 & 1.14 \end{pmatrix}; \quad (4.11)$$

$$ABD_w = \begin{pmatrix} 0.479 \times 10^8 & 0.197 \times 10^8 & 0 & 0 & 0 & 0 \\ 0.197 \times 10^8 & 0.479 \times 10^8 & 0 & 0 & 0 & 0 \\ 0 & 0 & 0.188 \times 10^8 & 0 & 0 & 0 \\ 0 & 0 & 0 & 4.29 & 2.40 & 0 \\ 0 & 0 & 0 & 2.40 & 4.29 & 0 \\ 0 & 0 & 0 & 0 & 0 & 2.31 \end{pmatrix}. \quad (4.12)$$

4.3 Sandwich Panels

For the design of the fuselage main structure, the wing ribs, the false spar and control surfaces, as reported in Chapter 2, it was decided to use sandwich panels. The choice of the lamination sequence of the external faces of the panels was also made considering both the load conditions and the design rules for composite laminates. Since the panels are primarily responsible for transferring shear loads, it was chosen to use only plain weave carbon fiber plies on the external faces. The initial configuration was designed such that each of the two faces of the panel is composed of a ply, the outermost one, oriented at 45° and a ply, in contact with the core, oriented at 0° with respect to the reference direction of the laminate. For the core material we chose to use Divinycell H80, produced by the Diab company [10], a polyvinyl chloride foam that provides excellent mechanical properties to low weight. According to Zenkert [11], PVC foams are used in almost every type of sandwich application and are hence the most widely used of all core material. The Divinycell H is ideal for applications subject to fatigue, slamming or impact loads. Other key features of Divinycell H include consistent high quality, excellent

adhesion/peel strength, excellent chemical resistance, low water absorption and good thermal/acoustic insulation. Divinycell H is also compatible with virtually all commonly used resin and manufacturing systems. The mechanical characteristics of the material depend on its density and for this project it was decided to select Divinycell H80 (where 80 indicates the density of the core in kg/m^3), as it represents a good compromise between lightness and mechanical properties. Material data are presented in table 4.2.

Property	Test Procedure	Unit	Nominal	Minimum
Compressive Strength	ASTM D 1621	MPa	1.4	1.15
Compressive Modulus	ASTM D1621-B-73	MPa	90	80
Tensile Strength	ASTM D 1623	MPa	2.5	2.2
Tensile Modulus	ASTM D 1623	MPa	95	85
Shear Strength	ASTM C 273	MPa	1.15	0.95
Shear Modulus	ASTM C 273	MPa	27	23
Shear Strain	ASTM C 273	%	30	
Density	ISO 845	kg/m^3	80	
Poissons ratio			0.4	

Table 4.2: Technical characteristics DIVINYCELL H 80

Assuming an initial core thickness of 5 mm knowing that each woven carbon fiber ply is 0.218 mm thick, we obtain a total panel thickness of 5.87 mm and a density per unit surface area of 1.35 kg/m^2 . The weight of the core only affects 3% of the total weight of the panels, meaning that, in the case in which the contact surface between the ribs and the spar is not sufficient to guarantee effective bonding, it is possible to increase the thickness of the core without significantly impacting the overall weight.

4.4 Truss Structures

The truss structures are made of aerospace-grade aluminum, chosen for its high strength-to-weight ratio and ability to withstand high concentrated loads. This is the only component of the structure made of aluminum, since the truss structure, being the component responsible for transferring all the aerodynamic loads applied to the wing to the cylindrical beams, is subjected to considerable concentrated forces and requires materials capable of withstanding high mechanical stresses, while keeping the weight low. The properties of the 7075-T6 aluminum alloy according to the data provided by MatWeb [12] are reported in table 4.3. Given the high mechanical performance and the ability to withstand concentrated loads,

aluminum was also chosen for the manufacturing of the flanged bushings and the rods of the control surfaces.

Property	Symbol	Unidirectional
Modulus of elasticity [GPa]	E	71,7
Ultimate Tensile Strength [MPa]	F_{1t}	572
Tensile Yield Strength [MPa]	F_{1t}	503
Shear Strength [MPa]	F_{12}	331
Shear Modulus [GPa]	G_{12}	26,9
Poisson's Ratio	ν	0.33
Density kg/m ³	ρ	2810

Table 4.3: Alluminum 7075-T6 mechanical properties

Chapter 5

Structural Analysis of Wing Components

The sizing and structural analysis of components represents a crucial phase during the design of aerospace structures. In this and the next chapter, the methods used to perform the structural analysis of the wing and fuselage components and the results obtained are presented. To perform the stress analysis, it was decided to employ Finite Element Analysis (FEA) as the primary tool, given the geometric complexity of the components, the use of composite materials and the complex load distribution, that are difficult to manage with analytical methods. FEA methods provide a detailed and precise overview, allowing for the accurate modeling and simulation of structural stresses. The stress determination was carried out following two slightly different approaches depending on the component to be analyzed. Specifically, critical structural elements such as the spar and cylindrical beams are analyzed in detail using a custom MATLAB finite element code. This approach offers the flexibility to quickly modify load and boundary conditions, as well as the geometric characteristics of the beams during the design phase. Additionally, unlike commonly used structural analysis software, this custom code allows for a more accurate representation of the lift distribution along the wing, eliminating the need for significant approximations.

For the other components, including the wing ribs, the fuselage main structure, and the wing-fuselage connection structures, Ansys software has been chosen for structural analysis. The complexity associated with their geometry and applied loads would otherwise make a detailed stress analysis infeasible or overly complicated.

It is important to specify that in this preliminary design phase, the structural weight has been intentionally excluded from the analysis. This decision stems from the fact that the weight effect, acting in the opposite direction to lift forces,

effectively reduces the total load on the structure. Although this alleviating effect is beneficial during the operational phase of the aircraft, lowering the maximum stresses on each component, accounting for the weight's relieving influence in the structural analysis presents a potential drawback. Future structural design adjustments may lead to a reduction in the structure's weight, which would, in turn, increase the total applied load. This could result in certain elements being undersized for the revised load condition.

5.1 Mathematical Model

The mathematical model underlying the Matlab code used to perform the structural analysis follows traditional FEM analysis methods, with the exception of considering the non-uniform properties of composite materials in different directions through the thickness. Consequently, the model must be adapted to accurately reflect these anisotropic characteristics. Nonetheless, as stated by Kollár & Springer [9], the strains (and consequently the displacements) of an orthotropic fiber-reinforced composite beam can be obtained by replacing, in the force-strain relationships:

$$\begin{pmatrix} N \\ M_y \\ M_z \\ T \end{pmatrix} = \begin{pmatrix} EA & 0 & 0 & 0 \\ 0 & EI_{xx} & EI_{xy} & 0 \\ 0 & EI_{xy} & EI_{yy} & 0 \\ 0 & 0 & 0 & GJ \end{pmatrix} \begin{pmatrix} \epsilon_z^0 \\ \frac{1}{D} \\ \frac{1}{D} \\ \frac{\rho_y}{\theta} \end{pmatrix}, \quad (5.1)$$

the traditional tensile EA , bending EI , and torsional GJ stiffness with the replacement stiffness:

$$\widehat{EA} = \int_{(s)} \frac{d_{11}}{D} d\eta \quad (5.2)$$

$$\widehat{EI}_{xx} = \int_{(s)} \left[\frac{d_{11}}{D} y^2 + \frac{a_{11}}{D} \cos^2 \alpha \right] d\eta \quad (5.3)$$

$$\widehat{EI}_{xy} = \int_{(s)} \left[\frac{d_{11}}{D} xy - \frac{a_{11}}{D} \cos \alpha \sin \alpha \right] d\eta \quad (5.4)$$

$$\widehat{GJ} = \frac{4A^2}{\oint a_{66} d\eta}, \quad (5.5)$$

where the x and y coordinates lie on the cross-section of the beam as shown in figure 5.11, the z -axis is perpendicular to the cross-section and α is the angle between the η -direction (which lies along the perimeter of the cross-section) and the x -axis. The elements of the $[a]$, $[b]$ and $[d]$ matrices are related to the $[A]$, $[B]$ and $[D]$ matrices by:

$$\begin{bmatrix} a_{11} & a_{12} & a_{16} & b_{11} & b_{12} & b_{16} \\ a_{12} & a_{22} & a_{26} & b_{21} & b_{22} & b_{26} \\ a_{16} & a_{26} & a_{66} & b_{61} & b_{62} & b_{66} \\ b_{11} & b_{21} & b_{61} & d_{11} & d_{12} & d_{16} \\ b_{12} & b_{22} & b_{62} & d_{12} & d_{22} & d_{26} \\ b_{16} & b_{26} & b_{66} & d_{16} & d_{26} & d_{66} \end{bmatrix} = \begin{bmatrix} A_{11} & A_{12} & A_{16} & B_{11} & B_{12} & B_{16} \\ A_{12} & A_{22} & A_{26} & B_{21} & B_{22} & B_{26} \\ A_{16} & A_{26} & A_{66} & B_{61} & B_{62} & B_{66} \\ B_{11} & B_{21} & B_{61} & D_{11} & D_{12} & D_{16} \\ B_{12} & B_{22} & B_{62} & D_{12} & D_{22} & D_{26} \\ B_{16} & B_{26} & B_{66} & D_{16} & D_{26} & D_{66} \end{bmatrix}^{-1}, \quad (5.6)$$

where

$$D = a_{11}d_{11} - b_{11}^2. \quad (5.7)$$

This holds true if shear deformations are negligible, making the Bernoulli-Navier assumptions valid, according to which the plane cross-sections remain plane and perpendicular to the beam's neutral axis during bending. According to Minera et al. [13], classical beam theories are sufficiently accurate for relatively slender beam structures (length to thickness ratio $L/t > 20$) and shear deformations can be neglected. The most relevant difference between isotropic and orthotropic beams lies in the stress determination. The calculation of the stresses in the beam can be divided into four steps:

1. Nodal displacement calculation obtained by substituting the replacing stiffness into the expression for the displacements of the corresponding isotropic beam;
2. Calculation of forces and moments acting on the cross-section by assuming the isotropic beam;
3. Determination of the force vector in each laminate, taking into account the anisotropic properties of the latter;
4. Determination of the strains and stresses in each layer of the laminate.

The calculation of the beam deformations follows the classical models of FEA of isotropic beams. For a detailed description of the method, please refer to Megson [14]. The mathematical model is based on the application of the virtual work principle to the governing equations of Euler's beam theory:

$$\frac{\partial^2}{\partial z^2} \left(EI \frac{\partial^2 w}{\partial z^2} - N_z w \right) + \rho A \frac{\partial^2 w}{\partial t^2} = q \quad (5.8)$$

and St. Venant's torsion theory:

$$q_T + \frac{\partial}{\partial z} \left[\left(GJ + N_z \frac{I_{0s}}{A} \right) \frac{\partial \theta}{\partial z} \right] - \rho I_{0s} \frac{\partial^2 \theta}{\partial t^2} = 0 \quad (5.9)$$

through which the so-called "weak formulation" of the governing equations is obtained. Unlike the governing equations of Euler's beam theory and St. Venant's

torsion theory, which are exact at every point in the domain, their respective weak formulations are exact only in the integral sense, implying that the solution is exact only in a few simple cases. In order to make the weak form of the equation of motion, more accurate, it's necessary to discretize the beam into multiple elements so that the weak form equations are satisfied not only over the entire domain but within each element. Therefore, a higher number of discretization elements leads to a more accurate solution to the problem. The weak formulation offers the significant advantage of approximating the beam deflection $w(z)$ along each element using a polynomial function, which can be expressed as the cross product of the deformation values at the nodes and the so-called shape functions:

$$w_e(z) = (N_{w1}, N_{w2}, N_{w3}, N_{w4}) \cdot (w_i, \varphi_i, w_{i+1}, \varphi_{i+1})^t = \mathbf{N}_w \mathbf{w}_e \quad (5.10)$$

where the subscripts i and $i+1$ represent the indices of the nodes associated with the element,

$$\varphi(z) = \partial w(z) / \partial z$$

is the displacement slope,

$$\mathbf{N}_w^t = \begin{pmatrix} N_{w1} \\ N_{w1} \\ N_{w1} \\ N_{w1} \end{pmatrix} = \begin{bmatrix} 1 - 3\frac{z^2}{h^2} + 2\frac{z^3}{h^3} \\ -x + 2\frac{z^2}{h} - \frac{z^3}{h} \\ 1 - 3\frac{z^2}{h} + 2\frac{z^3}{h} \\ 1 - 3\frac{z^2}{h} + 2\frac{z^3}{h} \end{bmatrix} \quad (5.11)$$

and h is the length of the element. Similarly twist deformations $\theta(z)$ can be expressed as:

$$\theta_e(x) = (N_{\theta1}, N_{\theta2}) \cdot (\theta_i, \theta_{i+1})^t = \mathbf{N}_\theta \boldsymbol{\theta}_e \quad (5.12)$$

where

$$\mathbf{N}_\theta^t = \begin{pmatrix} N_{\theta1} \\ N_{\theta2} \end{pmatrix} = \begin{bmatrix} 1 - 3\frac{z^2}{h^2} + 2\frac{z^3}{h^3} \\ -z + 2\frac{z^2}{h} - \frac{z^3}{h} \end{bmatrix}. \quad (5.13)$$

In this way, the problem of determining the polynomial coefficients for $w(z)$ and $\theta(z)$ is reduced to the determination of deformations at nodes. Inserting eq.5.1 and eq.5.12 into the weak form of the governing equations yields the matrix form of the problem:

$$\mathbf{K} \mathbf{v} + \mathbf{K}_\sigma \mathbf{v} + \mathbf{M} \ddot{\mathbf{v}} = \mathbf{F} \quad (5.14)$$

where \mathbf{K} and \mathbf{M} and are the stiffness matrices and the consistent mass matrix, \mathbf{K}_σ is the geometric stiffness matrix (which takes non-zero values only in the case

where the beam is subjected to compressive loads) , \mathbf{F} is the consistent vector of loads applied at nodes and \mathbf{v} is the displacements vector, obtained by assembling the displacement vectors of the individual elements:

$$\mathbf{v}_e = [\omega_i, \varphi_i, \theta_i, \omega_{i+1}, \varphi_{i+1}, \theta_{i+1}]. \quad (5.15)$$

As the goal of this project is to develop a preliminary design of the aircraft structure, the structural analysis will focus on determining the stresses caused by static lift loads. Therefore the previous equation can be simplified by omitting the dynamic term and the geometric stiffness matrix:

$$\mathbf{K}\mathbf{v} = \mathbf{f}. \quad (5.16)$$

The element stiffness matrix K_e , assuming constant beam stiffness characteristics along each element is defined by:

$$K_e = \begin{bmatrix} \frac{12EI}{h^3} & -\frac{6EI}{h^2} & 0 & -\frac{12EI}{h^3} & -\frac{6EI}{h^2} & 0 \\ -\frac{6EI}{h^2} & \frac{4EI}{h} & 0 & \frac{6EI}{h^2} & \frac{2EI}{h} & 0 \\ 0 & 0 & \frac{GJ}{h} & 0 & 0 & -\frac{GJ}{h} \\ -\frac{12EI}{h^3} & \frac{6EI}{h^2} & 0 & \frac{12EI}{h^3} & \frac{6EI}{h^2} & 0 \\ -\frac{6EI}{h^2} & \frac{2EI}{h} & 0 & \frac{6EI}{h^2} & \frac{4EI}{h} & 0 \\ 0 & 0 & -\frac{GJ}{h} & 0 & 0 & \frac{GJ}{h} \end{bmatrix}, \quad (5.17)$$

while the consistent load vector, assuming each element is subjected to a uniform distribution of transverse load q and torsional load q_t , is given by:

$$\mathbf{f}_e = \begin{bmatrix} \frac{qh}{2} + S_i \\ -\frac{qh^2}{12} + M_i \\ \frac{q_t h}{2} + T_i \\ \frac{qh}{2} + S_{i+1} \\ \frac{qh^2}{12} + M_{i+1} \\ \frac{q_t h}{2} + T_{i+1} \end{bmatrix}, \quad (5.18)$$

where S , M and T represent the potential concentrated loads of shear, bending moment and torsional moment, respectively.

The matrix equation 5.16 is therefore obtained by assembling the element stiffness matrices, load vectors and deformation vectors, taking into account that adjacent elements share three degrees of freedom (DOFs) at their common nodes. The resulting system of equations is singular since one of the properties of the stiffness matrix is that $\det(K) = 0$, which implies that the system has an infinite number of solutions. To obtain a unique solution, it is necessary to reduce the system by imposing a number of boundary conditions equal to the system's degrees of freedom.

However, solving the reduced system yields only the nodal deformations, while stress determination necessitates additional post-processing. From classical beam theory, the bending moment, the transverse force and the torsion distributions along each element can be calculated from:

$$M_x(z) = -EI \frac{d^2 w}{dz^2}$$

$$= -EI \left(-\frac{6}{h^2} + \frac{12z}{h^3}, \frac{4}{h} - \frac{6z}{h^2}, \frac{6}{h^2} - \frac{12z}{h^3}, \frac{2}{h} - \frac{6z}{h^2} \right) (w_i, \theta_i, w_{i+1}, \theta_{i+1})^t; \quad (5.19)$$

$$S_y(z) = \frac{dM}{dz} = -EI \left(\frac{12}{h^3}, -\frac{6}{h^2}, -\frac{12}{h^3}, -\frac{6}{h^2} \right) (w_i, \theta_i, w_{i+1}, \theta_{i+1})^t; \quad (5.20)$$

$$T(z) = GJ \frac{d\varphi}{dz} = GJ \left(-\frac{1}{h}, \frac{1}{h} \right) (\varphi_i, \varphi_{i+1})^t. \quad (5.21)$$

Since the beams have been designed using composite material, the determination of stresses and strains was carried out following the approach proposed by Kollár et al. [9], (Chapter 6). The analysis of each laminate is based on laminate plate theory and is formulated with certain approximations: strains are assumed to vary linearly across the laminate, shear deformations are considered negligible, and out-of-plane normal stress (σ_z) and shear stresses ($\tau_{\xi z}, \tau_{\eta z}$) are assumed small in comparison to in-plane stresses (σ_ξ, σ_η , and $\tau_{\xi\eta}$). Given the load condition acting on the cross-section, the vector of in-plane forces per unit length ($N_\xi, N_\eta, N_{\xi\eta}, M_\xi, M_\eta, M_{\xi\eta}$) acting on each orthotropic and symmetrical laminate reduces to:

$$N_\xi = \frac{M_x}{EI_{xx}} \frac{y}{a_{11}} \quad (5.22)$$

$$N_{\xi\eta} = q = q_b + q_t \quad (5.23)$$

$$M_\eta = \frac{M_x \cos\alpha}{EI_{xx}} \frac{d_{11}}{a_{11}}, \quad (5.24)$$

where $q_b = q_s + q_{s,0}$ represents the shear flow due to transverse load, being

$$q_s = -\frac{S_y}{EI_{xx}} \int_0^s \frac{y}{a_{11}} d\eta \quad (5.25)$$

the shear flow distribution supposing that the closed beam section is cut at some convenient point, thereby producing an open section beam loaded through its shear center, and

$$q_{s,0} = -\frac{\oint a_{66} q_s d\eta}{\oint a_{66} d\eta} \quad (5.26)$$

is the value of the constant shear flow at the cut, while

$$q_t = \frac{M_z}{2A(z)} \quad (5.27)$$

is the shear flow due to torsion, where A represents the enclosed area. Starting from the generalized strain-force relationships:

$$\begin{pmatrix} \epsilon_\xi^0 \\ \epsilon_\eta^0 \\ \gamma_{\xi\eta}^0 \\ \kappa_\xi \\ \kappa_\eta \\ \kappa_{\xi\eta} \end{pmatrix} = \begin{bmatrix} a_{11} & a_{12} & a_{16} & b_{11} & b_{12} & b_{16} \\ a_{12} & a_{22} & a_{26} & b_{21} & b_{22} & b_{26} \\ a_{16} & a_{26} & a_{66} & b_{61} & b_{62} & b_{66} \\ b_{11} & b_{21} & b_{61} & d_{11} & d_{12} & d_{16} \\ b_{12} & b_{22} & b_{62} & d_{12} & d_{22} & d_{26} \\ b_{16} & b_{26} & b_{66} & d_{16} & d_{26} & d_{66} \end{bmatrix} \begin{pmatrix} N_\xi \\ N_\eta \\ N_{\xi\eta} \\ M_\xi \\ M_\eta \\ M_{\xi\eta} \end{pmatrix} \quad (5.28)$$

given the in-plane force and moment vector, the strains and curvatures of the laminate's reference plane can be determined through equation 5.1. In accordance with the laminate plate theory, the strains at any point within the laminate are given by:

$$\begin{pmatrix} \epsilon_\xi \\ \epsilon_\eta \\ \gamma_{\xi\eta} \end{pmatrix} = \begin{pmatrix} \epsilon_\xi^0 \\ \epsilon_\eta^0 \\ \gamma_{\xi\eta}^0 \end{pmatrix} + \zeta \begin{pmatrix} \kappa_\xi \\ \kappa_\eta \\ \kappa_{\xi\eta} \end{pmatrix} \quad (5.29)$$

where ζ represents the distance from the reference plane. The stresses in each ply are finally obtained using the stress-strain relationships under plane-stress conditions:

$$\begin{pmatrix} \sigma_\xi \\ \sigma_\eta \\ \tau_{\xi\eta} \end{pmatrix} = [Q] \begin{pmatrix} \epsilon_\xi \\ \epsilon_\eta \\ \gamma_{\xi\eta} \end{pmatrix} \quad (5.30)$$

where the $[Q]$ matrix represents the stiffness matrix of the ply in the $\xi - \eta$ coordinate system.

5.2 Model Validation

The validation of the model was carried out by comparing the results obtained from the MATLAB program with those derived from the ANSYS software for a thin-walled, closed-section beam with constant dimensions along its span. The flanges and walls are composed of the same laminates used in the Green Raven's beam, while the load case has been simplified. Since the only differences between the beam under analysis and the simplified validation model lie in the geometric parameters and loading conditions, if results align, the model can be considered accurate and any variations in geometry or loading conditions should still yield

sufficiently reliable results. The validation beam is 1.92 m long (the same length of the designed beam), with its cross-section defined by a width of 20 mm and a height of 15 mm, so to simplify the analysis while still maintaining consistency with the structural properties of the original model. The beam is subjected to an upward shear force of 20 N at the upper-left corner of the tip cross-section. This load condition, due to the distance between the point where the load is applied and the cross-section's shear center, i.e. the point where a shear load does not induce any torsional effects on the beam, is particularly useful for confirming the model's accuracy in predicting the beam's behavior when subjected to combined shear and torsion. The beam is considered simply supported at $z = 0$ and $z = L/6$, where the z -axis is aligned with the longitudinal axis of the beam. Therefore, in both models, the displacements in the y -direction and the twist of the cross-section at these two points are constrained to be zero. Stress analysis using ANSYS software was performed following the steps below:

- Definition of the mechanical characteristics of UD and PW ply reported in table 4.1;
- Choice of shell element 181 as basis for structural analysis;
- Definition of the stacking sequences of the laminates characterizing the flanges and walls;
- Beam geometry definition;
- Surface mesh, through which the mechanical characteristics of the laminates are attributed to the flanges and walls;
- Definition of loads and constraints applied to the beam.

In order to correctly verify the accuracy of the model, the number of elements characterizing the mesh along the z -direction of the beam must be equal to the number of elements used in the MATLAB code. The comparison of the results obtained through the MATLAB program and the ANSYS software are shown in the following figures.

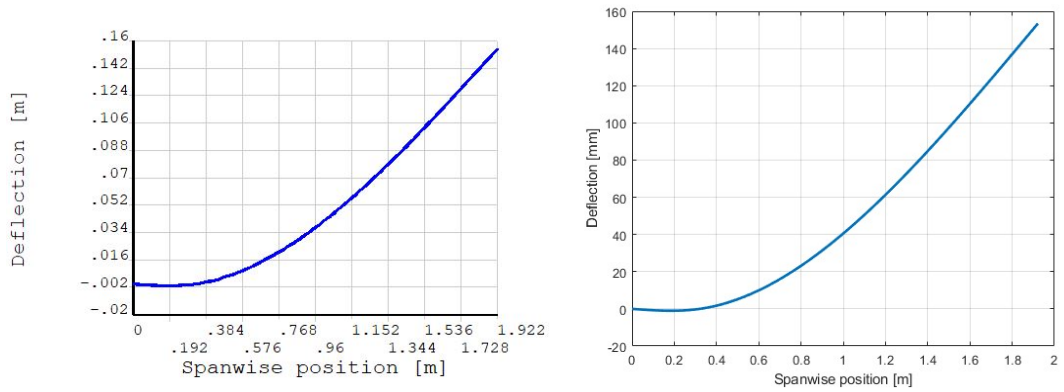


Figure 5.1: Displacements obtained with ANSYS (left) and MATLAB (right)

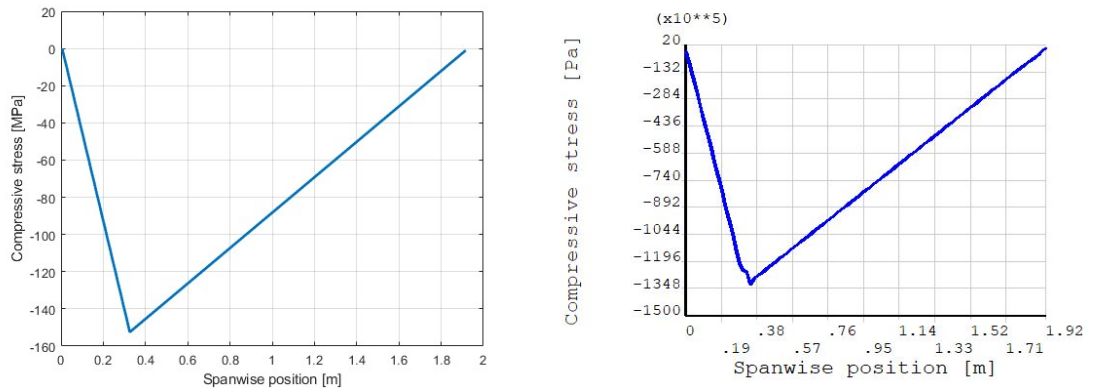


Figure 5.2: Normal stresses in the flanges obtained with ANSYS and MATLAB

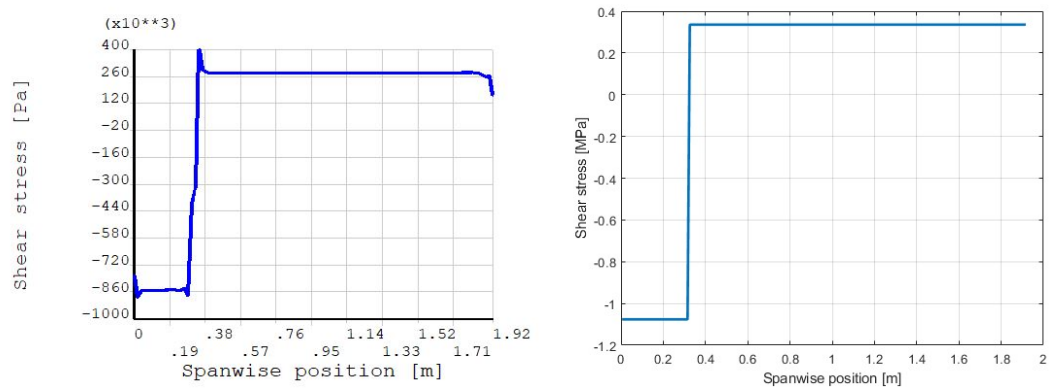


Figure 5.3: Shear stresses in the flanges obtained with ANSYS and MATLAB

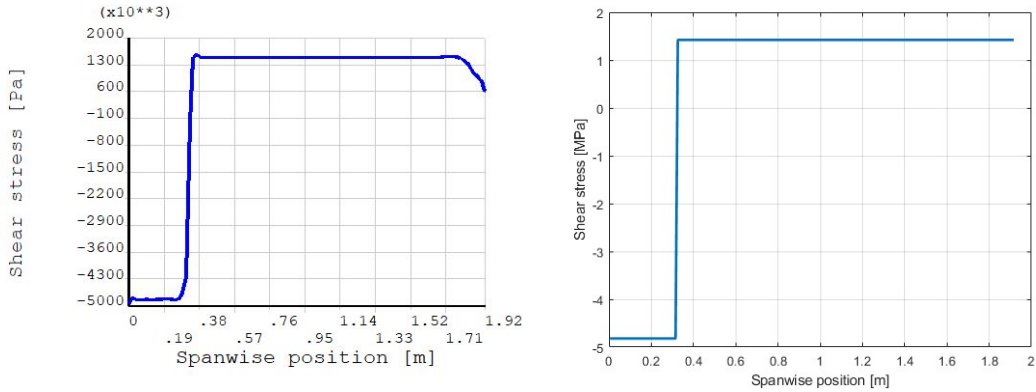


Figure 5.4: Shear stresses in the webs obtained with ANSYS and MATLAB

As shown in figure 5.1, the deformations of the beam are correct. From Figures 5.2, 5.3, and 5.4, it can be observed that while the stress trends obtained using the MATLAB code and the ANSYS software are consistent, the stress values computed with the MATLAB code are higher than those obtained with ANSYS. However, this is not due to an error in the program, but to the fact that the "PLOT PATH ITEM" command used to plot the stress trend along the beam shows the average value of the stresses through the thickness of the element, while the MATLAB code plots the trend of the maximum stresses. To obtain the values of the maximum stresses in the beam with ANSYS, the "PLOT" command was used, which allows to obtain the stress values for each layer. The results are reported in table 5.1, in which the maximum values of the stresses obtained are compared, as well as the deformations at the tip of the beam.

	MATLAB	ANSYS	error
Tip Deflection [mm]	153.42	154.4	0.6%
Tip Twist	0.222°	0.216°	2.7%
Maximum compressive stress in the flanges	152.5	153	0.33%
Maximum shear stress in the flanges	1.08	1.1	2%
Maximum shear stress in the webs	4.82	4.79	0.6%

Table 5.1: Model validation results

From the table, it can be observed that both the deformations and stresses calculated using the MATLAB code and the Ansys software are in agreement. Therefore, it can be concluded that neglecting shear deformation as well as considering plane stress conditions does not significantly impact the results and the model is valid for structural analysis.

5.3 Wing Spar Analysis

The structural analysis of the wing spar was carried out through the mathematical model described in the previous section. The main differences compared to the validation model lie in the geometry of the spar and the applied loads. Specifically, the cross-section features a height that varies linearly along the span, ranging from a value of $h_r = 70$ mm at the root to $h_t = 10$ mm at the tip. In order to ensure that a node is positioned at $z = L/6$, corresponding to the point of application of the constraints, it was decided to divide the beam into 180 elements. Through equations 5.3 and 5.5, the replacement stiffness of the spar along the span can be calculated:

$$\widehat{EI}(z) = \frac{bh(z)^2}{2a_f(1,1)} + 2\frac{b}{d_f(1,1)} + 2\frac{h(z)^3}{12a_w(1,1)} \quad (5.31)$$

$$\widehat{GJ}(z) = 2\frac{b^2h(z)^2}{a_f(3,3)b + a_w(3,3)h}. \quad (5.32)$$

Each element is therefore characterized by non-constant bending and torsional stiffness, while the element stiffness matrix was formulated by assuming constant cross-sectional properties. Consequently the stiffness values were approximated by taking the value at the midpoint of the element. The bending and torsional stiffness along the beam are shown in figure 5.5.

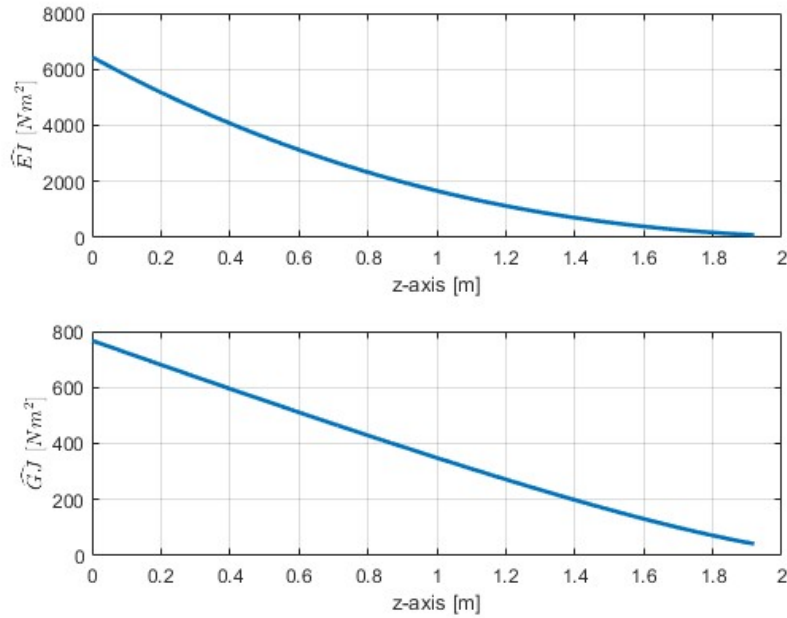


Figure 5.5: Bending and Torsional stiffness distribution

Since the spar's z -axis is inclined by an angle $\beta = 20.5^\circ$ with respect to the UAV's y_0 -axis, relative to which the lift forces have been determined (Figure 3.5), the relationship between the lift distribution along the y_0 -axis and the z -axis must be defined. The differential lift $dLdy_0$ must equal the redistributed lift along the spar's z -axis $dL'dz$, where $dz = dy_0/\cos(\beta)$. Therefore, the redistributed lift along the spar dL' is related to the original lift distribution by:

$$dL' = dL\cos(\beta). \quad (5.33)$$

The torsional moment distribution along the beam is obtained by multiplying the lift distribution dL' by the location of the center of pressure, defined as the point along the aerodynamic chord where the torsional moment is zero, with respect to the cross-section shear center. The distributions of transverse load and torsional moment are shown in figure 5.8.

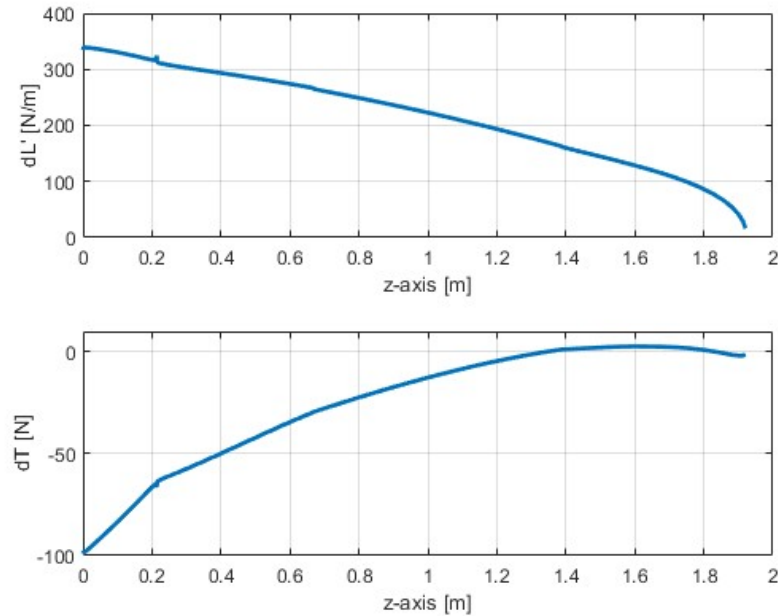


Figure 5.6: Lift and torsional moment distribution

As with the stiffness characteristics, the transverse load and torsional moment distributions acting on each element have been approximated by considering the value at the midpoint of the element. Given the stiffness properties and applied loads, the stiffness matrix and the consistent load vector for each element are obtained through equation 5.17 and 5.18 and are assembled to form the global stiffness matrix and the global load vector. By removing the equations associated with the constrained degrees of freedom from matrix equation 5.16, the reduced

system is obtained, the solution of which allows to obtain the displacement vector \mathbf{v} containing the transverse displacements, the cross-section rotations, and the twist of unconstrained nodes. The deformations of the beam are shown in figure 5.7.

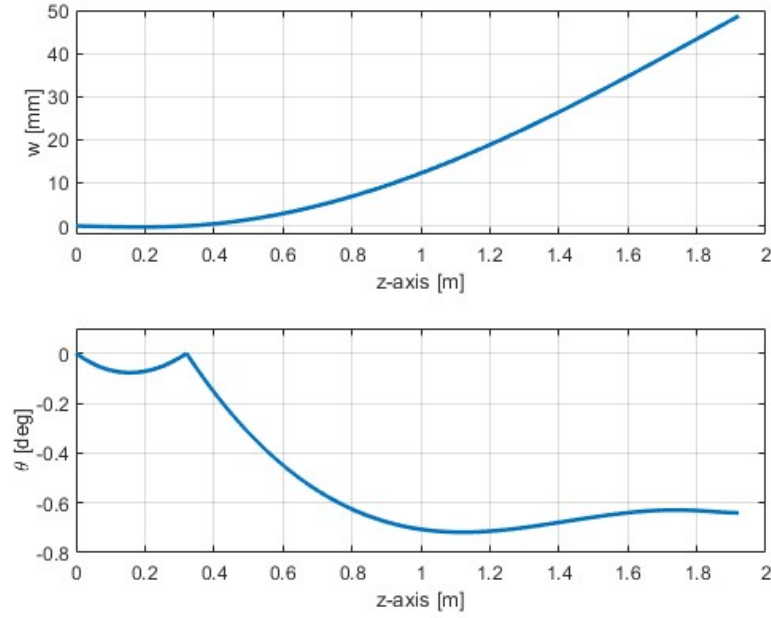


Figure 5.7: Wing spar deflection and twist

As an additional check to ensure the correct application of loads and proper solution of the problem, it was verified that the total lift and torsional load acting on the wing were in equilibrium with the reaction forces. The values of the latter can be determined by solving the system of equations

$$\mathbf{R} = \mathbf{K}\mathbf{v} - \mathbf{f} \quad (5.34)$$

and are reported below.

Reaction forces			Reaction moments		
Symbol	Constrained at	Value	Symbol	Constrained at	Value
Rf_1	$z = 0$	573.8 N	Rm_1	$z = 0$	13.5 Nm
Rf_2	$z = l/6$	-992.1 N	Rm_2	$z = l/6$	33.3 Nm

Table 5.2: Wing spar reaction forces and moments

The resultant total lift and torsional moment calculated are:

$$L = \int_0^l dL' dz = 418.3N \quad (5.35)$$

$$M_z = \int_0^l dM_z dz = -46.9 Nm. \quad (5.36)$$

Since both the sum of shear forces and the sum of torsional moments are zero, the beam is in equilibrium, and the solution of the system is therefore correct.

Finally, as outlined in section 5.1, the normal and shear stress distributions along the span were determined through post-processing. Following equations 5.19, 5.20, and 5.21, the distributions of the bending moment M_x , the shear load S_y , and the torsional moment T_z along the spar have been determined, as shown in figure 5.8.

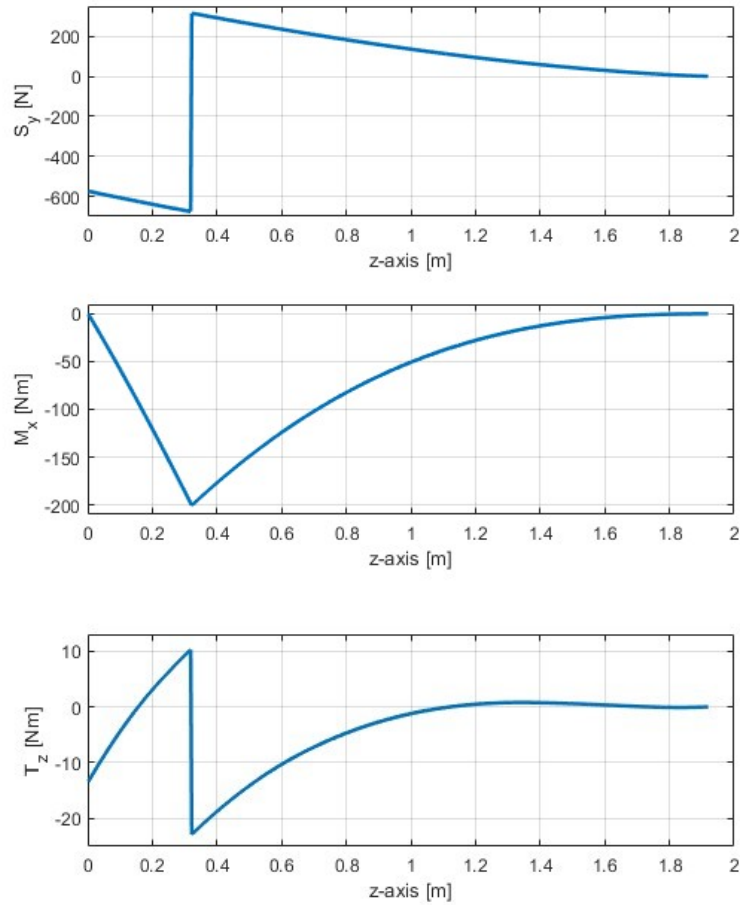


Figure 5.8: Transverse load, bending moment and torsional moment distribution

The vector of in-plane forces (N_ξ , $N_{\xi\eta}$, M_ξ) is given by equations 5.22, 5.23 and 5.24, where y is the coordinate of the most critical cross-section point, i.e. for both flanges and webs $y = h/2$. Since $\cos\alpha = 0$ in the webs and $\cos\alpha = 1$ in the flanges,

the vectors of in-plane forces can be written as:

$$\begin{pmatrix} N_\xi \\ N_{\xi\eta} \\ M_\xi \end{pmatrix}_f = \begin{pmatrix} \frac{M_z}{EI_{yy}} \frac{h}{2a_{11f}} \\ q_f \\ \frac{M_z}{EI_{yy}} \frac{1}{d_{11f}} \end{pmatrix} \quad (5.37)$$

$$\begin{pmatrix} N_\xi \\ N_{\xi\eta} \\ M_\xi \end{pmatrix}_w = \begin{pmatrix} \frac{M_z}{EI_{yy}} \frac{h}{2a_{11w}} \\ q_w \\ 0 \end{pmatrix}. \quad (5.38)$$

The axial force distribution in flanges $N_{\xi,f}$ and webs $N_{\xi,w}$ and the moment distribution $M_{\xi,f}$ in flanges are shown in figure 5.9 and 5.10 respectively.

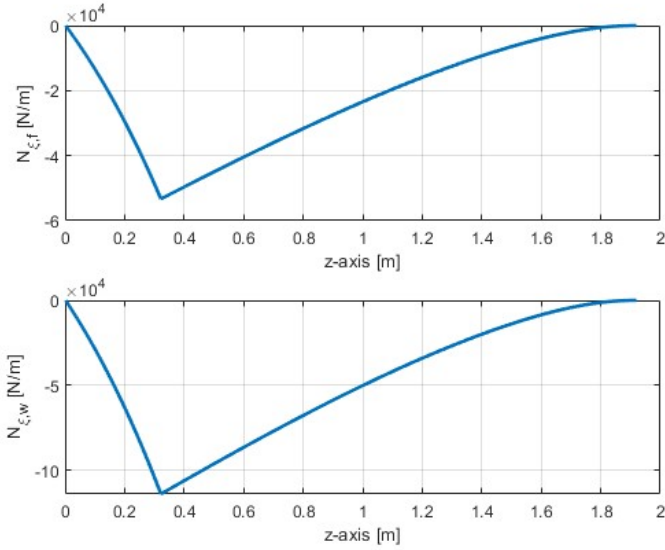


Figure 5.9: Axial force distribution in flanges (top) and webs (bottom) laminates

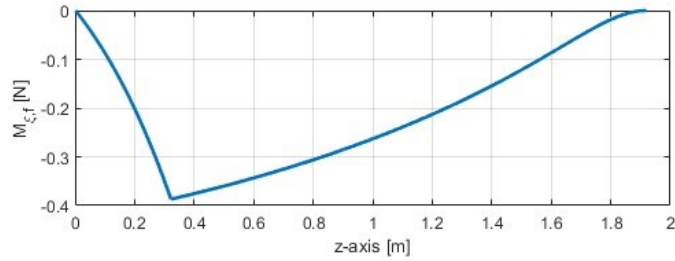


Figure 5.10: Moment distribution in flanges laminates

The maximum shear flows, q_f and q_w , are obtained by separately determining the shear flows due to both bending and torsion of the beam. The total shear flow is then calculated by appropriately summing these two contributions. The shear flow caused by bending is derived from equations 5.25 and 5.26. For convenience, it was chosen to consider the beam's cross-section to be open at the intersection with the positive y-axis, as shown in Figure 5.11.

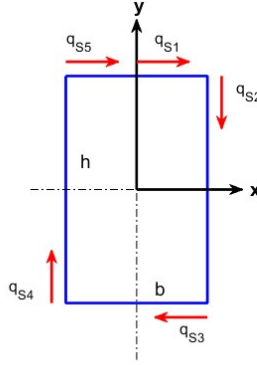


Figure 5.11: Direction of shear flow along the perimeter of the cross section

Using Equation 5.25, the expression for the resulting shear flow q_s are:

$$q_{s1} = -\frac{S_y}{EI_{xx}} \int_0^{s1} \frac{h}{2a_{11f}} ds1 = -\frac{S_y}{EI_{xx}} \frac{hs1}{2a_{11f}} \quad (5.39)$$

$$q_{s2} = -\frac{S_y}{EI_{xx}} \left[\frac{hb}{4a_{11f}} + \int_0^{s2} \left(\frac{h}{2} - s2 \right) \frac{1}{a_{11w}} ds2 \right] = -\frac{S_y}{EI_{xx}} \left[\frac{hb}{4a_{11f}} + \frac{hs2 - s2^2}{2a_{11w}} \right] \quad (5.40)$$

$$q_{s3} = -\frac{S_y}{EI_{xx}} \left[\frac{hb}{4a_{11f}} + \int_0^{s3} \frac{-h}{2a_{11f}} ds3 \right] = -\frac{S_y}{EI_{xx}} \left[\frac{hb}{4a_{11f}} + \frac{hs3}{2a_{11f}} \right] \quad (5.41)$$

$$q_{s4} = -\frac{S_y}{EI_{xx}} \left[-\frac{hb}{4a_{11f}} + \int_0^{s4} \left(-\frac{h}{2} + s4 \right) \frac{1}{a_{11w}} ds4 \right] = -\frac{S_y}{EI_{xx}} \left[\frac{hb}{4a_{11f}} + \frac{hs4 - s4^2}{2a_{11w}} \right] \quad (5.42)$$

$$q_{s5} = -\frac{S_y}{EI_{xx}} \left[-\frac{hb}{4a_{11f}} + \int_0^{s1} \frac{h}{2a_{11f}} ds5 \right] = -\frac{S_y}{EI_{xx}} \left[-\frac{hb}{4a_{11f}} + \frac{hs5}{2a_{11f}} \right]. \quad (5.43)$$

$$q_{s0} = 0. \quad (5.44)$$

Since value of the constant shear flow at the cut $q_{s,0}$ is zero,

$$q_b = q_s + q_{s,0} = q_s \quad (5.45)$$

and the maximum shear flows due to bending in the flanges:

$$q_{s_f} = \frac{S_y}{EI_{xx}} \frac{hb}{4a_{11f}} \quad (5.46)$$

and walls:

$$q_{s_w} = \frac{S_y}{EI_{xx}} \left[\frac{hb}{4a_{11f}} + \frac{h^2}{8a_{11w}} \right] \quad (5.47)$$

are shown in figure 5.12.

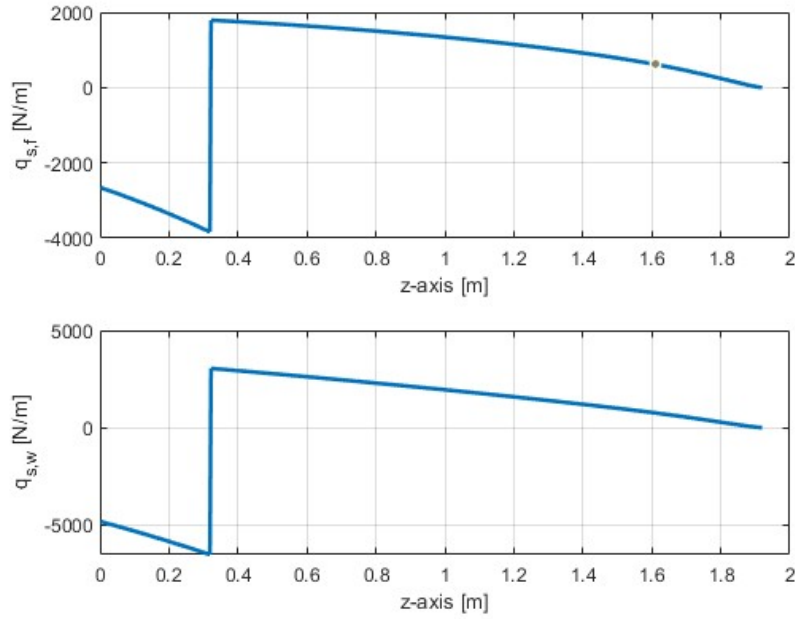


Figure 5.12: Maximum bending shear flow in walls and flanges

The bending shear flow pattern along the perimeter of the cross section is shown in figure 5.13.

The distribution of the constant torsional shear flow, calculated using Equation 5.27, is displayed in figure 5.14. Given that the shear flow resulting from torsion can either have the same or opposite sign to the shear flow produced by bending at different points along the cross-section, it is not sufficient to simply add the two flow values algebraically to determine the maximum shear flow at each node. To ensure accurate results, the chosen approach was to sum q_s to the absolute value of q_t multiplied by the sign of q_s . This method guarantees that in every point along the spar, the shear flow in both the walls and flanges reflects the maximum possible values.

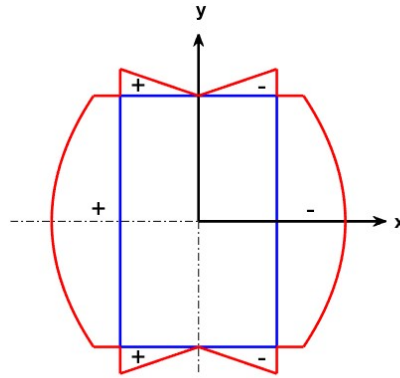


Figure 5.13: Bending shear flow pattern along the perimeter of the cross section

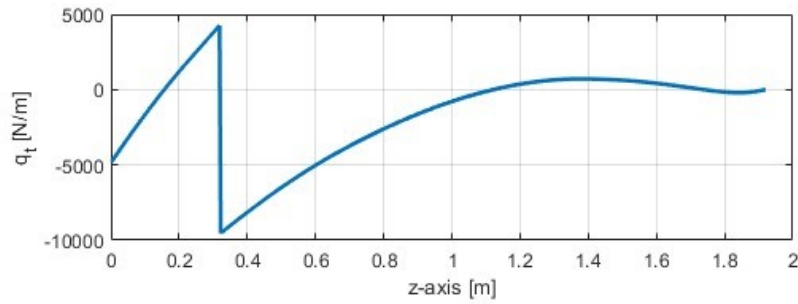


Figure 5.14: Torsional shear flow distribution

The stresses in each ply of the laminates are then obtained by applying equations 5.28 and 5.30 and the results of the maximum normal and shear stresses for the UD , PW_0 and PW_{45} layers (where the subscript indicates the lamination angle with respect to the reference z -axis) in the flanges and walls are shown in figures 5.15–5.18. Table 5.3 shows the comparison between the values of the maximum resulting stresses for the UD and PW layers with their respective strengths.

	σ_{max} [MPa]	F_{1c} [MPa]	τ_{max} [MPa]	F_{12}
UD layer	173.1	1400	4.1	159
PW layer	73.4	750	2.9	155

Table 5.3: Comparison between maximum stresses and material strengths

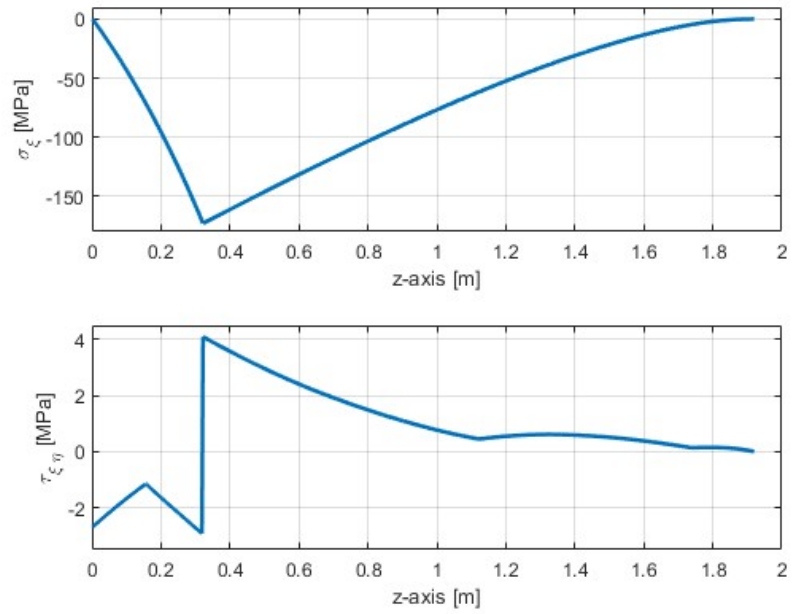


Figure 5.15: Normal and shear stresses distribution in the UD flange layer

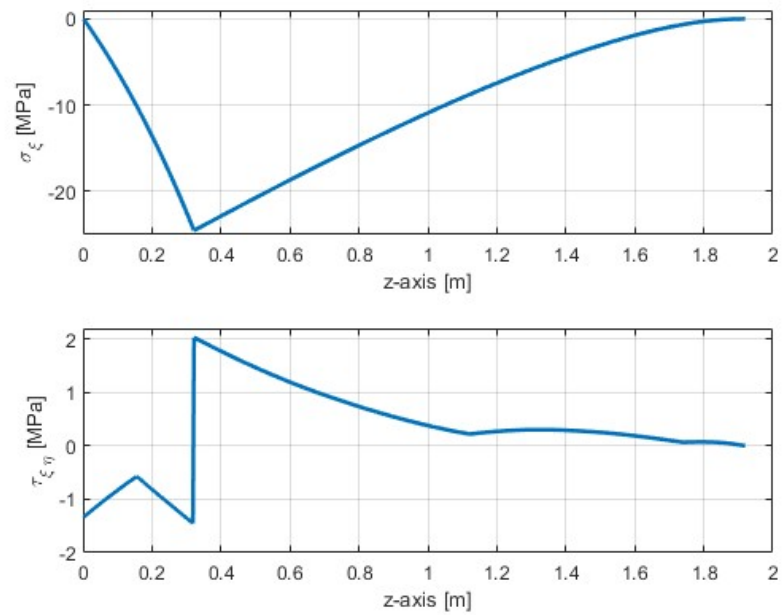


Figure 5.16: Normal and shear stresses distribution in the PW_{45} flange layer

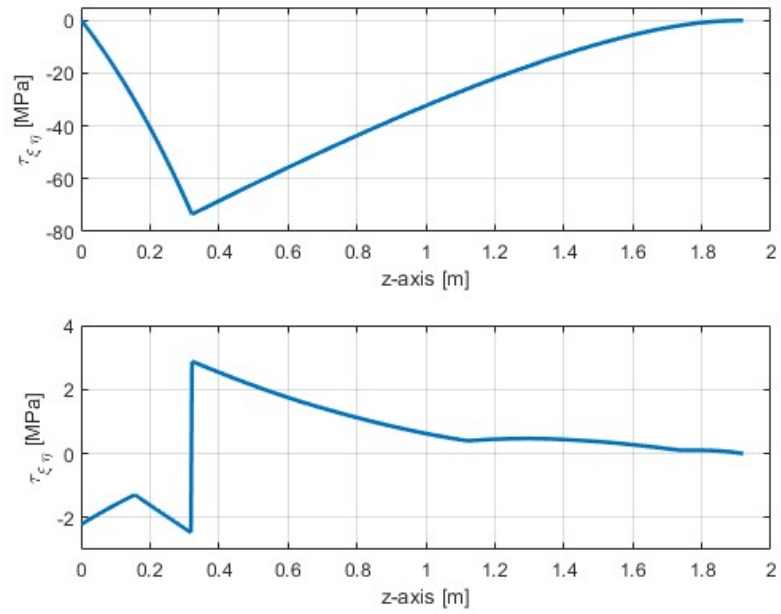


Figure 5.17: Normal and shear stresses distribution in the PW_0 walls layer

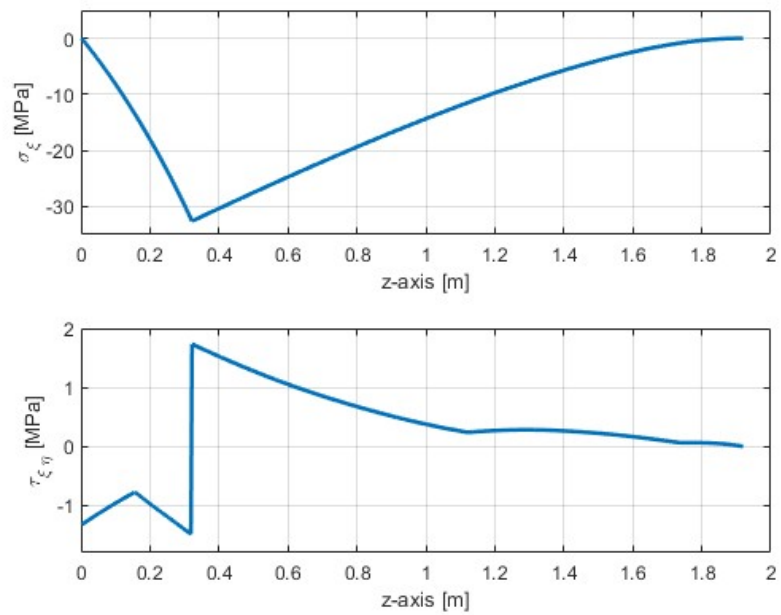


Figure 5.18: Normal and shear stresses distribution in the PW_{45} walls layer

From the results obtained it is evident that the maximum stress values are well below the strength limits imposed by the materials, however, in order to state that the beam is able to resist the applied loads it is crucial to ensure that no instability phenomena, such as buckling or local buckling occur. The first phenomenon, global buckling, refers to an instability of the beam when subjected to an axial compressive load. Since the wing spar is only subjected to shear loads, this type of buckling will not be considered in the current analysis. Local buckling on the other hand is due to the onset of compressive stresses on specific wall segments of the cross-section generated by the bending moments and can therefore occur even in the absence of axial compressive loads, leading to local instability and thus reducing the flexural stiffness of the entire beam. In the case of a rectangular beam subjected to bending, the upper flange is the part of the structure most susceptible to local buckling, since it is primarily subjected to compressive stresses as demonstrated by the results obtained. The calculation of the local critical buckling stress is typically performed by modelling the flange as a panel simply supported along its longer edges and subjected to a compressive load along the shorter side. The comparison between the maximum compressive stresses to which the panel is subjected and the critical buckling stress therefore allows us to verify the possibility that instability phenomena may arise inside the beam.

As reported by Qiao and Shan [15], the local buckling stress resultant (force per unit length) for an orthotropic plate simply supported along all four edges can be simplified as:

$$N_{CR}^{SS} = \frac{2\pi^2}{b^2} \left[\sqrt{D_{11}D_{22}} + (D_{11} + 2D_{66}) \right], \quad (5.48)$$

where b is the length of the loaded side and D_{ij} are the laminate bending stiffness coefficients. For the problem at hand, the boundary conditions are slightly different because the upper flange results simply supported only along its longer edges. Nevertheless, in thin-walled panels with a large length-to-width ratio, the contribution of the shorter, unsupported edges becomes negligible, and the buckling behavior is dominated by the longer, simply supported edges. Consequently, the previously mentioned formula provides a good approximation of the local buckling stress. From Equation 5.48, a critical buckling load value of $7,67 \times 10^5$ N/m is obtained for the flanges. This value must be compared with the maximum load per unit length acting on the upper flange, given by:

$$N_{max} = n_{UD} \cdot t_{UD} \cdot \sigma_{max,UD} + n_{PW} \cdot t_{PW} \cdot \sigma_{max,PW} \quad (5.49)$$

where, n represents the number of layers, t is the thickness of each layer, and σ_{max} denotes the maximum compressive stress for the unidirectional (UD) and plain weave (PW) plies, resulting in a calculated value of

$$N_{max} = 1,03 \times 10^5 \text{ N/m.}$$

The analyses conducted demonstrate that the maximum compressive and shear stresses remain well within the material's strength limits, and the critical buckling load far exceeds the maximum applied stress. Consequently, the spar is adequately designed to withstand the aerodynamic loads applied to the wing under the most severe flight conditions, ensuring both structural strength and local stability. Despite the results indicating that further weight reduction could be achieved by decreasing the number of layers in the laminates of the flanges and walls, as discussed in section 4, it was decided to maintain a minimum laminate thickness of 1 mm.

5.4 Truss Structure Analysis

Given the geometric complexity of the truss structures, the stress analysis was performed using ANSYS software, which enabled the direct import of the three-dimensional geometry from the CAD modeling software. For a valid finite element analysis, it is essential to first define the type of element on which the analysis will be based. The most commonly used elements in FEA are:

- Beam elements, suitable for analyzing slender beam structures, based on Timoshenko beam theory, including shear-deformation effects.
- Shell elements, ideal for thin shell structures and for modeling composite layered shells or sandwich constructions, based on the Mindlin-Reissner shell theory.
- Solid elements, used for analyzing fully three-dimensional structures, which can take the form of prisms, tetrahedral, or pyramids depending on the geometric regularity of the structure.

The choice of element type is crucial because, although solid elements can yield more accurate results compared to shell or beam elements, they come with a significantly higher computational cost due to the larger number of nodes associated with these elements. This principle also applies to the order of the shape functions used to define the displacement field inside the element. Unlike first-order elements, where the nodes are located at the corners, higher-order elements, by adding additional nodes positioned at the midpoint of each side, allows for more accurate interpolation of displacements, strains, and stresses compared to linear elements. Another significant advantage of higher-order elements lies in their ability to reduce the sensitivity of the results to the mesh size, allowing for accurate results even with a coarser mesh. However, this increases the system's degrees of freedom and, consequently, the computational time required to solve the problem. For this reason, higher-order elements are well-suited for curved geometries, where they

provide a more accurate approximation without requiring a highly refined mesh, and for nonlinear materials to accurately capture the complex physical behavior. Additionally, they are beneficial in cases where the geometry contains holes or other discontinuities that cause high stress concentrations. Conversely, for simple geometries with uniformly distributed loads or large models, the advantages of using higher-order elements may not justify the increased computational cost. Given that the truss structures feature curved surfaces and areas with sharp transitions, the use of simpler beam or shell elements, may lead to inaccurate results. Additionally, since stress concentrations are expected at the load application points, particularly around the circular reinforcements, it becomes crucial to accurately model these regions and simpler element types may not provide the required accuracy in these areas of interest. As a consequence, the decision was made to use 3-D Solid 187 elements. Given the geometry, after selecting the appropriate element type and defining the material mechanical properties, it is necessary to define the mesh applied to the model. Initially, a coarse mesh was applied, which was then gradually refined until convergence in the results was achieved. Finally, boundary conditions and applied loads were set. Since the structure is bonded to the spar, all nodes belonging to the inner faces of the rectangular reinforcement were constrained in translation in the two directions that lie in the plane of the respective face. The applied loads are determined by modeling each truss structure as a beam simply supported at the shear centers of the two cylindrical reinforcements, while the reaction forces from the wing spar are applied as concentrated loads in correspondence with the shear center of the rectangular reinforcement as shown in figure 5.19, where points A and C correspond to the shear center of the front and rear cylindrical beams respectively and point B corresponds to the spar shear center.

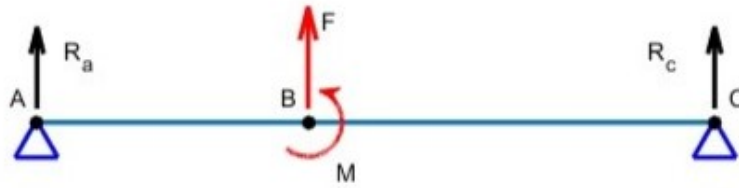


Figure 5.19: Truss structures beam model

By enforcing both force and moment equilibrium around point B:

$$\begin{cases} R_a + R_c + F = 0 \\ M - R_a \cdot d_a + R_c \cdot d_c = 0 \end{cases} \quad (5.50)$$

where d_a and d_c are the distances between points A and C from point B, the

reaction forces acting on the truss structure can be determined and results are reported in table 5.4.

Truss structure	d_a [m]	d_c [m]	F [N]	M [Nm]	R_a [N]	R_C [N]
Outer	0,24	0,22	992	-33,3	-546,8	-445,2
Inner	0,13	0,33	-574	-13,6	382,2	191,8

Table 5.4: Loads applied to truss structures

Since, in this case, the cylindrical beams are not bonded to the reinforcements, allowing for the UAV to be disassembled, the loads are not distributed along the inner faces of the circular reinforcements but are concentrated at the contact points between the cylindrical beams and reinforcements. To ensure accurate load application, the concentrated loads were not applied to a single node but distributed across multiple nodes along the thickness of the structure, thus reducing stress concentration and improving the accuracy of the analysis as depicted in figures 5.20 and 5.21.

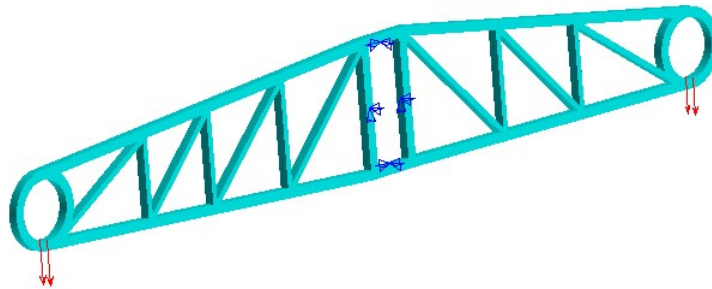


Figure 5.20: Outer truss structure loads and boundary conditions

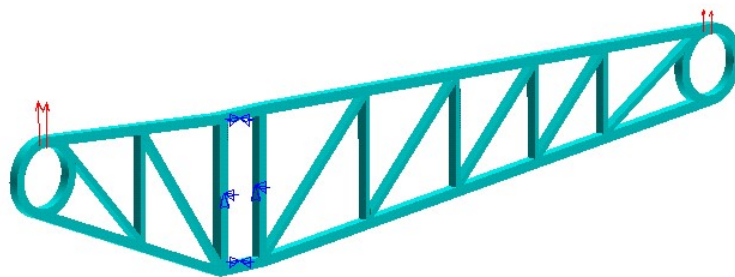


Figure 5.21: Inner truss structure loads and boundary conditions

To verify the ability of the two structures to withstand the applied loads, it was decided to make use of the Von Mises yield criterion [16], according to which, an isotropic and ductile material will not fail as long as the energy associated with the distortion of the material does not reach the critical value that causes yield. The application of this criterion requires the introduction of the equivalent Von Mises stress, obtained by combining the principal stresses according to the equation:

$$\sigma_v = \sqrt{\frac{(\sigma_1 - \sigma_2)^2 + (\sigma_2 - \sigma_3)^2 + (\sigma_3 - \sigma_1)^2}{2}}. \quad (5.51)$$

Following Von Mises' failure criterion, the yield condition is reached if the equivalent stress exceeds the value of the yield stress of the material, obtained through experimental tensile tests, leading the material to reach the plastic field, with consequent permanent deformation of the component. The static structural analysis carried out using the ANSYS software allows to determine, in addition to the principal stresses, the value of the equivalent Von Mises stress at each point of the structure, as shown in figures 5.23 and 5.22.

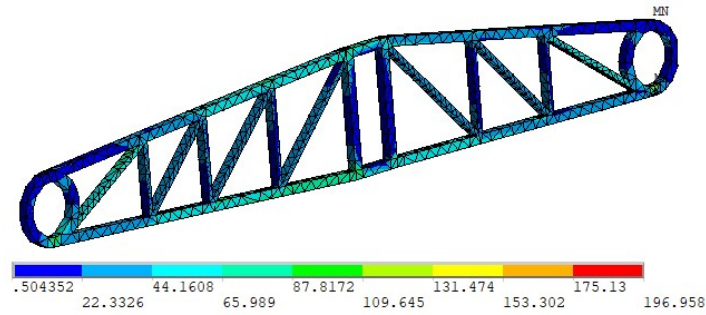


Figure 5.22: Von Mises stress in the outer truss structure [MPa]

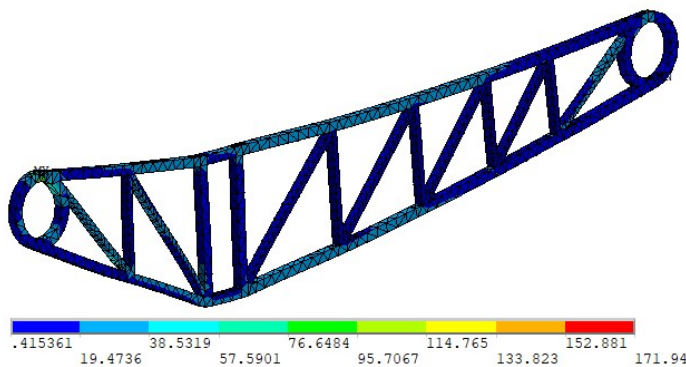


Figure 5.23: Von Mises stress in the inner truss structure [MPa]

Comparing the results obtained with the yield strength value of aluminum detailed in table 4.3, it can be deduced that at no point of the structure does the material reach the yield condition and that the minimum safety factor obtained

$$S.F._{yield} = \frac{\sigma_y}{\sigma_{v,max}} = \frac{503 \text{ MPa}}{197 \text{ MPa}} = 2.55 \quad (5.52)$$

exceeds the minimum value of 1.5 imposed by Certification Specifications.

Having verified that the stresses in the structure are not such as to reach the yield strength of the material, however, does not imply that the structure is adequately sized to transmit the aerodynamic loads from the wing spars to the cylindrical beams. It is also essential to verify that the truss elements subject to axial compressive stress do not buckle, consequently causing an increase in stress in the elements not subject to instability. These instability phenomena are therefore critical as they would induce a reduction in the stiffness of the components, until the collapse of the structure is achieved. This verification was carried out through the analysis of the buckling eigenvalues, which allows to determine the minimum multiplication factor to be applied to the load to reach the buckling condition. The results show that the minimum buckling eigenvalue for the outer truss structure is equal to $\lambda_1 = 1.5$, while for the inner truss structure, the minimum buckling load factor is $\lambda_2 = 2.4$.

Consequently, since the applied loads do not induce either material yield failure or instability phenomena, we can conclude that both truss structures are correctly sized.

5.5 Rib Analysis

The wing ribs are essential for transferring aerodynamic loads from the skin and control surfaces to the spar. As ribs are essential for maintaining the aerodynamic profile of the skin along the wing, the failure of a rib could drastically alter the wing's overall aerodynamic characteristics. The structural integrity of the ribs is thus crucial to the wing's performance and stability. As previously mentioned, this components are designed as sandwich structures composed of two faces made from carbon fiber composites, each made up by two layers of plain weave carbon fiber-epoxy prepreg to enhance shear strength, separated by a polymeric core. This design not only increases the out-of-plane flexural stiffness of the ribs but also significantly enhances the contact area between the skin and the ribs and between the ribs and the spar, thus allowing for an effective bonding and ensuring a more efficient transfer of loads. To determine the aerodynamic load applied, it is assumed that each rib receives loads from the two adjacent halves of the skin panels. Rather than conducting a structural analysis on each rib individually, it's been decided

to focus on analyzing the stresses and deformations on the most critical rib. In this case, the second rib from the wing root was identified as the critical one, being the total load a function of the integral of the pressure coefficient over the surface area, and since the chord length of the aerodynamic profile is greater at the root than at the tip, meaning that the resulting load on the ribs closer to the root is significantly higher. The rib located directly at the root was excluded from analysis as it only bears the load from a single half skin panel.

Moreover, the second rib features, in addition to the lightening holes, two additional openings to allow the cylindrical beams to pass through, which reduce the stiffness of the component and could lead to stress concentrations around their perimeters, potentially causing structural failure in those areas.

The experimental aerodynamic data provide the pressure coefficient (cp) distribution over 20 non-uniformly distributed nodes along the chord for 240 airfoil profiles along the spanwise. The rib under examination is positioned at $y_0 = -0.4$ m with respect to the UAV's reference system, between the root rib located at $y_0 = -0.2$ m and the third rib at $y_0 = -0.6$ m. Since each rib bears the aerodynamic load from the halves of the neighboring skin panels, the pressure coefficient distribution must be considered for skin panels spanning between $y_0 = -0.3$ m and $y_0 = -0.5$ m, corresponding to the airfoil profiles numbered between 150 and 167. The values of the pressure coefficients can be arranged in a matrix $CP(i, j)$ where the index $i(1 : 20)$ refers to the position of the corresponding node along the chord, while $j(150 : 167)$ represents the corresponding profile. To simplify the calculation, it is assumed that the pressure coefficient remains constant between two adjacent profiles and that the chord length is constant between airfoils. The load per unit length along the rib can then be approximated by integrating the pressure coefficient along the specified span, as follows:

$$dL(i) = \frac{1}{2} \rho v^2 \int cp(i) dy \text{ N/m} \quad (5.53)$$

where the integral is calculated through the matlab trapz function:

$$\int cp(i) dy = \text{trapz}(\mathbf{y}, CP(i, :)) \quad (5.54)$$

and \mathbf{y} is the vector containing the airfoils coordinated along the y_0 -axis. This method provides an estimate of the aerodynamic load distributed across the 20 nodes along the critical rib. Finally, since the structural analysis was conducted using ANSYS, a piecewise constant function was chosen to interpolate the aerodynamic load through a uniform distribution of 10 elements along the profile so as to simplify the application of loads to the model within the software environment while still providing a sufficiently accurate representation of the load distribution. The comparison between the load distribution obtained through equation 5.54 and the distribution obtained through numerical interpolation is shown in figure 5.24.

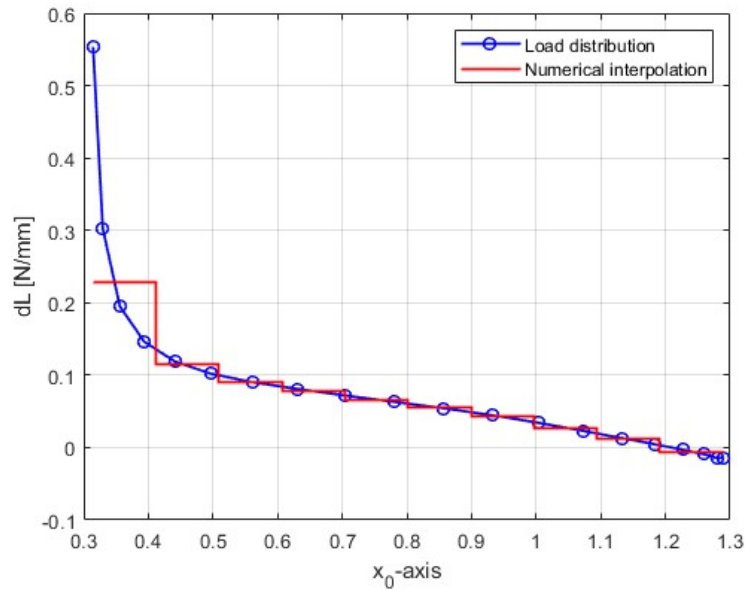


Figure 5.24: Load distribution applied to the rib

The load distribution is expressed in N/mm rather than N/m since ANSYS imports geometry in millimeters and it is therefore necessary to scale the applied loads to match the model's geometric units. After defining the loads applied to the rib, a static structural analysis was performed on the component. Given that the rib has a sufficiently thin thickness, shell 181 elements were chosen for the analysis. These elements are particularly suitable for analyzing thin to moderately-thick shell structures and are compatible with layered applications, making them well-suited for modeling sandwich panels. The accuracy of these elements in modeling composite shells is based on the first-order shear-deformation theory, commonly known as Mindlin-Reissner shell theory [4]. Since the aerodynamic load was approximated using a piecewise constant function across an evenly spaced 11-nodes distribution along the airfoil, the rib's upper edge was divided into 10 segments before meshing. After mesh generation, loads and boundary conditions were applied to the model. The loads were assigned by applying a constant line pressure to each segment along the upper edge.

As for the boundary conditions, the same approach used for the truss structures was followed. All nodes along the opening for the spar insertion were constrained in translation along the two directions lying within the plane of the corresponding contact surfaces between the spar and the rib. The loads and boundary conditions applied to the model are shown in figure 5.25.

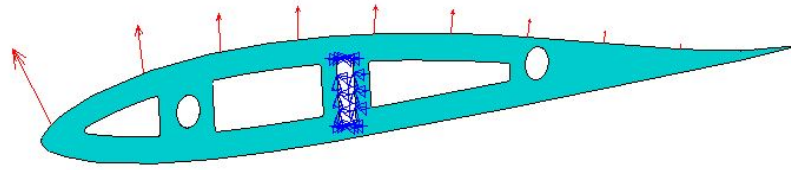


Figure 5.25: Rib loads and boundary conditions

The Ansys software allows to plot the results obtained for each layer of the laminate and therefore the reported results, in addition to the overall deformation of the rib show the trend of the stresses in the faces and in the core. In this way it is possible to verify that the aerodynamic loads applied to the rib do not induce stresses exceeding the limits of the material both for the plain wave carbon fiber ply and for the PVC foam.

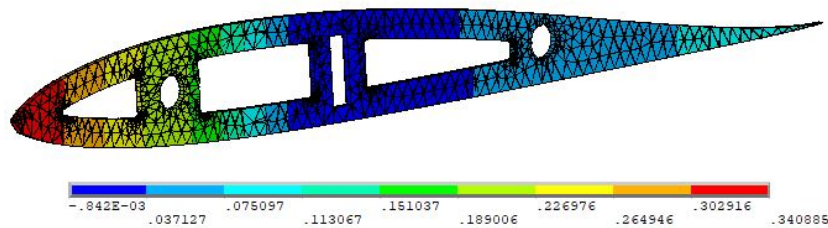


Figure 5.26: Rib deflections [mm]

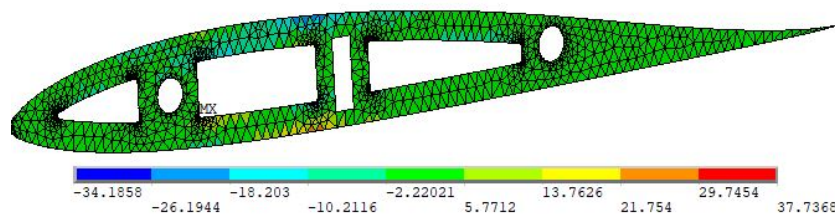


Figure 5.27: Normal stresses in the rib faces [MPa]

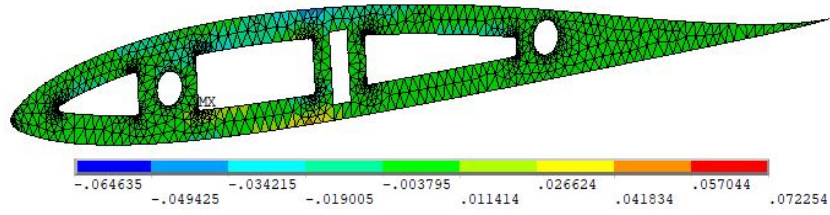


Figure 5.28: Normal stresses in the rib core [MPa]

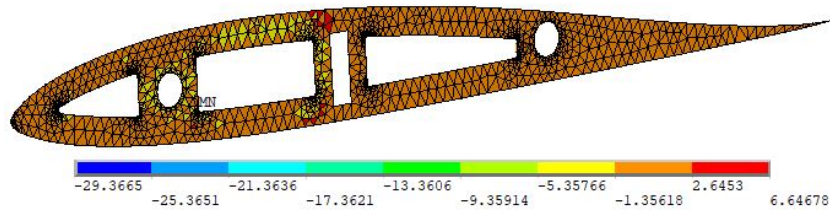


Figure 5.29: Shear stresses in the rib faces [MPa]

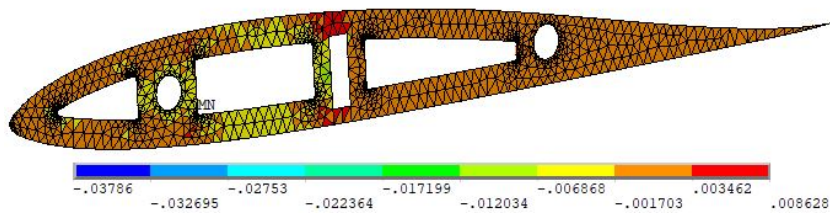


Figure 5.30: Shear stresses in the rib core [MPa]

As expected, the maximum stresses are obtained near the edges of the lightening holes, but the comparison between the results obtained and the strength characteristics of the materials reported in table 5.5, shows how the maximum normal and shear stresses are significantly lower than the limits imposed by the materials.

	PW carbon fiber	Divinycell H80
Maximum tensile stress [MPa]	37.74	0.07
Tensile strength [MPa]	722	2.2
Maximum compressive stress [MPa]	34.19	0.06
Compressive strength [MPa]	742	1.15
Maximum shear stress [MPa]	29.37	0.04
In-Plane shear strength [MPa]	155	0.95

Table 5.5: Comparison between maximum stresses and materials strengths for the wing ribs

This suggests the potential to reduce the number of layers for each face to a single layer, thereby achieving a weight reduction in the ribs. However, since out-of-plane loads may occur during the UAV wing assembly, such a reduction could lead to excessive panel flexibility or even failure. Consequently, a minimum thickness of 0.5 mm has been maintained for each face of the sandwich panels used in the ribs to ensure structural integrity.

5.6 Wing Components' Weight

The detailed breakdown of the weight and the position of the center of mass in the symmetry plane of all components that make up the wing structure is presented in table 5.6.

Item	Mass [g]	x_{cm} [mm]	z_{cm} [mm]
Main Wing			
Spars	624	906	42
Ribs	940	809	3
False Spar	100	1121	-14
Truss Structure (outer)	230	725	-4
Truss Structure (inner)	240	718	-22
Control Surfaces			
Ribs	30	1217	26
Spars	64	1218	43
Flanged Bushings	30	1202	46
Rods	170	1199	48
Total	2428	877	16

Table 5.6: Weight of the wing components

The data in the table highlight that the wing is exceptionally lightweight,

reflecting the efficiency of the chosen materials and design solutions. This is primarily attributed to the use of a polymeric film for the skin, which significantly reduces its weight compared to solutions where the skin also serves structural functions. Additionally, this approach allows for the possibility of increasing the number of ribs within the wing if future analyses reveal excessive alterations in aerodynamic characteristics caused by skin deformation.

Chapter 6

Structural Analysis of Fuselage Components

In this chapter, the analysis of the stresses acting on the main load carrying components of the fuselage is discussed. The analysis was performed by analyzing separately the main fuselage structure and the two cylindrical beams which are responsible for transferring the loads from the wings to the main structure.

6.1 Cylindrical Beams Analysis

The structural analysis of the cylindrical beams, given the possibility of easily modifying their geometric characteristics, the constraint conditions and the loads applied in the design phase, was carried out using the Matlab software, following the same procedure illustrated for the structural analysis of the wing spar.

The sizing of the cylinders requires identifying which one is more critical, i.e., which of the two experiences higher loads. Since the geometric characteristics of the cross-section are constrained by design limits, as outlined in section 2.3, the appropriate layup sequence and number of layers must be determined to ensure the most critical cylinder can withstand the applied stresses. The identification of the most stressed cylindrical beam was carried out by considering that both beams are subject to the same boundary conditions, being simply supported at the primary load-bearing fuselage ribs. Consequently, the most critical beam is the one experiencing higher concentrated loads. As demonstrated by the reaction forces applied to the truss structures from table 5.4, the front cylindrical beam is identified as the most critical component and therefore, the sizing of the beams that transfer loads from the wings to the fuselage must be based on the concentrated forces applied to the front beam. The sizing is carried out by performing a structural analysis of the component considering the same stacking sequence used for the

spar flanges, as the highest expected loads are compressive, primarily due to the bending of the cylindrical beam. Consequently, the ABD matrix of the laminate is as shown in equation 4.11. From equations 5.3 and 5.5, given that the radius of the section is $r = 15$ mm, the expressions for the bending and torsional stiffness characteristics of the beam are:

$$\widehat{EI}(z) = \frac{\pi r^3}{a_f(1,1)} + \frac{r}{d_f(1,1)} = 902.5 \text{ Nm}^2 \quad (6.1)$$

$$\widehat{GJ}(z) = 2 \frac{\pi^2 r^3}{a_f(6,6)} = 962,9 \text{ Nm}^2. \quad (6.2)$$

Following the same procedure as for the analysis of the wing spar, by discretizing the beam into a finite number of elements, constraining the degrees of freedom in translation and rotation at the supports, and applying concentrated loads, the system of equations 5.16 can be solved to obtain the deformation vector. Since no torsional moments act on the beam, the only significant deformation is bending, as shown in figure 6.1.

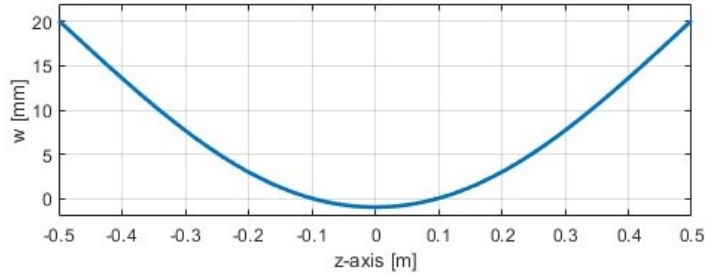


Figure 6.1: Front Cylindrical beam deflection

The reaction forces were determined for both the front and rear beams, as they are essential for the structural analysis of the fuselage and results are presented in table 6.1.

Front Cylindrical beam		Rear Cylindrical beam	
Constrained point	Value	Constrained point	Value
$z = -0.1$ m	-164.4 N	$z = -0.1$ m	-253.4 N
$z = 0.1$ m	-164.4 N	$z = 0.1$ m	-253.4 N

Table 6.1: Reaction forces applied to the cylindrical beams

The shear force and bending moment diagrams obtained from equations 5.19 and 5.20 are as shown in figure 6.2.

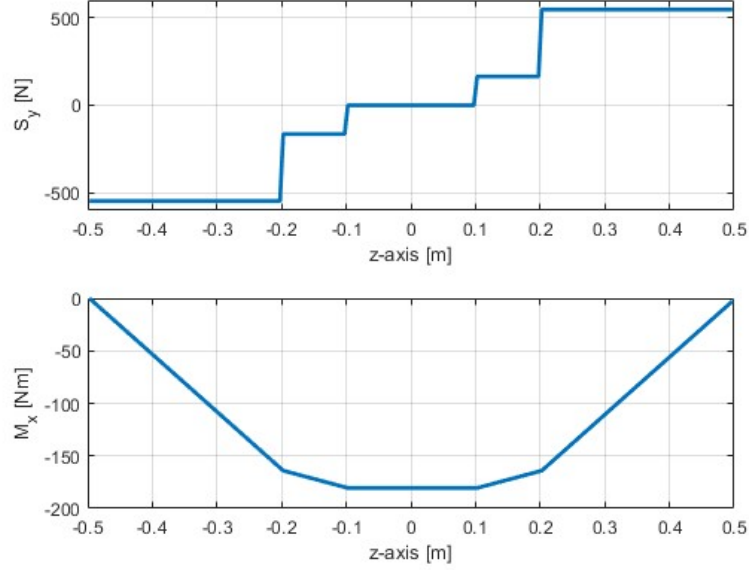


Figure 6.2: Transverse load and bending moment distribution in the cylindrical beam

The shear flow, as done for the rectangular beam, can be determined by summing the flow obtained by considering the section opened at a specific point (equation 5.25) as shown in figure 6.3:

$$q_s = -\frac{S_y}{\widehat{EI}_{xx}} \int_0^{s1} \frac{y}{a_{f(1,1)}} ds1 = -\frac{S_y}{\widehat{EI}_{xx}} \int_0^\theta \frac{r^2 \sin(\theta)}{a_{f(1,1)}} d\theta = \frac{S_y r^2}{\widehat{EI}_{xx} a_{f(1,1)}} (\cos(\theta) - 1). \quad (6.3)$$

and the flow at the point where the section was cut (equation 5.26):

$$q_{s0} = -\frac{\oint q_s ds}{\oint ds} = -\frac{S_y r^3 \int_0^{2\pi} (\cos(\theta) - 1) d\theta}{\widehat{EI}_{xx} a_{f(1,1)} 2\pi r} = \frac{S_y}{\widehat{EI}_{xx}} \frac{r^2}{a_{f(1,1)}}. \quad (6.4)$$

The overall shear flow distribution as a function of the angle θ is given by:

$$q_b = \frac{S_y r^2}{\widehat{EI}_{xx} \cdot a_{11f}} \cos(\theta). \quad (6.5)$$

It follows that at $\theta = 0$, where the axial loads are zero, the shear flow is highest, whereas at $\theta = \pi/2$, where the axial loads and bending moments are at their peak, the shear flow is zero.

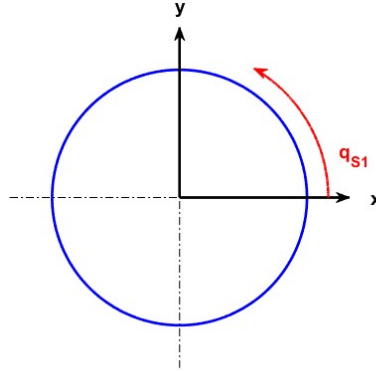


Figure 6.3: Direction of shear flow along the perimeter of the cylindrical beam cross section

The in-plane force vectors for these critical points on the cross-section are given by:

$$\begin{pmatrix} N_{\xi} \\ N_{\xi\eta} \\ M_{\xi} \end{pmatrix}_{\theta=0} = \begin{pmatrix} \frac{M_z^{max}}{EI_{yy}} \frac{r}{a_{11w}} \\ 0 \\ \frac{M_z^{max}}{EI_{yy}} \frac{1}{d_{11w}} \end{pmatrix}. \quad (6.6)$$

$$\begin{pmatrix} N_{\xi} \\ N_{\xi\eta} \\ M_{\xi} \end{pmatrix}_{\theta=\pi/2} = \begin{pmatrix} 0 \\ \frac{S_y r^2}{EI_{xx} \cdot a_{11f}} \\ 0 \end{pmatrix}. \quad (6.7)$$

The distribution of the maximum stresses in the UD and PW plies has been obtained through equations 4.3 and 5.30 and results are reported in figures 6.4 and 6.5.

	σ_{max} [MPa]	F_{1c} [MPa]	τ_{max} [MPa]	F_{12} [MPa]
UD layer	394.5	1400	4.2	159
PW layer	55.9	750	20.8	155

Table 6.2: Maximum compressive and shear stress in cylindrical beams

From the results obtained, it is evident that the selected number of plies and the lamination sequence are adequate to ensure the efficient transmission of aerodynamic loads from the wing to the fuselage.

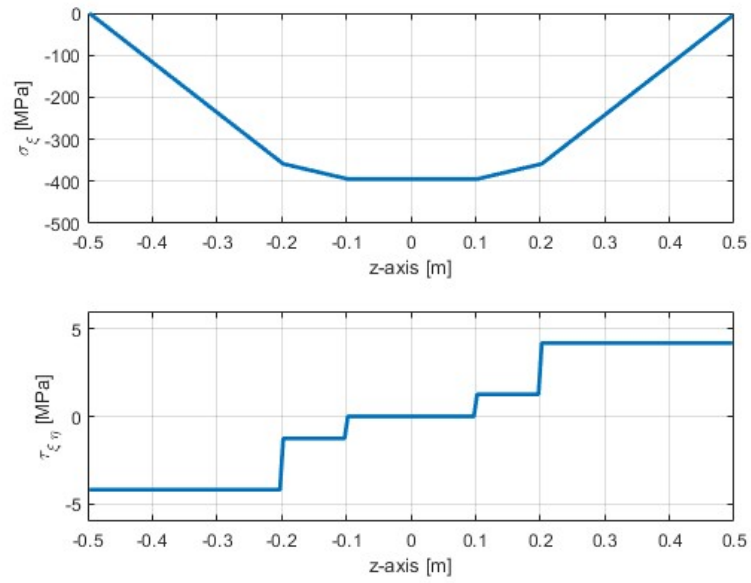


Figure 6.4: Maximum normal and shear stresses distribution in the UD layer

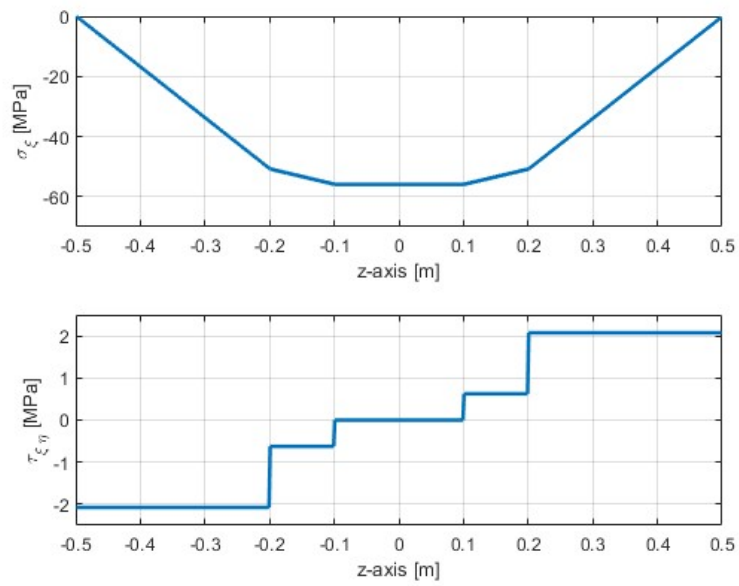


Figure 6.5: Maximum normal and shear stresses distribution in the PW_{45} layer

6.2 Fuselage Main Structure Analysis

Before conducting the structural analysis of the fuselage main structure, it is essential to recognize that an accurate analysis is not feasible at this preliminary design stage. This limitation arises not only from the potential need to modify the structure in later phases, but also due to the absence of critical data required for a comprehensive structural analysis and the assumptions made this far.

First of all, the most critical flight condition has been established based on the initial mass estimation of the aircraft provided by Suewatanakul et al. [2]; however, as noted in Section 6.3, the structural weight is actually lower than the estimated value. Consequently, the characteristic speed for the flight condition in which the maximum load factor is reached is overestimated, leading to an inflated calculation of lift.

Secondly, as outlined in section 5, the wing analysis was conducted disregarding the weight of elements. This approach was intended to capture the most critical loading condition, allowing for adjustments to the structural components in subsequent design stages.

Finally, aside from the hydrogen storage tank, fuel cells, hybrid battery, and extra battery, only preliminary weight estimates have been made for other components, and their placement within the UAV has not yet been determined. As a result, it is not possible to accurately apply the weight-induced loads of these systems in the FEM model. This leads to an imbalance in the fuselage under the applied loads.

In this context, the structural analysis of the fuselage serves as a preliminary assessment rather than a precise evaluation of performance under operational conditions. Given the current design phase, this analysis primarily provides a conceptual understanding of the load-bearing behavior and overall stress distribution within the fuselage structure. Without definitive data on component placement and weights, as well as adjustments in structural mass and critical flight speeds, the analysis cannot reflect the final loading conditions. Instead, it highlights potential areas for structural refinement, offering insights into how the fuselage might respond to estimated loads. This preliminary analysis thus lays the groundwork for further optimization, identifying regions that may require reinforcement or modification as more accurate data becomes available in subsequent design stages.

Due to the geometric complexity inherent in the three-dimensional structure, the analysis of the main fuselage was conducted using Ansys software. As outlined in section 2.2, the fuselage of the Green Raven is composed of longitudinal and transverse sandwich panels interlocked through half-cut joints and is designed to bear multiple types of loads: aerodynamic lift forces transferred from the skin, concentrated loads from the weight of onboard systems, self-weight of the structure and concentrated loads transferred from the cylindrical beams extending from the wings.

The concentrated loads transmitted by the cylindrical beams to the primary load bearing panels have already been obtained, since they are equal in modulus and opposite in direction to the reaction forces applied to the cylindrical beams. These loads, thanks to the presence of the flanged bushings that connect the cylinders to the primary load-bearing panels, are not concentrated in specific points, but distributed in the neighboring areas of the perimeters of the corresponding holes. Consequently, a correct application to the model of the loads coming from the wings requires defining 4 master nodes, on which the concentrated forces are applied, each linked to corresponding slave nodes belonging to the contact surface between the bushing and the panel, enabling an effective distribution of these forces. This approach allows for a more realistic load distribution simulation and reduces stress concentrations that would occur if the loads were applied to specific points. Similarly, the load due to the weight of the hydrogen tank, the fuel cells and the extra batteries, taking into account the load factor $n = 4$, was distributed on the nodes belonging to the edges of the system support panels. Finally, the lift distribution per unit length transmitted from the skin to the fuselage's longitudinal panels has been determined and applied to the model, similarly to the approach outlined in section 5.5.

In the present analysis, as previously mentioned, the approximations made and the lack of information regarding system placements result in an unbalanced fuselage. Consequently, the structural analysis was performed by using static stress analysis with the inertia relief [17], a technique used to simulate an equilibrium condition in structures that are not rigidly constrained. Inertia relief allows for the simulation of equilibrium by introducing inertial forces that counterbalance the applied external loads, thereby enabling an approximation of the structural response avoiding unrealistic stress concentrations that might result from artificial boundary conditions. To simplify the analysis and avoid plotting stresses in all possible directions within the fuselage, a strategic approach was taken: rather than visualizing each stress component individually, the material strengths were defined, and the maximum stress failure criterion was chosen for evaluation. Using the maximum stress failure criterion allows us to assess whether stresses in any direction exceed the material's strength limits, thereby simplifying the analysis and avoiding the need for detailed individual stress plots, which would otherwise be cumbersome and less informative. The results obtained for the two ply and for the core of the sandwich panels are shown in figures 6.6, 6.7 and 6.8. As evident, the most highly stressed areas are located in the primary load-bearing panels. However, since the ratio between the maximum stresses and the material strengths does not exceed 0.013, the structure is not only sufficiently dimensioned but also allows for potential weight-reducing cutouts and openings for system cabling, as well as the application of additional concentrated loads from the inertia of remaining systems in future design phases. Nevertheless, as previously discussed, it is not feasible to

implement weight-reducing cutouts at this stage of design, as the exact positions of systems and their supports within the fuselage are not yet defined and this uncertainty could lead to conflicts with the placement of other systems in later stages.

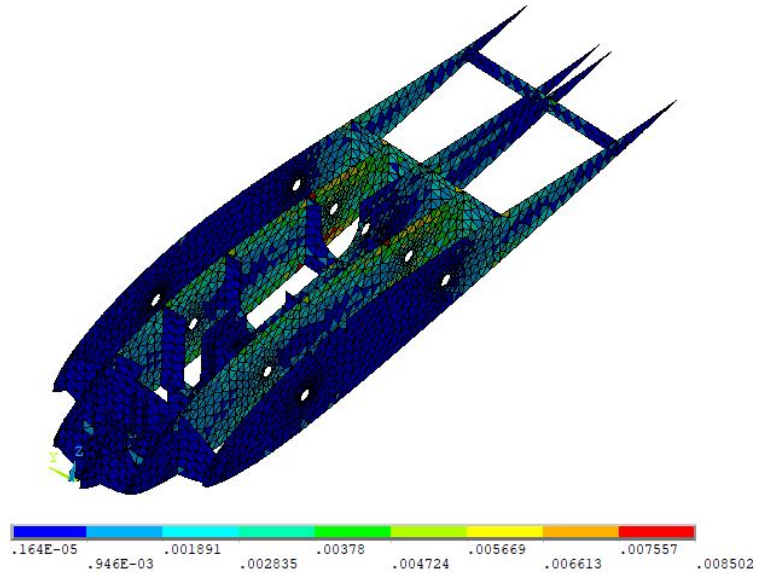


Figure 6.6: Maximum stress criterion in the PW_{45} ply

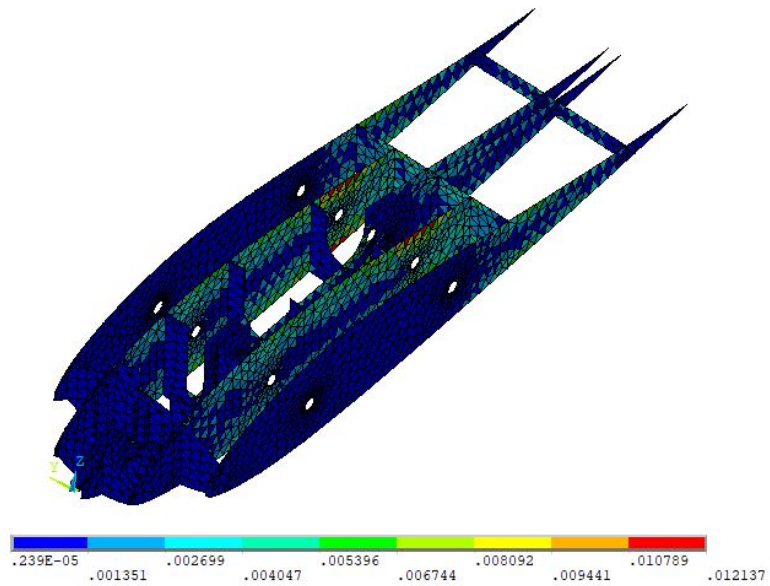


Figure 6.7: Maximum stress criterion in the PW_0 ply

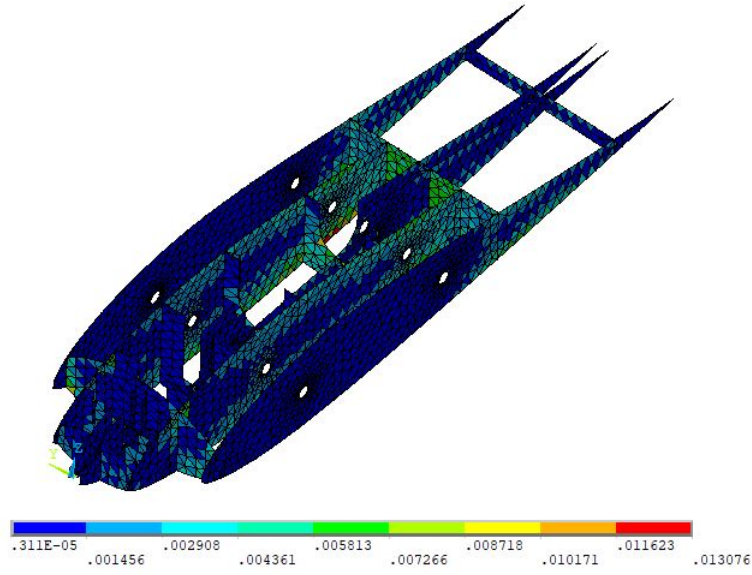


Figure 6.8: Maximum stress criterion in the core

6.3 Fuselage Components' Weight

The weight and the position of the center of mass in the symmetry plane of the fuselage components are listed in table 6.3.

Item	Mass [g]	x_{cm} [mm]	z_{cm} [mm]
Fuselage			
Main Structure	2050	676	-14
Cylindrical Beams	307	896	-18
Flanged Bushings	85	725	-10
Control Surfaces			
Ribs	18	1571	-75
Spars	15	1555	-71
Flanged Bushings	7	1528	-72
Rods	21	1528	-72
Total	2503	717	-16

Table 6.3: Weight of the fuselage components

By combining the weight of the fuselage with that of the two wings, as detailed in table 5.6, and the polymeric skin, which weighs approximately 0.96 kg, the total structural weight amounts to 5.9 kg, and the overall center of mass is located at $x=793$ mm, $z=0$ mm. This result highlights that the design decisions have

successfully produced a structure capable of handling the loads imposed under the aircraft's most demanding flight conditions while remaining well below the maximum allowable weight of 15 kg. This reduction in the total structural weight offers significant advantages, as it lowers the speed required for the UAV to generate enough aerodynamic forces to balance its weight. Consequently, this reduces the power demand on the engines, and, in turn, on the fuel cells and batteries.

Chapter 7

Future Works

While the current study has successfully achieved its primary objectives, further developments of the structural design are necessary to ensure the operational functionality of the framework. As reiterated throughout this work, uncertainties regarding the placement of internal systems within the fuselage remain one of the key challenges to detailed design, necessitating further advancements in subsequent design phases.

A critical aspect of future work includes the design of openings in the main fuselage structure to accommodate the passage of electrical systems, as well as the the quick-release mechanism for attaching the wings to the fuselage. The placement of the landing gear and engines is particularly critical, as it requires the development of structures capable of effectively transferring both propulsion loads and impact forces during landing to the main framework.

A key aspect for future development lies in the study of the aeroelastic behavior of the Green Raven UAV, due to the interaction between the wing's structural elasticity and the aerodynamic forces acting upon it [18]. This interaction alters the geometric shape of the structure, modifying the aerodynamic flow itself, initiating a phenomenon of mutual interaction. Exceeding critical speeds can result in static or dynamic instabilities, increased internal stresses, and potential structural failure.

Aeroelastic analysis therefore requires determining the critical speeds causing:

- **Divergence:** Beyond this speed, aerodynamic forces exceed the elastic restoring forces, causing an increase in the angle of attack at the wingtip. This results in amplified aerodynamic loads and a self-reinforcing deformation;
- **Aileron Reversal:** The increase in lift due to aileron deflection is counteracted by the reduction caused by wing twist deformation. When reversal speed is exceeded, the nose-down moment dominates the aileron deflection, leading to an opposite roll moment relative to the command;

- **Flutter:** When the flutter speed is exceeded, unsteady aerodynamic forces induce rapid elastic deformations in the structure, leading to vibrations. If these oscillations remain undamped, the system becomes dynamically unstable, potentially resulting in structural failure.

It is therefore evident that ensuring the critical speeds associated with these phenomena exceed the operational speeds of the aircraft is essential to guarantee proper response to controls and structural integrity.

Chapter 8

Conclusions

The main focus of this thesis was to design the internal structure of the Green Raven to ensure an effective transfer of aerodynamic loads while maintaining simplicity in construction and assembly and adhering to the maximum weight limits imposed on the structure.

The use of a polymer film for the skin, which therefore does not contribute to the structural stiffness of the wing, and internal load-bearing components such as the spar and ribs, made respectively with composite materials and sandwich panels, significantly reduced the overall weight of the structure while maintaining a robust framework capable of effectively handling aerodynamic forces. Additionally, the weight reduction was further enhanced by the lightening holes in the ribs, which allowed the removal of material from areas less subjected to stress.

In designing the internal structure of the control surfaces, a similar design philosophy was applied. By incorporating lightweight materials and designing efficient load transmission systems to the wing and fuselage ribs, the UAV's control surfaces were optimized for both manufacturing and assembly simplicity while simultaneously reducing their weight.

During the design of the fuselage, significant focus was placed on the need to create a structure that could not only support the loads transmitted by the wings and those resulting from the weight of the predefined onboard systems but also be characterized by modularity, thereby simplifying potential future modifications in later stages of the UAV's development. This requirement was met through the adoption of a structure composed of sandwich panels joined using half-lap joints, which also enabled achieving a balance between ensuring consistent structural integrity and minimizing weight.

A significant challenge in the structural design arose from the need to disassemble the aircraft to simplify transportation, which necessitated the development of a system for transferring the loads applied to the wings from the spars to the primary load-bearing panels of the fuselage. For this purpose, two cylindrical beams were

designed to pass through the fuselage and insert into the wings, absorbing the aerodynamic load applied to the spars through truss structures. This solution ensures efficient load transmission without significantly increasing the overall structural weight, without interfering with the systems housed in the fuselage, and while adhering to the geometric constraints imposed by the Green Raven's BWB configuration.

Finally, the structural analysis, conducted using MATLAB and ANSYS software, verified that the stresses experienced by the load-bearing components under the aircraft's most demanding load conditions remain within safe limits. This ensures the structure's integrity and prevents the risk of failure, while complying with the VLA certification standards requiring a safety factor of 1.5.

In summary, the designed structure successfully meets the established design objectives, maintaining a total weight within the specified limits while ensuring structural integrity.

Appendix A

Aerodynamic data

For more details on the aerodynamic data, refer to the full file available on Dropbox:
Dati Completi MainWing.

Appendix B

Matlab Code for FEM Analysis of the Main Spar

spar.m

```
1 %%%%%%%%%%%%%%%%%%%%%%%%%%%%%%%%%%%%%%%%%%%%%%%%%%%%%%%%%%%%%%%%%%%%%%%%%%
2 % Main Program
3 % Beam FE-code for bending about 1-axis and St. Venant torsion
4 %
5 % Use SI units only
6 %%%%%%%%%%%%%%%%%%%%%%%%%%%%%%%%%%%%%%%%%%%%%%%%%%%%%%%%%%%%%%%%%%%%%%%%%%
7
8 % Clean workspace and command window
9 clear all;
10 close all;
11 clc;
12
13 %%%%%%%%%%%%%%%%%%%%%%%%%%%%%%%%%%%%%%%%%%%%%%%%%%%%%%%%%%%%%%%%%%%%%%%%%%
14 % Geometry Definition
15 %%%%%%%%%%%%%%%%%%%%%%%%%%%%%%%%%%%%%%%%%%%%%%%%%%%%%%%%%%%%%%%%%%%%%%%%%%
16 % Beam input data
17 alpha = 20.5 * pi / 180; % Angle between y_0 and z-axis [rad]
18 L = 1.8 / cos(alpha); % Spar length [m]
19 h1 = 0.07; % Root height [m]
20 h2 = 0.01; % Tip height [m]
21 b = 0.02; % Beam width [m]
22 tf = 0.001044; % Flange thickness [m]
23 tw = 0.00109; % Web thickness [m]
24
25 %%%%%%%%%%%%%%%%%%%%%%%%%%%%%%%%%%%%%%%%%%%%%%%%%%%%%%%%%%%%%%%%%%%%%%%%%%
26 % ABD Matrices (Material Properties)
27 %%%%%%%%%%%%%%%%%%%%%%%%%%%%%%%%%%%%%%%%%%%%%%%%%%%%%%%%%%%%%%%%%%%%%%%%%%
28 % Stiffness matrices for different plies
29 Qf = 1e9 * [129 3.19 0;
30            3.19 9.11 0;
31            0 0 5.22]; % UD ply stiffness matrix
32
33 Qw0 = 1e9 * [56.9 5.12 0;
34            5.12 56.9 0;
35            0 0 4.3]; % PW0 ply stiffness matrix
```

Matlab Code for FEM Analysis of the Main Spar

```

36
37 Qw45 = 1e9 * [35.3 26.7 0;
38               26.7 35.3 0;
39               0 0 2.59]; % PW45 ply stiffness matrix
40
41 % Compliance matrices for flanges and webs
42 Af = [0.938884e8 0.135747e8 0.291013e-8;
43        0.135747e8 0.209241e8 -0.291013e-8;
44        0.291013e-8 -0.291013e-8 0.144538e8];
45
46 Df = [9.29460      1.04088      0.209766e-15;
47        1.04088      1.68651      -0.209766e-15;
48        0.209766e-15 -0.209766e-15 1.14401];
49
50 Aw = [0.478702e8 0.196858e8 0.436519e-8;
51        0.196858e8 0.478702e8 -0.436519e-8;
52        0.436519e-8 -0.436519e-8 0.187948e8];
53
54 Dw = [4.29258      2.39603      0.570491e-15;
55        2.39603      4.29258      -0.570491e-15;
56        0.570491e-15 -0.570491e-15 2.31];
57
58 % Calculate inverse compliance matrices
59 af = inv(Af);
60 df = inv(Df);
61 aw = inv(Aw);
62 dw = inv(Dw);
63
64 %%%%%%%%%%%%%%%%%%%%%%%%%%%%%%%%%%%%%%%%%%%%%%%%%%%%%%%%%%%%%%%%%%%%%%%%%%%
65 % Element and Node Data
66 %%%%%%%%%%%%%%%%%%%%%%%%%%%%%%%%%%%%%%%%%%%%%%%%%%%%%%%%%%%%%%%%%%%%%%%%%%%
67 nelem = 600; % Number of elements (MUST BE A MULTIPLE OF 6)
68 le = L / nelem; % Length of each element [m]
69 ndof = 3 * (nelem + 1); % Number of degrees of freedom
70 nnode = nelem + 1; % Number of nodes
71
72 % Node coordinates along the beam
73 node_z = linspace(0, L, nnode)';
74
75 %%%%%%%%%%%%%%%%%%%%%%%%%%%%%%%%%%%%%%%%%%%%%%%%%%%%%%%%%%%%%%%%%%%%%%%%%%%
76 % Replacement Stiffnesses
77 %%%%%%%%%%%%%%%%%%%%%%%%%%%%%%%%%%%%%%%%%%%%%%%%%%%%%%%%%%%%%%%%%%%%%%%%%%%
78 % Interpolated height along the beam
79 h = interp1([0, L], [h1, h2], (node_z(1:end-1) + le / 2));
80
81 % Cross-sectional properties
82 A = b .* h; % Enclosed area [m^2]
83
84 % Stiffness calculations
85 EI = b .* (h.^2) / (2 * af(1, 1)) + 2 * b / df(1, 1) + 2 * (h.^3) / (12 * aw(1, 1)
86 ); % Bending stiffness [Nm^2]
87
88 GJ = 2 * b^2 .* h.^2 ./ (af(3, 3) * b + aw(3, 3) .* h); % Torsional stiffness [Nm
89 ^2]
90
91 %%%%%%%%%%%%%%%%%%%%%%%%%%%%%%%%%%%%%%%%%%%%%%%%%%%%%%%%%%%%%%%%%%%%%%%%%%%
92 % Applied Loads
93 %%%%%%%%%%%%%%%%%%%%%%%%%%%%%%%%%%%%%%%%%%%%%%%%%%%%%%%%%%%%%%%%%%%%%%%%%%%
94 % Load distribution calculation
95 [q, qt] = load_distribution(node_z, alpha); % Distributed load [N/m], distributed
96 torque [Nm/m]
97
98
99

```

Matlab Code for FEM Analysis of the Main Spar

```

94 %%%%%%%%%%%%%%%%%%%%%%%%%%%%%%%%%%%%%%%%%%%%%%%%%%%%%%%%%%%%%%%%%%%%%%%%%
95 % Assemble Stiffness Matrix and Load Vector
96 %%%%%%%%%%%%%%%%%%%%%%%%%%%%%%%%%%%%%%%%%%%%%%%%%%%%%%%%%%%%%%%%%%%%%%%%%
97 [K, Q] = assemble(le, EI, GJ, q, qt, ndof, nelem); % Assemble global stiffness
    and load vector
98
99 %%%%%%%%%%%%%%%%%%%%%%%%%%%%%%%%%%%%%%%%%%%%%%%%%%%%%%%%%%%%%%%%%%%%%%%%%
100 % Apply Boundary Conditions
101 %%%%%%%%%%%%%%%%%%%%%%%%%%%%%%%%%%%%%%%%%%%%%%%%%%%%%%%%%%%%%%%%%%%%%%%%%
102 % Apply boundary conditions by removing locked degrees of freedom
103 free_dofs = [2, 4:3*(nelem/6), 3*(nelem/6) + 2, 3*(nelem/6) + 4:ndof];
104 Ks = K(free_dofs, free_dofs);
105 Qs = Q(free_dofs);
106
107 %%%%%%%%%%%%%%%%%%%%%%%%%%%%%%%%%%%%%%%%%%%%%%%%%%%%%%%%%%%%%%%%%%%%%%%%%
108 % Solve Beam Bending and Torsion Equations
109 %%%%%%%%%%%%%%%%%%%%%%%%%%%%%%%%%%%%%%%%%%%%%%%%%%%%%%%%%%%%%%%%%%%%%%%%%
110 [defl, teta, fi, w] = bending(Ks, Qs, K, Q, nelem, nnode, node_z);
111
112 %%%%%%%%%%%%%%%%%%%%%%%%%%%%%%%%%%%%%%%%%%%%%%%%%%%%%%%%%%%%%%%%%%%%%%%%%
113 % Post-Processing
114 %%%%%%%%%%%%%%%%%%%%%%%%%%%%%%%%%%%%%%%%%%%%%%%%%%%%%%%%%%%%%%%%%%%%%%%%%
115 % Calculate internal forces and stresses along the beam
116 [Mx, Tx, Mz, sigmaf0, sigmaf45, sigmaw0, sigmaw45, etaf, etaw] = stress(w, EI, GJ,
    Qf, Qw0, Qw45, af, df, aw, dw, le, h, tw, tf, A, ndof, node_z);
117
118 %%%%%%%%%%%%%%%%%%%%%%%%%%%%%%%%%%%%%%%%%%%%%%%%%%%%%%%%%%%%%%%%%%%%%%%%%
119 % Local Buckling Analysis
120 %%%%%%%%%%%%%%%%%%%%%%%%%%%%%%%%%%%%%%%%%%%%%%%%%%%%%%%%%%%%%%%%%%%%%%%%%
121 % Calculate critical local buckling load
122 Nxcr = (2 * (pi^2) / b^2) * (sqrt(Df(1, 1) * Df(2, 2)) + Df(1, 1) + 2 * Df(3, 3));
    % Critical local buckling load
123 Nx = 4 * 0.000152 * max(abs(sigmaf0(1, :))) + 2 * 0.000218 * max(abs(sigmaf45(1,
    :))); % Applied load comparison
124
125 %%%%%%%%%%%%%%%%%%%%%%%%%%%%%%%%%%%%%%%%%%%%%%%%%%%%%%%%%%%%%%%%%%%%%%%%%
126 % Display Results
127 %%%%%%%%%%%%%%%%%%%%%%%%%%%%%%%%%%%%%%%%%%%%%%%%%%%%%%%%%%%%%%%%%%%%%%%%%
128
129 % Display Tip Deflection and Tip Twist
130 tip_deflection = w(end-2) * 1e3; % Tip deflection in [mm]
131 disp(['Tip deflection: w = ', num2str(tip_deflection), ' [mm]']);
132
133 tip_twist = w(end) * 180 / pi; % Tip twist in degrees
134 disp(['Tip twist: teta = ', num2str(tip_twist), ' [ ]']);
135
136 % Maximum Normal and Shear Stresses in Flanges (UD Ply)
137 max_sigmaf0_normal = max(abs(sigmaf0(1, :))) * 1e-6; % Convert to [MPa]
138 disp(['Maximum normal stress in flanges (UD ply): sigma_max = ', num2str(
    max_sigmaf0_normal), ' [MPa]']);
139
140 max_sigmaf0_shear = max(abs(sigmaf0(3, :))) * 1e-6; % Convert to [MPa]
141 disp(['Maximum shear stress in flanges (UD ply): tau_max = ', num2str(
    max_sigmaf0_shear), ' [MPa]']);
142
143 % Maximum Normal and Shear Stresses in Flanges (PW Ply)
144 max_sigmaf45_normal = max(abs(sigmaf45(1, :))) * 1e-6; % Convert to [MPa]
145 disp(['Maximum normal stress in flanges (PW ply): sigma_max = ', num2str(
    max_sigmaf45_normal), ' [MPa]']);
146
147 max_sigmaf45_shear = max(abs(sigmaf45(3, :))) * 1e-6; % Convert to [MPa]

```

Matlab Code for FEM Analysis of the Main Spar

```

148 disp(['Maximum shear stress in flanges (PW ply): tau_max = ', num2str(
      max_sigmaf45_shear), ' [MPa]']);
149
150 % Maximum Normal and Shear Stresses in Webs (PW_0 Ply)
151 max_sigmax0_normal = max(abs(sigmax0(1, :))) * 1e-6; % Convert to [MPa]
152 disp(['Maximum normal stress in webs (PW_0 ply): sigma_max = ', num2str(
      max_sigmax0_normal), ' [MPa]']);
153
154 max_sigmax0_shear = max(abs(sigmax0(3, :))) * 1e-6; % Convert to [MPa]
155 disp(['Maximum shear stress in webs (PW_0 ply): tau_max = ', num2str(
      max_sigmax0_shear), ' [MPa]']);
156
157 % Maximum Normal and Shear Stresses in Webs (PW_45 Ply)
158 max_sigmax45_normal = max(abs(sigmax45(1, :))) * 1e-6; % Convert to [MPa]
159 disp(['Maximum normal stress in webs (PW_45 ply): sigma_max = ', num2str(
      max_sigmax45_normal), ' [MPa]']);
160
161 max_sigmax45_shear = max(abs(sigmax45(3, :))) * 1e-6; % Convert to [MPa]
162 disp(['Maximum shear stress in webs (PW_45 ply): tau_max = ', num2str(
      max_sigmax45_shear), ' [MPa]']);
163
164 disp(['Critical Local Buckling Load (Nxcr) = ', num2str(Nxcr), ' [N/m]']);
165 disp(['Calculated Applied Load (Nx) = ', num2str(Nx), ' [N/m]']);

```

load_distribution.m

```

1 function [q, qt] = load_distribution(node_z, alpha)
2 %%%%%%%%%%%%%%%%%%%%%%%%%%%%%%%%%%%%%%%%%%%%%%%%%%%%%%%%%%%%%%%%%%%%%%%%%
3 % Function: load_distribution
4 % Purpose: Calculate distributed lift and torsional moment load on a beam
5 %
6 % Inputs:
7 %   - node_z : Array of nodal z-coordinates along the beam [m]
8 %   - alpha  : Angle between y_0 and z-axis [rad]
9 %
10 % Outputs:
11 %   - q      : Distributed lift force along the beam [N/m]
12 %   - qt     : Distributed torque along the beam [Nm/m]
13 %%%%%%%%%%%%%%%%%%%%%%%%%%%%%%%%%%%%%%%%%%%%%%%%%%%%%%%%%%%%%%%%%%%%%%%%%
14
15 %% Import Lift Distribution Data
16 load('lift_spar.mat'); % Load the lift distribution data
17 Lspar = Liftdistributionspar; % Extract data (columns represent span position,
      chord, cl, etc.)
18
19 % Parameters for Load Distribution Calculations
20 xsc_r = 0.7; % Shear center position at the root [m]
21 rho = 1.225; % Air density [kg/m^3]
22 g = 9.81; % Gravitational acceleration [m/s^2]
23 v = 27.6; % Airspeed [m/s]
24
25 %%%%%%%%%%%%%%%%%%%%%%%%%%%%%%%%%%%%%%%%%%%%%%%%%%%%%%%%%%%%%%%%%%%%%%%%%
26 % Lift Distribution Calculations
27 %%%%%%%%%%%%%%%%%%%%%%%%%%%%%%%%%%%%%%%%%%%%%%%%%%%%%%%%%%%%%%%%%%%%%%%%%
28
29 % Lift distribution for the entire UAV
30 dL = 0.5 * rho * Lspar(:, 2) .* Lspar(:, 3) * v^2; % Lift per unit length [N/m]
31 total_Lift = trapz(Lspar(:, 1), dL); % Total lift force [N]
32 disp(['Total Lift (entire UAV): L = ', num2str(total_Lift), ' [N]']);
33
34 % Lift distribution for the wing only

```

Matlab Code for FEM Analysis of the Main Spar

```

35 Lspar = Lspar(140:end, :); % Filter lift data for the
    wing portion
36 dL = 0.5 * rho * Lspar(:, 2) .* Lspar(:, 3) * v^2; % Recalculate lift
    distribution for the filtered data
37
38 % Lift distribution for the spar
39 Lspar(:, 1) = (Lspar(:, 1) - Lspar(1, 1)) ./ cos(alpha); % Correct span position
    along the spar
40 Lspar(:, 3) = Lspar(:, 3) .* cos(alpha); % Adjust lift
    coefficient for inclination
41 dL = 0.5 * rho * Lspar(:, 2) .* Lspar(:, 3) * v^2; % Calculate lift
    distribution for the spar [N/m]
42
43 %%%%%%%%%%%%%%%%%%%%%%%%%%%%%%%%%%%%%%%%%%%%%%%%%%%%%%%%%%%%%%%%%%%%%%%%%%
44 % Moment Distribution Calculations (Spar)
45 %%%%%%%%%%%%%%%%%%%%%%%%%%%%%%%%%%%%%%%%%%%%%%%%%%%%%%%%%%%%%%%%%%%%%%%%%%
46
47 % Calculate center of pressure relative to shear center and resulting moment
    distribution
48 cop = (Lspar(:, 4) + Lspar(:, 5) - (xsc_r + Lspar(:, 1) * sin(alpha))); % Center
    of pressure
49 dM = dL .* cop; % Torsional moment distribution [Nm/m]
50
51 % Calculate total lift and moment applied to the beam
52 Lift_spar = trapz(Lspar(:, 1), dL); % Total lift applied to the beam [N]
53 disp(['Total Lift (spar): L = ', num2str(Lift_spar), ' [N]']);
54
55 Moment_spar = trapz(Lspar(:, 1), dM); % Total torsional moment applied to the
    beam [Nm]
56 disp(['Total Torsional Moment (spar): M_z = ', num2str(Moment_spar), ' [Nm]']);
57
58 %%%%%%%%%%%%%%%%%%%%%%%%%%%%%%%%%%%%%%%%%%%%%%%%%%%%%%%%%%%%%%%%%%%%%%%%%%
59 % Interpolate Load Distribution to Nodes
60 %%%%%%%%%%%%%%%%%%%%%%%%%%%%%%%%%%%%%%%%%%%%%%%%%%%%%%%%%%%%%%%%%%%%%%%%%%
61
62 % Interpolate lift (q) and moment (qt) distributions to the beam nodes
63 q = interp1(Lspar(:, 1), dL, (node_z(2:end) + node_z(1:end-1)) / 2); %
    Distributed lift [N/m]
64 qt = interp1(Lspar(:, 1), dM, (node_z(2:end) + node_z(1:end-1)) / 2); %
    Distributed torque [Nm/m]
65
66 end

```

assemble.m

```

1 function [K, Q] = assemble(le, EI, GJ, q, qt, ndof, nelem)
2 %%%%%%%%%%%%%%%%%%%%%%%%%%%%%%%%%%%%%%%%%%%%%%%%%%%%%%%%%%%%%%%%%%%%%%%%%%
3 % Function: assemble
4 % Purpose: Assemble the system stiffness matrix and load vector for a
5 %           beam undergoing bending and torsion.
6 %
7 % Inputs:
8 %   - le : Element length [m]
9 %   - EI : Element bending stiffness [Nm^2]
10 %   - GJ : Element torsional stiffness [Nm^2]
11 %   - q : Element transverse pressure load [N/m]
12 %   - qt : Element torsional pressure load [Nm/m]
13 %   - ndof : Number of degrees of freedom
14 %   - nelem : Number of elements
15 %
16 % Outputs:

```

Matlab Code for FEM Analysis of the Main Spar

```

17 % - K      : System stiffness matrix
18 % - Q      : System load vector
19 %
20 % Notes:
21 % The function assembles the global stiffness matrix `K` and the global
22 % load vector `Q` by looping through each element and adding its contributions.
23 %%%%%%%%%%%%%%%%%%%%%%%%%%%%%%%%%%%%%%%%%%%%%%%%%%%%%%%%%%%%%%%%%%%%%%%%%
24
25 % Initialize the global stiffness matrix (K) and load vector (Q)
26 K = zeros(ndof);      % Global stiffness matrix [ndof x ndof]
27 Q = zeros(ndof, 1);   % Global load vector [ndof x 1]
28
29 %%%%%%%%%%%%%%%%%%%%%%%%%%%%%%%%%%%%%%%%%%%%%%%%%%%%%%%%%%%%%%%%%%%%%%%%%
30 % Calculate Element Stiffness Matrices and Load Vectors
31 %%%%%%%%%%%%%%%%%%%%%%%%%%%%%%%%%%%%%%%%%%%%%%%%%%%%%%%%%%%%%%%%%%%%%%%%%
32 Kel = zeros(6, 6, nelelem); % Initialize storage for element stiffness matrices [6
   % x 6 x nelelem]
33 Qel = zeros(6, nelelem);    % Initialize storage for element load vectors [6 x
   % nelelem]
34
35 for i = 1:nelelem
36     % Element stiffness matrix (Kel) for element `i`
37     Kel(:, :, i) = [12*EI(i)/le^3, -6*EI(i)/le^2, 0, -12*EI(i)/le^3, -6*EI(i)/le
   ^2, 0;
38                     -6*EI(i)/le^2, 4*EI(i)/le, 0, 6*EI(i)/le^2, 2*EI(i)/le, 0;
39                     0, 0, GJ(i)/le, 0, 0, -GJ(i)/le;
40                     -12*EI(i)/le^3, 6*EI(i)/le^2, 0, 12*EI(i)/le^3, 6*EI(i)/le^2,
   0;
41                     -6*EI(i)/le^2, 2*EI(i)/le, 0, 6*EI(i)/le^2, 4*EI(i)/le, 0;
42                     0, 0, -GJ(i)/le, 0, 0, GJ(i)/le];
43
44     % Element load vector (Qel) for element `i`
45     Qel(:, i) = [q(i)*le/2, -q(i)*le^2/12, qt(i)*le/2, q(i)*le/2, q(i)*le^2/12, qt
   (i)*le/2]';
46 end
47
48 %%%%%%%%%%%%%%%%%%%%%%%%%%%%%%%%%%%%%%%%%%%%%%%%%%%%%%%%%%%%%%%%%%%%%%%%%
49 % Assemble Global Stiffness Matrix and Load Vector
50 %%%%%%%%%%%%%%%%%%%%%%%%%%%%%%%%%%%%%%%%%%%%%%%%%%%%%%%%%%%%%%%%%%%%%%%%%
51 % Initial assignment for the first element to the global matrices
52 K(1:6, 1:6) = Kel(:, :, 1);
53 Q(1:6) = Qel(:, 1);
54
55 % Loop through elements to assemble global stiffness matrix and load vector
56 for i = 2:nelelem
57     % Determine global indices for the current element
58     start_idx = 3 * (i - 1) + 1; % Start index for the current element
59     end_idx = start_idx + 5;     % End index for the current element
60
61     % Add current element stiffness matrix to the global stiffness matrix
62     K(start_idx:end_idx, start_idx:end_idx) = ...
63     K(start_idx:end_idx, start_idx:end_idx) + Kel(:, :, i); % Element
   contribution to global stiffness
64
65     % Add current element load vector to the global load vector
66     Q(start_idx:end_idx) = Q(start_idx:end_idx) + Qel(:, i); % Element
   contribution to global load vector
67 end
68
69 end

```

bending.m

```

1 function [defl , teta , fi , w] = bending(Ks, Qs, K, Q, nele, nnode, node_z)
2 %%%%%%%%%%%%%%%%%%%%%%%%%%%%%%%%%%%%%%%%%%%%%%%%%%%%%%%%%%%%%%%%%%%%%%%%%
3 % Function: bending
4 % Purpose: Calculate the deformed shape of a beam under bending and torsion,
5 %           including deflections, rotations, and twists. Additionally,
6 %           compute maximum values and present reaction forces.
7 %
8 % Inputs:
9 %   - Ks      : Structural stiffness matrix for the reduced system
10 %   - Qs      : Structural load vector for the reduced system
11 %   - K       : System stiffness matrix
12 %   - Q       : System load vector
13 %   - nele    : Number of elements
14 %   - nnode   : Number of nodes
15 %   - node_z  : Array of nodal z-coordinates
16 %
17 % Outputs:
18 %   - defl    : Deflection vector of size nnode
19 %   - teta    : Rotation vector of size nnode
20 %   - fi     : Twist vector of size nnode
21 %   - umax   : Maximum deflection
22 %   - tmax   : Maximum rotation
23 %   - fimax  : Maximum twist
24 %   - w      : Complete result vector containing all displacements
25 %%%%%%%%%%%%%%%%%%%%%%%%%%%%%%%%%%%%%%%%%%%%%%%%%%%%%%%%%%%%%%%%%%%%%%%%%
26
27 % Solve the reduced system of equations for displacements
28 wf = Ks \ Qs;
29
30 %%%%%%%%%%%%%%%%%%%%%%%%%%%%%%%%%%%%%%%%%%%%%%%%%%%%%%%%%%%%%%%%%%%%%%%%%
31 % Calculate Reaction Forces
32 %%%%%%%%%%%%%%%%%%%%%%%%%%%%%%%%%%%%%%%%%%%%%%%%%%%%%%%%%%%%%%%%%%%%%%%%%
33 % Assemble the complete displacement vector, including zero displacements
34 % for the degrees of freedom locked by boundary conditions.
35 w = zeros(3 * nnode, 1);
36 w([2, 4:3*(nele/6), 3*(nele/6) + 2, 3*(nele/6) + 4:end]) = wf;
37
38 % Compute the reaction forces using the complete system stiffness matrix (K)
39 F_r = K * w - Q;
40
41 % Extract the reaction forces and moments at specific points
42 F_1 = F_r([1, 3, 3 * (nele / 6) + 1, 3 * (nele / 6) + 3]);
43
44 % Display reaction forces at the base (z = 0) and at z = L/6
45 disp(['The reaction force and moment at z = 0 are: T_1 = ', num2str(F_1(1)), ' [N
46     ], C_1 = ', num2str(F_1(2)), ' [N*m]']);
47
48 disp(['The reaction force and moment at z = L/6 are: T_2 = ', num2str(F_1(3)), ' [
49     N], C_2 = ', num2str(F_1(4)), ' [N*m]']);
50
51 %%%%%%%%%%%%%%%%%%%%%%%%%%%%%%%%%%%%%%%%%%%%%%%%%%%%%%%%%%%%%%%%%%%%%%%%%
52 % Extract Deflections, Rotations, and Twists
53 %%%%%%%%%%%%%%%%%%%%%%%%%%%%%%%%%%%%%%%%%%%%%%%%%%%%%%%%%%%%%%%%%%%%%%%%%
54 % Split the result vector into components representing deflection,
55 % rotation, and twist for each cross-section along the beam.
56 defl = w(1:3:end-2); % Cross-section deflection vector
57 teta = w(2:3:end-1); % Cross-section rotation vector
58 fi = w(3:3:end); % Cross-section twist vector

```

stress.m

Matlab Code for FEM Analysis of the Main Spar

```

1 function [Mx, Ty, Mz, sigmaf0, sigmaf45, sigmaw0, sigmaw45, etaf, etaw] = stress(w
2     , EI, GJ, Qf, Qw0, Qw45, af, df, aw, dw, le, h, tw, tf, A, ndof, node_z)
3 %~~~~~%
4 % Function: stress
5 % Purpose: Calculate internal forces (bending moment, shear force, and
6 % torsional moment) and stresses in flanges and webs.
7 % Outputs:
8 % - Mx, Ty, Mz : Bending moment, shear force, and torsional moment along the
9 % beam
10 % - sigmaf0, sigmaf45 : Stress in the flanges for UD and PW ply
11 % - sigmaw0, sigmaw45 : Stress in the webs for PW_0 and PW45 ply
12 % - etaf, etaw : Strains in flanges and webs
13 %~~~~~%
14 % Initialize Vectors for Internal Forces and Stresses
15 num_elems = ndof / 3 - 1;
16 Mx = zeros(num_elems, 1); % Bending moment along the beam
17 Ty = zeros(num_elems, 1); % Shear force along the beam
18 Mz = zeros(num_elems, 1); % Torsional moment along the beam
19
20 sigmaf0 = []; sigmaf45 = [];
21 sigmaw0 = []; sigmaw45 = [];
22 etaf = []; etaw = [];
23 %~~~~~%
24 % Loop Through Each Element to Calculate Forces and Stresses
25 %~~~~~%
26 for i = 1:num_elems
27     % Calculate Shear Force (Ty) and Curvature (K)
28     Ty(i) = -EI(i) * ((12 / le^3) * w(3 * (i-1) + 1) - (6 / le^2) * w(3 * (i-1) +
29     2) ...
30     - (12 / le^3) * w(3 * i + 1) - (6 / le^2) * w(3 * i + 2));
31     K = -Ty(i) / EI(i);
32     % Calculate Bending Moment (Mx)
33     Mx(i) = -EI(i) * ((-6 / le^2) * w(3 * (i-1) + 1) + (4 / le) * w(3 * (i-1) + 2)
34     ...
35     + (6 / le^2) * w(3 * i + 1) + (2 / le) * w(3 * i + 2));
36     % Calculate Torsional Moment (Mz)
37     Mz(i) = GJ(i) * (w(3 * (i-1) + 6) - w(3 * (i-1) + 3)) / le;
38
39     % Calculate Shear Flow
40     qt = Mz(i) / (2 * A(i)); % Torsional shear flow
41     qbw = -K * (h(i) * (A(i) / h(i)) / (4 * af(1, 1)) + h(i)^2 / (8 * aw(1, 1)));
42     % Bending shear flow in webs
43     qbf = -K * h(i) * (A(i) / h(i)) / (4 * af(1, 1)); % Bending shear flow in
44     flanges
45     % Calculate In-plane Force Vectors in Flanges (Nf) and Webs (Nw)
46     Nf = [Mx(i) * (h(i) / 2) / (EI(i) * af(1, 1));
47     qbf + sign(qbf) * abs(qt);
48     Mx(i) / (EI(i) * df(1, 1))];
49     Nw = [Mx(i) * (h(i) / 2) / (EI(i) * aw(1, 1));
50     qbw + sign(qbw) * abs(qt);
51     0];
52
53     % Calculate Strains in Flanges (etaf_total) and Webs (etaw_total)

```

Matlab Code for FEM Analysis of the Main Spar

```
54   etaf_total = [af(1, 1) 0 0; af(1, 2) 0 0; 0 af(3, 3) 0; 0 0 df(1, 1); 0 0 df
55   (1, 2); 0 0 0] * Nf;
56   etaw_total = [aw(1, 1) 0 0; aw(1, 2) 0 0; 0 aw(3, 3) 0; 0 0 dw(1, 1); 0 0 dw
57   (1, 2); 0 0 0] * Nw;
58   % Extract Strains for Flanges and Webs
59   etaf(:, i) = etaf_total(1:3) + tf / 2 * etaf_total(4:end); % Flange strains
60   etaw(:, i) = etaw_total(1:3); % Web strains
61   % Calculate Stresses in Flanges and Webs
62   sigmaf0(:, i) = Qf * etaf(:, i); % Flange stress vector for UD ply
63   sigmaf45(:, i) = Qw45 * etaf(:, i); % Flange stress vector for PW ply
64   sigmaw45(:, i) = Qw45 * etaw(:, i); % Web stress vector for PW45 ply
65   sigmaw0(:, i) = Qw0 * etaw(:, i); % Web stress vector for PW0 ply
66 end
```

Appendix C

Matlab Code for FEM Analysis of Cylindrical Beams

cylindrical.m

```
1 %%%%%%%%%%%%%%%%%%%%%%%%%%%%%%%%%%%%%%%%%%%%%%%%%%%%%%%%%%%%%%%%%%%%%%%%%%
2 % Main Program: Cylindrical Beam
3 % Beam FE-code for bending about 1-axis and St. Venant torsion
4 %
5 % Use SI units only
6 %%%%%%%%%%%%%%%%%%%%%%%%%%%%%%%%%%%%%%%%%%%%%%%%%%%%%%%%%%%%%%%%%%%%%%%%%%
7
8 % Clean workspace and command window
9 clear all;
10 close all;
11 clc;
12
13 %%%%%%%%%%%%%%%%%%%%%%%%%%%%%%%%%%%%%%%%%%%%%%%%%%%%%%%%%%%%%%%%%%%%%%%%%%
14 % Definitions and Input Data
15 %%%%%%%%%%%%%%%%%%%%%%%%%%%%%%%%%%%%%%%%%%%%%%%%%%%%%%%%%%%%%%%%%%%%%%%%%%
16 % Geometry Definition
17 L = 1;           % Tube length [m]
18 r = 0.015;      % Tube radius [m]
19 t = 0.001044;   % Tube thickness [m]
20
21 %%%%%%%%%%%%%%%%%%%%%%%%%%%%%%%%%%%%%%%%%%%%%%%%%%%%%%%%%%%%%%%%%%%%%%%%%%
22 % Material Properties (ABD Matrices)
23 %%%%%%%%%%%%%%%%%%%%%%%%%%%%%%%%%%%%%%%%%%%%%%%%%%%%%%%%%%%%%%%%%%%%%%%%%%
24 % Stiffness matrices for different plies
25 Qud = 1e9 * [129 3.19 0;
26             3.19 9.11 0;
27             0 0 5.22]; % UD ply stiffness matrix
28
29 Qpw = 1e9 * [35.3 26.7 0;
30             26.7 35.3 0;
31             0 0 2.59]; % PW45 ply stiffness matrix
32
```

Matlab Code for FEM Analysis of Cylindrical Beams

```

33 % Compliance matrices for the cylindrical spar
34 A = [0.938884e8 0.135747e8 0.291013e-8;
35       0.135747e8 0.209241e8 -0.291013e-8;
36       0.291013e-8 -0.291013e-8 0.144538e8];
37
38 D = [9.29460      1.04088      0.209766e-15;
39       1.04088      1.68651      -0.209766e-15;
40       0.209766e-15 -0.209766e-15 1.14401];
41
42 % Calculate inverse compliance matrices
43 a = inv(A);
44 d = inv(D);
45
46 %%%%%%%%%%%%%%%%%%%%%%%%%%%%%%%%%%%%%%%%%%%%%%%%%%%%%%%%%%%%%%%%%%%%%%%%%
47 % Element Input Data
48 %%%%%%%%%%%%%%%%%%%%%%%%%%%%%%%%%%%%%%%%%%%%%%%%%%%%%%%%%%%%%%%%%%%%%%%%%
49 nelem = 30;           % Number of elements (MUST BE MULTIPLE OF 10)
50 le = L / nelem;      % Length of each element [m]
51 ndof = 3 * (nelem + 1); % Number of degrees of freedom
52 nnode = nelem + 1;   % Number of nodes
53
54 % Node coordinates along the beam (centered on 0)
55 node_z = linspace(-L / 2, L / 2, nnode)'; % Node coordinates [m]
56
57 %%%%%%%%%%%%%%%%%%%%%%%%%%%%%%%%%%%%%%%%%%%%%%%%%%%%%%%%%%%%%%%%%%%%%%%%%
58 % Geometrical Stiffness Properties
59 %%%%%%%%%%%%%%%%%%%%%%%%%%%%%%%%%%%%%%%%%%%%%%%%%%%%%%%%%%%%%%%%%%%%%%%%%
60 % Cross-sectional properties
61 A = pi * (r^2 - (r - t)^2); % Cross-section area [m^2]
62
63 % Stiffness calculations
64 EI = pi * (r^3 / a(1, 1) + r / d(1, 1)); % Bending stiffness [Nm^2]
65 GJ = 2 * pi^2 * r^3 / a(3, 3);         % Torsional stiffness [Nm^2]
66
67 %%%%%%%%%%%%%%%%%%%%%%%%%%%%%%%%%%%%%%%%%%%%%%%%%%%%%%%%%%%%%%%%%%%%%%%%%
68 % Applied Loads
69 %%%%%%%%%%%%%%%%%%%%%%%%%%%%%%%%%%%%%%%%%%%%%%%%%%%%%%%%%%%%%%%%%%%%%%%%%
70 S1 = 546.8; % Concentrated load outer structures [N]
71 S2 = -382.2; % Concentrated load inner structures [N]
72
73 %%%%%%%%%%%%%%%%%%%%%%%%%%%%%%%%%%%%%%%%%%%%%%%%%%%%%%%%%%%%%%%%%%%%%%%%%
74 % Assemble Stiffness Matrix and Load Vector
75 %%%%%%%%%%%%%%%%%%%%%%%%%%%%%%%%%%%%%%%%%%%%%%%%%%%%%%%%%%%%%%%%%%%%%%%%%
76 [K, Q] = assemble_c(le, EI, GJ, S1, S2, ndof, nelem); % Assemble global stiffness
    and load vector
77
78 %%%%%%%%%%%%%%%%%%%%%%%%%%%%%%%%%%%%%%%%%%%%%%%%%%%%%%%%%%%%%%%%%%%%%%%%%
79 % Apply Boundary Conditions
80 %%%%%%%%%%%%%%%%%%%%%%%%%%%%%%%%%%%%%%%%%%%%%%%%%%%%%%%%%%%%%%%%%%%%%%%%%
81 % Remove locked degrees of freedom to apply boundary conditions
82 free_dofs = [1:3*4*nelem/10, 3*4*nelem/10+2, 3*4*nelem/10+4:3*6*nelem/10, 3*6*
    nelem/10+2, 3*6*nelem/10+4:ndof];
83 Ks = K(free_dofs, free_dofs);
84 Qs = Q(free_dofs);
85
86 %%%%%%%%%%%%%%%%%%%%%%%%%%%%%%%%%%%%%%%%%%%%%%%%%%%%%%%%%%%%%%%%%%%%%%%%%
87 % Solve Beam Bending and Torsion Equations
88 %%%%%%%%%%%%%%%%%%%%%%%%%%%%%%%%%%%%%%%%%%%%%%%%%%%%%%%%%%%%%%%%%%%%%%%%%
89 [defl, teta, fi, w] = bending_c(Ks, Qs, K, Q, nnode, nelem, node_z);
90
91 %%%%%%%%%%%%%%%%%%%%%%%%%%%%%%%%%%%%%%%%%%%%%%%%%%%%%%%%%%%%%%%%%%%%%%%%%

```

Matlab Code for FEM Analysis of Cylindrical Beams

```

92 % Post-Processing
93 %%%%%%%%%%%%%%%%%%%%%%%%%%%%%%%%%%%%%%%%%%%%%%%%%%%%%%%%%%%%%%%%%%%%%%%%%
94 % Calculate internal forces and stresses along the cylindrical spar
95 [Mx, Tx, sigma_90, sigma_0] = stress_c(w, Qud, Qpw, a, d, EI, GJ, le, r, t, ndof);
96
97 %%%%%%%%%%%%%%%%%%%%%%%%%%%%%%%%%%%%%%%%%%%%%%%%%%%%%%%%%%%%%%%%%%%%%%%%%
98 % Display Results
99 %%%%%%%%%%%%%%%%%%%%%%%%%%%%%%%%%%%%%%%%%%%%%%%%%%%%%%%%%%%%%%%%%%%%%%%%%
100 % Maximum stresses in UD and PW layers
101 disp(['Maximum normal stress (UD layer): sigma_max = ', num2str(max(abs(sigma_90
102     (1, :, 1))) * 1e-6), ' [MPa] ']);
102 disp(['Maximum shear stress (UD layer): tau_max = ', num2str(max(abs(sigma_0(3, :,
103     1))) * 1e-6), ' [MPa] ']);
103 disp(['Maximum normal stress (PW layer): sigma_max = ', num2str(max(abs(sigma_90
104     (1, :, 2))) * 1e-6), ' [MPa] ']);
104 disp(['Maximum shear stress (PW layer): tau_max = ', num2str(max(abs(sigma_0(3, :,
105     2))) * 1e-6), ' [MPa] ']);

```

assemble_c.m

```

1  function [K, Q] = assemble_c(le, EI, GJ, S1, S2, ndof, nelem)
2  %%%%%%%%%%%%%%%%%%%%%%%%%%%%%%%%%%%%%%%%%%%%%%%%%%%%%%%%%%%%%%%%%%%%%%%%%
3  % Function: assemble_c
4  % Purpose: Assemble the system stiffness matrix and load vector for
5  %           a cylindrical beam under bending.
6  %
7  % Outputs:
8  % - K      : Global stiffness matrix
9  % - Q      : Global load vector
10 %%%%%%%%%%%%%%%%%%%%%%%%%%%%%%%%%%%%%%%%%%%%%%%%%%%%%%%%%%%%%%%%%%%%%%%%%
11
12 % Initialize the global stiffness matrix (K) and load vector (Q)
13 K = zeros(ndof);           % Global stiffness matrix [ndof x ndof]
14 Q = zeros(ndof, 1);       % Global load vector [ndof x 1]
15
16 %%%%%%%%%%%%%%%%%%%%%%%%%%%%%%%%%%%%%%%%%%%%%%%%%%%%%%%%%%%%%%%%%%%%%%%%%
17 % Define Element Stiffness Matrix
18 %%%%%%%%%%%%%%%%%%%%%%%%%%%%%%%%%%%%%%%%%%%%%%%%%%%%%%%%%%%%%%%%%%%%%%%%%
19 % Element stiffness matrix for bending and torsion [6x6]
20 Ke = [12*EI/le^3, -6*EI/le^2, 0, -12*EI/le^3, -6*EI/le^2, 0;
21      -6*EI/le^2, 4*EI/le, 0, 6*EI/le^2, 2*EI/le, 0;
22      0, 0, GJ/le, 0, 0, -GJ/le;
23      -12*EI/le^3, 6*EI/le^2, 0, 12*EI/le^3, 6*EI/le^2, 0;
24      -6*EI/le^2, 2*EI/le, 0, 6*EI/le^2, 4*EI/le, 0;
25      0, 0, -GJ/le, 0, 0, GJ/le];
26
27 %%%%%%%%%%%%%%%%%%%%%%%%%%%%%%%%%%%%%%%%%%%%%%%%%%%%%%%%%%%%%%%%%%%%%%%%%
28 % Assemble the Global Stiffness Matrix
29 %%%%%%%%%%%%%%%%%%%%%%%%%%%%%%%%%%%%%%%%%%%%%%%%%%%%%%%%%%%%%%%%%%%%%%%%%
30 % Add the element contributions to the global stiffness matrix
31 for i = 1:nelem
32     start_idx = (i - 1) * 3 + 1; % Start index for the current element in global
33     end_idx = start_idx + 5;     % End index for the current element in global
34     % Assemble the current element stiffness into the global stiffness matrix
35     K(start_idx:end_idx, start_idx:end_idx) = K(start_idx:end_idx, start_idx:
36     end_idx) + Ke;
37 end
38

```

Matlab Code for FEM Analysis of Cylindrical Beams

```

39 %%%%%%%%%%%%%%%%%%%%%%%%%%%%%%%%%%%%%%%%%%%%%%%%%%%%%%%%%%%%%%%%%%%%%%%%%
40 % Add Concentrated Loads
41 %%%%%%%%%%%%%%%%%%%%%%%%%%%%%%%%%%%%%%%%%%%%%%%%%%%%%%%%%%%%%%%%%%%%%%%%%
42 % Add concentrated loads to the global load vector
43 % The loads are applied at specific nodes
44 Q(1) = Q(1) + S1;           % Load at z=-L/2
45 Q(end - 2) = Q(end - 2) + S1; % Load at z=L/2
46
47 Q(3 * 3 * nelem / 10 + 1) = Q(3 * 3 * nelem / 10 + 1) + S2; % Load at z=-L/5
48 Q(3 * 7 * nelem / 10 + 1) = Q(3 * 7 * nelem / 10 + 1) + S2; % Load at z=L/5
49
50 end

```

bending_c.m

```

1 function [defl, teta, fi, w] = bending_c(Ks, Qs, K, Q, nnode, nelem, node_z)
2 %%%%%%%%%%%%%%%%%%%%%%%%%%%%%%%%%%%%%%%%%%%%%%%%%%%%%%%%%%%%%%%%%%%%%%%%%
3 % Function: bending_c
4 % Purpose: Calculate the deformed shape of a cylindrical beam under
5 %           bending and torsion, including deflections, rotations, and twists.
6 %
7 % Outputs:
8 %   - defl      : Deflection vector of size nnode
9 %   - teta      : Rotation vector of size nnode
10 %   - fi       : Twist vector of size nnode
11 %   - w        : Complete result vector containing all displacements
12 %%%%%%%%%%%%%%%%%%%%%%%%%%%%%%%%%%%%%%%%%%%%%%%%%%%%%%%%%%%%%%%%%%%%%%%%%
13
14 %%%%%%%%%%%%%%%%%%%%%%%%%%%%%%%%%%%%%%%%%%%%%%%%%%%%%%%%%%%%%%%%%%%%%%%%%
15 % Solve System of Equations for Displacements
16 %%%%%%%%%%%%%%%%%%%%%%%%%%%%%%%%%%%%%%%%%%%%%%%%%%%%%%%%%%%%%%%%%%%%%%%%%
17 % Solve reduced system of equations
18 wf = Ks \ Qs;
19
20 %%%%%%%%%%%%%%%%%%%%%%%%%%%%%%%%%%%%%%%%%%%%%%%%%%%%%%%%%%%%%%%%%%%%%%%%%
21 % Present Reaction Forces
22 %%%%%%%%%%%%%%%%%%%%%%%%%%%%%%%%%%%%%%%%%%%%%%%%%%%%%%%%%%%%%%%%%%%%%%%%%
23 % Create the full displacement vector including zero values for the locked DOFs
24 w = zeros(3 * nnode, 1);
25 free_dofs = [1:3*4*nelem/10, 3*4*nelem/10+2, 3*4*nelem/10+4:3*6*nelem/10, 3*6*
26             nelem/10+2, 3*6*nelem/10+4:3*nnode];
27 w(free_dofs) = wf;
28
29 % Calculate reaction forces
30 F_r = K * w - Q;
31
32 % Extract the reaction forces at key points
33 reaction_indices = [3*4*nelem/10+1, 3*4*nelem/10+3, 3*6*nelem/10+1, 3*6*nelem
34                    /10+3];
35 F_r = F_r(reaction_indices);
36
37 % Display the reaction forces
38 disp(['The reaction forces are: T_1 = ', num2str(F_r(2)), ' [N], T_2 = ', num2str(
39       F_r(3)), ' [N]']);
40
41 %%%%%%%%%%%%%%%%%%%%%%%%%%%%%%%%%%%%%%%%%%%%%%%%%%%%%%%%%%%%%%%%%%%%%%%%%
42 % Split Displacement into Deflection, Rotation, and Twist
43 %%%%%%%%%%%%%%%%%%%%%%%%%%%%%%%%%%%%%%%%%%%%%%%%%%%%%%%%%%%%%%%%%%%%%%%%%
44 % Deflection, rotation, and twist for each node
45 defl = w(1:3:end-2); % Deflection vector
46 teta = w(2:3:end-1); % Rotation vector

```

Matlab Code for FEM Analysis of Cylindrical Beams

```
44 fi = w(3:3:end); % Twist vector
```

stress_c.m

```
1 function [Mx, Ty, sigma_90, sigma_0] = stress_c(w, Qud, Qpw, a, d, EI, GJ, le, r,
2     t, ndof)
3 %%%%%%%%%%%%%%%%%%%%%%%%%%%%%%%%%%%%%%%%%%%%%%%%%%%%%%%%%%%%%%%%%%%%%%%%%%%
4 % Function: stress_c
5 % Purpose: Calculate internal forces (bending moment, torsional moment,
6 %         and shear force) and stresses in the cylindrical spar.
7 %
8 % Outputs:
9 % - Mx      : Bending moment along the beam
10 % - Tx     : Shear force along the beam
11 % - sigma_90: Stress for theta = 90 (for UD and PW plies)
12 % - sigma_0 : Stress for theta = 0 (for UD and PW plies)
13 %%%%%%%%%%%%%%%%%%%%%%%%%%%%%%%%%%%%%%%%%%%%%%%%%%%%%%%%%%%%%%%%%%%%%%%%%%%
14 %%%%%%%%%%%%%%%%%%%%%%%%%%%%%%%%%%%%%%%%%%%%%%%%%%%%%%%%%%%%%%%%%%%%%%%%%%%
15 % Initialization of Internal Forces and Stresses
16 %%%%%%%%%%%%%%%%%%%%%%%%%%%%%%%%%%%%%%%%%%%%%%%%%%%%%%%%%%%%%%%%%%%%%%%%%%%
17 num_elems = ndof / 3 - 1; % Number of elements along the beam
18 Mx = zeros(num_elems, 1); % Bending moment vector [Nm]
19 Tx = zeros(num_elems, 1); % Shear force vector [N]
20
21 sigma_90 = zeros(3, num_elems, 2); % Stresses for theta = 90 in UD and PW plies
22 sigma_0 = zeros(3, num_elems, 2); % Stresses for theta = 0 in UD and PW plies
23
24 %%%%%%%%%%%%%%%%%%%%%%%%%%%%%%%%%%%%%%%%%%%%%%%%%%%%%%%%%%%%%%%%%%%%%%%%%%%
25 % Loop Through Each Element to Calculate Forces and Stresses
26 %%%%%%%%%%%%%%%%%%%%%%%%%%%%%%%%%%%%%%%%%%%%%%%%%%%%%%%%%%%%%%%%%%%%%%%%%%%
27 for i = 1:num_elems
28     % Calculate Bending Moment (Mx)
29     Mx(i) = -EI * ((-6 / le^2) * w(3 * (i - 1) + 1) + (4 / le) * w(3 * (i - 1) +
30         2) ...
31         + (6 / le^2) * w(3 * i + 1) + (2 / le) * w(3 * i + 2));
32     % Calculate Shear Force (Tx)
33     Ty(i) = -EI * ((12 / le^3) * w(3 * (i - 1) + 1) - (6 / le^2) * w(3 * (i - 1) +
34         2) ...
35         - (12 / le^3) * w(3 * i + 1) - (6 / le^2) * w(3 * i + 2));
36
37     % Calculate Shear Flow
38     q=Ty(i)/EI*r^2/a(1,1); % Shear flow
39
40     % In-plane Force Vectors
41     % N_90 represents in-plane forces for theta = 90
42     % N_0 represents in-plane forces for theta = 0
43     N_90 = [Mx(i) * r / (EI * a(1, 1)); 0; Mx(i) / (EI * d(1, 1))];
44     N_0 = [0; q; 0];
45
46     % Calculate Strains for theta = 90 (eta_total_90)
47     eta_total_90 = [a(1, 1) 0 0;
48         a(1, 2) 0 0;
49         0 a(3, 3) 0;
50         0 0 d(1, 1);
51         0 0 d(1, 2);
52         0 0 0] * N_90;
53
54     % Calculate Strains for theta = 0 (eta_total_0)
```

```
55 eta_total_0 = [a(1, 1) 0 0;  
56               a(1, 2) 0 0;  
57               0 a(3, 3) 0;  
58               0 0 d(1, 1);  
59               0 0 d(1, 2);  
60               0 0 0] * N_0;  
61  
62 eta_90 = eta_total_90(1:3) + (t / 2) * eta_total_90(4:end);  
63  
64 eta_0 = eta_total_0(1:3) + (t / 2) * eta_total_0(4:end);  
65  
66 % Calculate Stresses in the Layers  
67 sigma_90(:, i, 1) = Qud * eta_90; % UD ply stress at theta=90  
68 sigma_90(:, i, 2) = Qpw * eta_90; % PW ply stress at theta=90  
69 sigma_0(:, i, 1) = Qud * eta_0; % UD ply stress at theta=0  
70 sigma_0(:, i, 2) = Qpw * eta_0; % PW ply stress at theta=0  
71  
72  
73 end
```

Bibliography

- [1] Michael Iwanizki et al. «Conceptual design studies of unconventional configurations». In: *3AF Aerospace Europe Conference 2020*. BORDEAUX, France, Feb. 2020. URL: <https://hal.science/hal-02907205> (cit. on p. 1).
- [2] Siwat Suewatanakul, Alessandro Porcarelli, Adam Olsson, Henrik Grimler, Ariel Chiche, Raffaello Mariani, and Göran Lindbergh. «Conceptual Design of a Hybrid Hydrogen Fuel Cell/Battery Blended-Wing-Body Unmanned Aerial Vehicle—An Overview». In: *Aerospace* 9.5 (2022). ISSN: 2226-4310. DOI: 10.3390/aerospace9050275. URL: <https://www.mdpi.com/2226-4310/9/5/275> (cit. on pp. 1, 77).
- [3] *Certification Specifications for Very Light Aeroplanes (CS-VLA)*. Tech. rep. Amendment 1. European Union Aviation Safety Agency (EASA), 2021. URL: <https://www.easa.europa.eu/en/document-library/certification-specifications/group/cs-vla-very-light-aeroplanes> (visited on 11/22/2024) (cit. on p. 24).
- [4] Shams Anwar and Xianguo Li. «A review of high-quality epoxy resins for corrosion-resistant applications». In: *Journal of Coatings Technology and Research* 21.2 (Mar. 2024), pp. 461–480 (cit. on pp. 32, 67).
- [5] Michael Thor, Markus G. R. Sause, and Roland M. Hinterhölzl. «Mechanisms of Origin and Classification of Out-of-Plane Fiber Waviness in Composite Materials—A Review». In: *Journal of Composites Science* 4.3 (2020). ISSN: 2504-477X. DOI: 10.3390/jcs4030130. URL: <https://www.mdpi.com/2504-477X/4/3/130> (cit. on p. 32).
- [6] Sebastiaan Wijskamp. «Shape distortions in composites forming». In: (Jan. 2005) (cit. on p. 32).
- [7] Toray Advanced Composites. *2510 Prepreg System*. 2024. URL: <https://www.toraycma.com/wp-content/uploads/2510-Prepreg-System.pdf> (cit. on p. 33).

-
- [8] Gong-Dong Wang, Jun Wang, Sayed K.M. Hossain, and Hao Chen. In: *Science and Engineering of Composite Materials* 22.3 (2015), pp. 315–323. DOI: doi: 10.1515/secm-2013-0251. URL: <https://doi.org/10.1515/secm-2013-0251> (cit. on p. 33).
- [9] László P. Kollár and George S. Springer. *Mechanics of Composite Structures*. Cambridge University Press, 2003 (cit. on pp. 36, 41, 45).
- [10] Diab Group. *Divinycell H*. Accessed: 2024-11-23. 2024. URL: <https://diab-media.azureedge.net/eyajkrhd/diab-divinycell-h-november-2024-rev24-si.pdf> (cit. on p. 37).
- [11] Dan Zenkert. «An Introduction to Sandwich Structures». In: 1995. URL: <https://api.semanticscholar.org/CorpusID:231338919> (cit. on p. 37).
- [12] MatWeb. *7075-T6 Aluminum Data Sheet*. Accessed: 2024-10-01. 2024. URL: <https://asm.matweb.com/search/specificmaterial.asp?bassnum=ma7075t6> (cit. on p. 38).
- [13] S. Minera, M. Patni, E. Carrera, M. Petrolo, P.M. Weaver, and A. Pirrera. «Three-dimensional stress analysis for beam-like structures using Serendipity Lagrange shape functions». In: *International Journal of Solids and Structures* 141-142 (2018), pp. 279–296. ISSN: 0020-7683. DOI: <https://doi.org/10.1016/j.ijsolstr.2018.02.030>. URL: <https://www.sciencedirect.com/science/article/pii/S0020768318300866> (cit. on p. 42).
- [14] T.H.G. Megson. «Chapter 17 - Matrix Methods of Analysis». In: *Structural and Stress Analysis (Fourth Edition)*. Ed. by T.H.G. Megson. Fourth Edition. Butterworth-Heinemann, 2019, pp. 607–652. ISBN: 978-0-08-102586-4. DOI: <https://doi.org/10.1016/B978-0-08-102586-4.00017-2>. URL: <https://www.sciencedirect.com/science/article/pii/B9780081025864000172> (cit. on p. 42).
- [15] Pizhong Qiao and Luyang Shan. «Explicit local buckling analysis and design of fiber-reinforced plastic composite structural shapes». In: *Composite Structures* 70.4 (2005), pp. 468–483. ISSN: 0263-8223. DOI: <https://doi.org/10.1016/j.compstruct.2004.09.005>. URL: <https://www.sciencedirect.com/science/article/pii/S0263822304003125> (cit. on p. 60).
- [16] J. Chakrabarty. «CHAPTER TWO - FOUNDATIONS OF PLASTICITY». In: *Theory of Plasticity (Third Edition)*. Ed. by J. Chakrabarty. Third Edition. Oxford: Butterworth-Heinemann, 2006, pp. 56–126. ISBN: 978-0-7506-6638-1. DOI: <https://doi.org/10.1016/B978-0-7506-6638-1.50008-X>. URL: <https://www.sciencedirect.com/science/article/pii/B978075066638150008X> (cit. on p. 64).

- [17] ANSYS. *Inertia Relief Analysis*. Ansys Documentation. 2023. URL: https://ansyshelp.ansys.com/public/account/secured?returnurl=/Views/Secured/corp/v242/en/ans_thry/thy_tool2.html (visited on 11/10/2024) (cit. on p. 78).
- [18] David Eller Dan Borglund. *Aeroelasticity of Slender Wing Structures in Low-Speed Airflow*. Division of Flight Dynamics, Royal Institute of Technology, 2016 (cit. on p. 82).